Mathematical Modelling of the Merging of Turbulent Plumes with Applications to Heat Pump Efflux

Alistair Delboyer

Supervisors: Matthew Scase[1], Matthew Hubbard[1], Matthew Johnson[2]

1: University of Nottingham School of Mathematical Sciences

2: University of Nottingham School of Geography

October 2021

Abstract

In this thesis, the impact of open loop heat pumps on rivers is investigated. These heat pumps inject water of a different temperature into the environment as part of their heating (or cooling) process. In doing so, thermal plumes are created. The behaviour of these thermal plumes is studied using thermal imagery from the Matapédia river and a relationship between the temperature difference between the plume and the downstream distance from the source of the plume is determined.

The cumulative impact of heat pumps on the ambient environment is investigated. This is carried out by considering the distance from the outflow of these heat pumps, or equivalently the sources of the thermal plumes, to the position where the thermal plumes can be considered to behave as one larger plume. This distance, the merging height (or merging distance), is studied as a function of source separation between the plumes, number of plumes and cross-flow velocity of the ambient environment. The mathematical models devised to study this show that the merging height increases linearly with source separation in both stillwater and a cross-flow, increases with the number of plumes, and decays exponentially with increasing cross-flow velocities. These findings are confirmed by experimental data. In conclusion, this work has determined relationships to explain the cumulative impact of heat pumps on the ambient environment and makes suggestions for further areas of investigation.

Acknowledgements

This PhD would not have been possible alone, and there are many people to thank for their contribution, both academically and otherwise. First and foremost, I'd like to thank my supervisors in no particular order - Matthew, Matthew and Matthew for their unending support in all aspects of the PhD, from their academic guidance to helping fend off the ridiculous difficulties incurred from trying to finish this thesis during a global pandemic. This project could not have been completed without your support. I'd like to thank Matt Johnson for his support through my placement and with the experimental work in the flume. I'd also like to thank Matt Scase and Matthew Hubbard for their support since my undergraduate degree, giving me the tools and passion to pursue a PhD in the first place. Lastly, I'd like to thank Matt Scase for convincing me to take a fluids module in my undergraduate degree when I'd written off the topic at the end of my second year...I bet you regret that now you've been stuck with me for four years.

Alongside my supervisors, there are many PGRs and post-docs to thank. I'd like to thank the following people for their support, hospitality and friendship through the last four years, or however long we were lucky enough to overlap for - Ben, Bethan, Tom, Heather, Anne, Rik, Mayo, Bobby, Charlotte, Róisín, the freshwater friends (formerly fluvial friends), all students on the MASS programme, and lastly, those who made the return from the pandemic not only possible, but enjoyable. I would also like to thank my family for their support in all things that it took to get this far, their unlimited patience, love and support.

I would also be remiss for not mentioning those outside of the PhD, namely those that I climb with, or those that I fence with. These groups provided an incredible outlet for the stress of the PhD, and helped me return to a state where the problems weren't quite as impossible. In particular, I'd like to acknowledge two fencers - the late John Holt, and my coach Jenna Griffiths. The former for tricking me into not quitting the sport at the start of the PhD, and the latter for constant support on and off piste, putting up with me at training, as well as her pastoral support towards the return to normality.

Finally, I'd like to thank the Leverhulme Trust for funding this thesis as part of the Modelling and Analytics for a Sustainable Society Doctoral Training Programme.

Contents

Chapter 1

Introduction

1.1 Outline of Thesis

This thesis will investigate the environmental impacts of so-called heat pumps - a renewable and sustainable source of energy. The key impact of these heat pumps is their tendency to change the temperature of the body of water in which they are based by discharging water of different temperature to ambient. In this thesis, we consider the impacts of heat pumps on rivers. This impact may be particularly problematic when the re-injected water is warmer than the ambient river as this can lead to thermal barriers and harm riverine life, as discussed in §1.2.2. Furthermore, there are several sites of so-called "district heating/cooling" where a number of heat pumps (in some cases over 100) are used in a single system. Therefore, it is critical to understand the cumulative impact that heat pumps can have on river temperature.

Individual plumes are studied in the Matapédia river, Quebec, using thermal imagery in §2. We track the temperature of these plumes relative to the Matapédia river and determine how this temperature returns to that of the ambient river as a function of distance downstream from the plume source. The cumulative impact of heat pumps is investigated using mathematical modelling in §3 and §4 for a stationary environment. We study the downstream distance from the point of injection where the multiple plumes will behave as a single plume and the behaviour of this plume thereafter. This modelling is then validated experimentally in §4.6. The investigation of plumes is then extended to plumes in a cross-flow in §5 subject to a behaviour known in the existing literature as the "blockage effect" (discussed in detail in §5.2). Finally, these mathematical models are validated against flume experiments in §6.

1.2 Environmental Background

1.2.1 Introduction to Heat Pumps

In recent years, investment in renewable sources of energy has increased dramatically in an attempt to move away from fossil fuels and prevent catastrophic climate change [1]. The utility of renewable energy is limited by location; for example solar energy production is greater and more cost effective near the equator than at higher latitudes, where day length is more variable. Most common forms of renewable energy (e.g. solar, hydroelectric, wind, geothermal) are well studied and used in many countries across the globe. Solar power is used globally, whereas other sources are more geographically limited such as geothermal energy which is used in countries that are located on tectonic plates or thermal hotspots, particularly Iceland and Kenya.

In May 2019, the Committee on Climate Change (CCC) published a report, [2], to outline the steps taken by the UK to reach "net zero" by 2050. This refers to the UK having no net carbon emissions by 2050. Reaching net zero by 2050 is an ambitious goal and a key technology cited in the report by the

CCC is the use of heat pumps.

Heat pumps are a form of renewable energy which are currently used at small scales to provide heating to houses, blocks of flats and factories. These heat pumps utilise heat in the environment to provide energy. They are particularly useful as they use low-grade (waste or secondary) heat [3, 4], which can be generated from the thermal by-product of other processes. This energy would otherwise be wasted. While heat pumps have a higher start-up cost than non-renewable heating systems, they are more cost-effective in the longer term [5] because they move energy from one place to another without having to "create" it. There is also significantly less energy wasted than non-renewable systems.

A schematic of the inside of a heat pump is given in Figure 1.1. Heat pumps use a high pressure, gaseous refrigerant that is circulated by a compressor. Once through the compressor, the hot, high pressure gas warms the surrounding environment. It is then cooled by the condenser until it condenses into a high pressure, cool liquid. This liquid passes through an expansion valve to an evaporator, where the liquid evaporates, thereby absorbing heat. The refrigerant then enters the compressor and the cycle is repeated [6].

Heat pumps may be used for either warming or cooling, and in some cases both. For example, in London, 62% of heat pumps are used for cooling, 36% for both and only 2% for only heating [7].

The heat pumps themselves are split into three main categories: air source, water source and ground source, where the source refers to the medium from which heat is extracted (Figure 1.1). In the UK, due to the relatively constant river temperature, water source heat pumps are more efficient than air source heat pumps [9]. Also the heat transfer rate of water is greater,

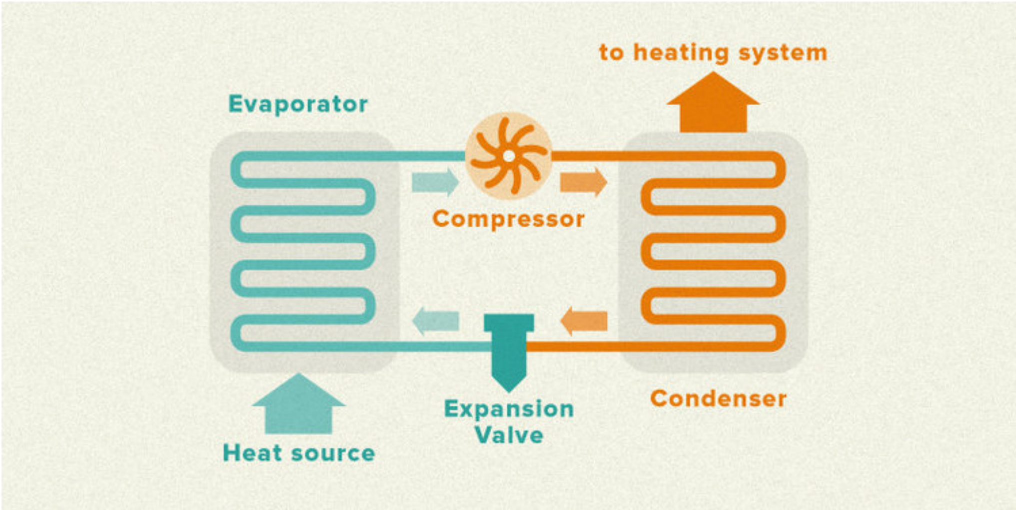

FIGURE 1.1: Schematic of the inside of a heat pump. Taken from [8].

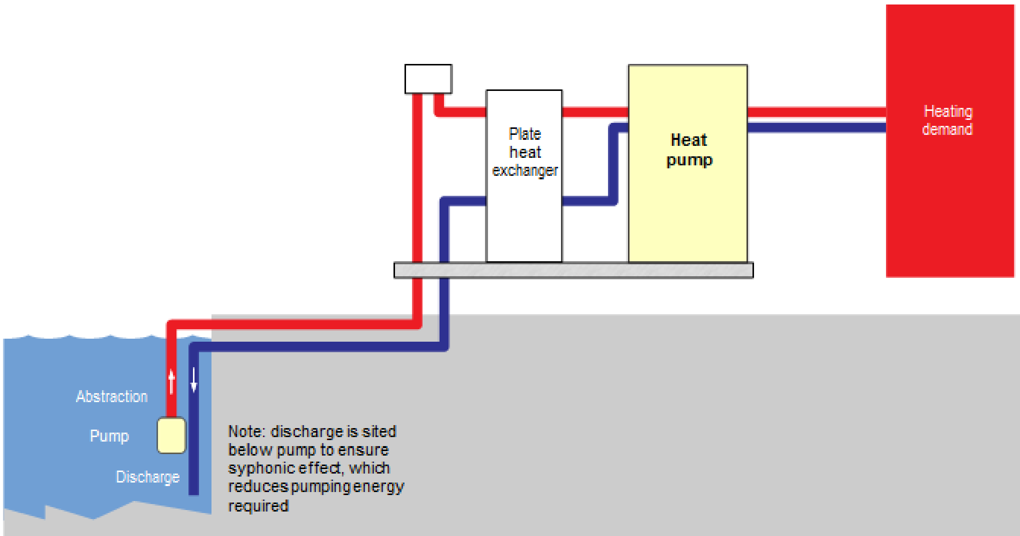

FIGURE 1.2: Schematic of a typical open loop system, taken from [5].

on average, than air or groundwater sources. Typical values for the heat transfer rate are $10 - 100\,\mathrm{W\,m^{-2}\,K^{-1}}$ in air [10], $50 - 10,000\,\mathrm{W\,m^{-2}\,K^{-1}}$ in water [10], and $30 - 60\,\mathrm{W\,m^{-2}\,K^{-1}}$ in the ground [11, 12, 13]. As such, water source heat pumps are a very feasible and potentially highly efficient heating source for the UK.

Water source heat pumps may be split further into open (an example of which is given in Figure 1.2) and closed loop. An open loop uses separate pipes for extraction and reinjection of water, while a closed loop has one continuous pipe, as shown in Figure 1.3. Closed loop heat pumps are advantageous due to their low maintenance and have fewer regulations in place [5]. On the other hand, open loop heat pumps are more flexible as the abstraction rate can be varied to meet needs, but in the UK they require abstraction and discharge permits (unless the volumes being abstracted are less than $20\,\mathrm{m^3}$ per day). Furthermore, the positioning of an open loop heat pump is critical as poor positioning can lead to recirculation, reducing the efficiency of the heat pump due to so-called "parasitic energy consumption" or "thermal breakthrough" [5].

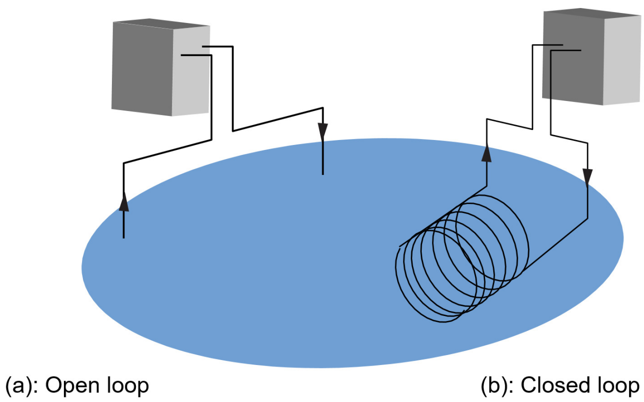

Figure 1.3: Diagram showing the difference between open and closed loop heat pumps from [5].

There are several measures of efficiency for heat pumps. These are the coefficient of performance (CoP) [14], seasonal coefficient of performance (SCoP) and the seasonal performance factor (SPF) [15]. The CoP and

SCoP are calculated quantities while the SPF is a measured quantity. The coefficient of performance is defined as

$$\mathrm{CoP} = \frac{\text{useful heat output}}{\text{electrical power input}},$$

and is an instantaneous value. The seasonal coefficient of performance is a long term measure, typically given over a season, month or year. It is given by

$$\mathrm{SCoP} = \frac{\text{total useful heat output}}{\text{total electrical power input}}.$$

The SPF is measured using

$$\mathrm{SPF} = \frac{\text{annual heat out}}{\text{annual electrical power in}}.$$

Each of these quantities assumes that the heat pump is used for heating. If it is used for cooling, analogous quantities are the energy efficiency ratio (EER) and the seasonal energy efficiency ratio (SEER).

The maximum theoretical CoP is given by

$$\mathrm{CoP}_{\mathrm{max}} = \frac{T_{\mathrm{out}}}{T_{\mathrm{out}} - T_{\mathrm{in}}}$$

for temperature, T, and the so-called Lorenz efficiency is defined as

$$\eta_{\mathrm{Lorenz}} = \frac{\mathrm{CoP}}{\mathrm{CoP}_{\mathrm{max}}} \leq 1$$

and is a measure of how well a heat pump is performing compared to an optimal heat pump. From these definitions, given in [16], we see that the power input to a heat pump must be reduced to increase its efficiency. This can be done in several ways, from adapting the rate of abstraction to ensuring that the source temperature is close to that of the object being heated. The temperature difference is likely to be more important than the abstraction rate since, relative to the volume of water in the river, the amount being abstracted will be small. Therefore, more attention should be paid to the positioning of heat pumps and their thermal impacts on the ambient river temperature.

1.2.2 Impact of Thermal Pollution on Riverine Life

Currently, the legislation regarding the discharge of water from heat pumps varies depending on location. For example, the Environment Agency (EA) of England advises that the temperature of water discharged back into the river must be within ±3 °C of the ambient river temperature. These acceptable temperature ranges are chosen to limit damage to riverine life, particularly those that are temperature sensitive. The ultimate aim of management is to keep river temperatures below 21 °C, which is critical for salmon, trout and many other fish species [17, 18, 19]. Most aquatic organisms have a specific temperature range that they can comfortably inhabit [20, 21, 22]. Therefore, a small increase in temperature could lead to significant changes in the faunal community, including the loss of key species [23]. However, due to rising temperatures across the globe, rivers are regularly exceeding this threshold, including in the UK, without the use of heat pumps [24, 20, 25, 26]. Therefore the impact of additional heating by heat pumps could be significant in adding to an already significant stressor on aquatic life in rivers. To this end, more work must be done to ascertain the impact of heat pumps on ambient river temperatures.

There are several scales of heat pumps used in the UK, which vary from single, small heat pumps, such as that installed at Hyde Mill, to so-called "district heating" systems such as that used in Kingston Heights [27, 28]. Hyde Mill uses a single, open loop, heat pump to provide additional heating and cooling to a farm in Gloucester, while Kingston Heights uses a network of 39 heat pumps to provide heating to 137 flats and a 142 room hotel

[28]. Hyde Mill discharges water at a low rate, as such, it is unlikely to have a significant impact on the temperature of the river. Kingston Heights abstracts up to 150 litres of water per second (compared to a mean river flow rate of $65.3\,\mathrm{m^3\,s^{-1}}$) and discharges water back to the river at no more than a $3\,^{\circ}\mathrm{C}$ temperature difference from ambient.

Despite these examples, there are no large scale trials for heat pumps, nor even any serious plans to decarbonise heating at all at the time of writing, [2]. Heat pumps themselves are relatively rare in the UK, with only 1% and 5% of renewable energy coming from heat pumps in 2017 and 2018 respectively [29, 30], despite the financial incentive provided by the renewable heat incentive (RHI). This incentive is in place to help the UK reach its goal of 12% of heating coming from renewable sources by 2020. However, this scheme was not successful in this goal, and has been extended to 2022. RHI payments are made quarterly over a span of seven years, and the amount varies depending on several factors, including tariffs and technology at the time of installation [31].

Presently, little is known about the impact of multiple heat pumps in the same area, despite examples such as Kingston Heights. Heat pumps being placed close together is also more likely as their numbers increase, particularly in urban areas. Therefore this thesis aims to model and analyse the behaviour of open loop water source heat pumps in rivers. These models and analyses aim to determine how the discharged fluid from the system will behave, how it will affect the ambient river and whether there is a way that the system may be configured to limit any further environmental effects. To do this, models of buoyancy-driven plumes must be developed.

1.3 Mathematical Background

1.3.1 Buoyancy-Driven Plumes

A buoyancy-driven plume is formed when a localised area of fluid experiences consistent buoyancy. This causes the fluid to rise, creating the typical, conical-shaped feature that we would expect to find exiting smoke stack chimneys or erupting volcanoes. These plumes exist on a wide range of scales, from very small such as above a burning candle, to very large such as the aforementioned volcanic ash cloud. These plumes will typically be highly turbulent, with a Reynolds' number greater than 10^4 [32]. This turbulence makes modelling a time dependent plume difficult, and computationally expensive. Despite this Morton, Taylor and Turner derived a model for time averaged plumes in their iconic paper [33] (henceforth MTT).

The modelling of MTT simplifies the coupled, non-linear Navier-Stokes' equations into three coupled ordinary differential equations (ODEs). To do this, three modelling assumptions are made. The first is to assume that the flow is Boussinesq, which is that the density differences between the plume and the environment may be ignored, except in any buoyancy terms. They also assume that the "rate of entrainment at the edge of the plume is proportional to a characteristic velocity at the same height". This will later become the famous entrainment assumption, first hypothesised by Zeldovich [34]. Finally, they assume that the "mean vertical velocity and mean buoyancy force in a horizontal section are of similar form at all heights" [33]. These assumptions give the significantly simplified system of equations

(1.1) - (1.3)

$$\frac{\mathrm{d}Q}{\mathrm{d}z} = 2\alpha M^{1/2} \tag{1.1}$$
$$\frac{\mathrm{d}M}{\mathrm{d}z} = \frac{FQ}{M} \tag{1.2}$$
$$\frac{\mathrm{d}F}{\mathrm{d}z} = -\mathrm{N}^2 Q \tag{1.3}$$

subject to $M(z=0)=0$, $Q(z=0)=0$, $F(z=0)=F_0$, where N^2 is the Brunt Väisälä frequency, and Q, M and F are the specific mass, momentum and buoyancy fluxes respectively. We note that this system of equations incorporates turbulence via α which is a result of the turbulent entrainment assumption. These equations are derived in §8.1 as well as in [35].

It is important to note that (1.1) - (1.3) have assumed that the quantities inside the plume follow a so-called top hat profile. This is a simplified model. In reality, these quantities are much more likely to follow a Gaussian profile. The difference is given schematically in Figure 1.4. To demonstrate the physical difference, we can consider the buoyancy of the system. In a top hat profile, we would have buoyancy inside the plume and none outside. However, in a Gaussian profile, the buoyancy would follow a Gaussian curve and therefore decay to zero as r tends to infinity. For the remainder of this chapter, we will work with the top hat profiles.

These quantities are expressed in terms of the plume radius, b, vertical velocity of fluid in the plume, w and the modified gravity of the plume, $g' = \dfrac{\rho_\infty - \rho}{\rho}$, where ρ denotes the density of fluid inside the plume and ρ_∞ denotes the density of fluid in the ambient environment. We define

$$Q = b^2 w \tag{1.4}$$
$$M = b^2 w^2 \tag{1.5}$$
$$F = b^2 w g'. \tag{1.6}$$

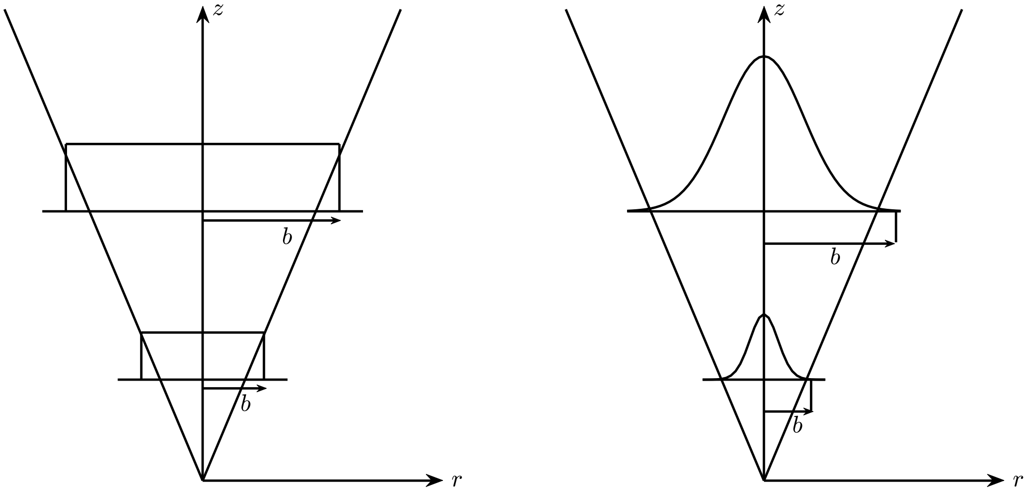

Figure 1.4: Schematic showing the difference between the profiles of quantities inside a plume when using top hat and Gaussian profiles.

We note that (1.1) uses the aforementioned entrainment assumption. It is assumed that the velocity of entrained fluid, u_e, is proportional to the mean centreline vertical velocity of fluid inside the plume at the same height. The constant of proportionality is α. Explicitly, the entrainment assumption is given by

$$u_e = \alpha w. \tag{1.7}$$

Typically, α is given the value 0.1 [36]. This was verified experimentally by Lee & Chu [37]. Despite this typical value of an entrainment coefficient, there is a surprising lack of consensus in the literature. This value is typically taken from the range $0.08 \leq \alpha \leq 0.13$, but the choice of entrainment coefficient depends on the author, with $\alpha = 0.09$ taken in [38, 39], $\alpha = 0.13$ in [33], $\alpha = 0.12$ in [40] and $0.05 \leq \alpha \leq 0.12$ in [41]. In this work, α is taken to be 0.1 unless experimental data shows otherwise.

The behaviour of a plume is dependent on the environment, specifically if the environment is stratified or unstratified. An environment is stratified if the density of the environment varies with height, specifically $\dfrac{\mathrm{d}\rho_\infty}{\mathrm{d}z} \neq 0$. This is represented in (1.1) - (1.3) by N^2. An environment is unstratified if $\mathrm{N}^2 = 0$. In this case, the plume may rise indefinitely because the fluid inside the plume will always be more buoyant than in the ambient environment. For $\mathrm{N}^2 = 0$, dimensional analysis may be used to find a power law solution. This solution is given, in terms of fluxes by

$$Q(z) = \frac{6\alpha}{5}\left(\frac{9\alpha}{10}\right)^{1/3} F_0^{1/3} z^{5/3}, \quad M(z) = \left(\frac{9\alpha}{10}\right)^{2/3} F_0^{2/3} z^{4/3}, \quad F(z) = F_0, \tag{1.8}$$

or in terms of the plume quantities

$$b = \frac{6\alpha}{5} z, \quad w = \frac{5}{6\alpha}\left(\frac{9\alpha}{10}\right)^{1/3} F_0^{1/3} z^{-1/3}, \quad g' = \frac{5}{6\alpha}\left(\frac{10}{9\alpha}\right)^{1/3} F_0^{2/3} z^{-5/3}. \tag{1.9}$$

Clearly (1.9) are not well-defined at $z = 0$ due to the singularity at this point, but are seen to be physically relevant sufficiently far from the source. Interestingly, the radius of a time averaged plume, b, grows linearly with height. Furthermore, the value of the entrainment coefficient, α, may be found experimentally using this time averaged radius.

For a stratified environment, where $\mathrm{N}^2 \neq 0$, there will be a finite height where the density of fluid inside the plume is equal to the density of the ambient environment. At this height, the plume will no longer be able to rise, and the fluid will then spread horizontally. The height at which a plume can no longer rise is commonly known as the rise height, or the height of neutral buoyancy, and was approximated experimentally by Briggs [42]. It was shown that this approximation is accurate for plumes of all scales, from table-top laboratory experiments to large oil fires as shown in Figure 1.5.

Thus far, only stillwater environments in which the environment is laminar have been discussed. An alternative case is turbulent plumes in turbulent but not flowing environments; for example, in a convecting environment. For a turbulent plume in a turbulent environment, the turbulence of the plume can entrain fluid from the environment and the turbulence of the environment

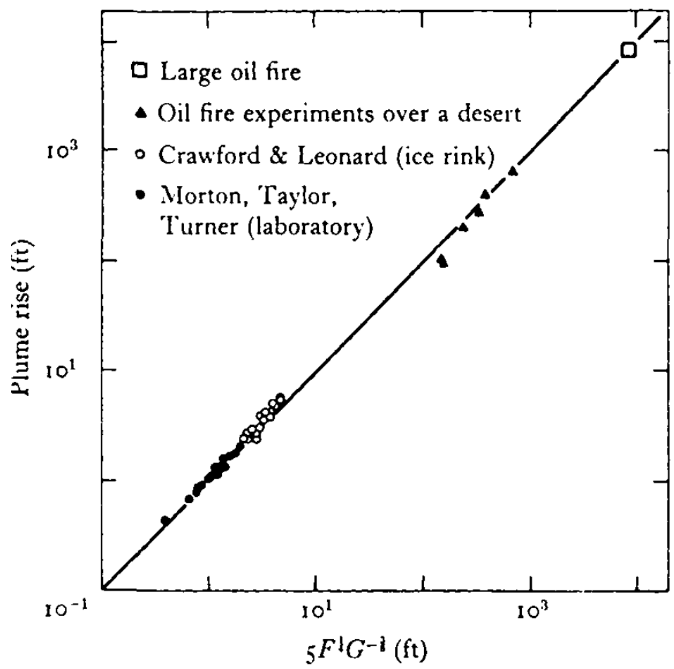

FIGURE 1.5: Measurements of plume rise in calm stratified surroundings taken from [42].

can entrain fluid from the plume. This entrainment of the plume by the environment is often referred to as extrainment. In this case the entrainment assumption is modified to capture the environment entraining the plume, and is given by

$$u_e = \alpha w - \beta V \tag{1.10}$$

where α and β are the entrainment and extrainment coefficients respectively, and V is some characteristic velocity. This characteristic velocity, given in [43, 44], is given by

$$V = 0.44 \left[\frac{(ga\Delta T)^4 \kappa^2 d^3}{\nu} \right]^{1/9} \tag{1.11}$$

where g denotes acceleration due to gravity, a is the coefficient of thermal expansion, d is the vertical length scale, κ is the thermal diffusivity and ν is the kinematic viscosity. The modified plume equations are studied in [45, 43]. To allow direct comparison, the MTT formulation given by (1.1) -

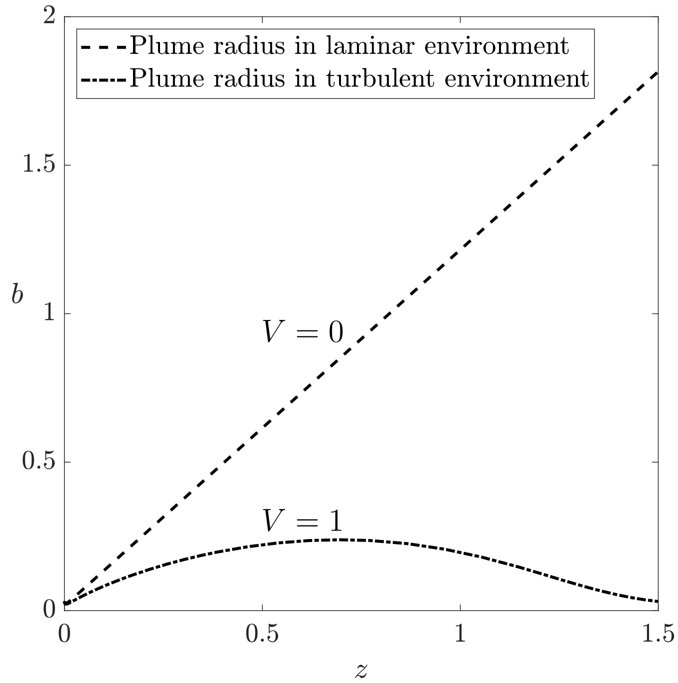

FIGURE 1.6: Figure comparing the different behaviour in the radii of plumes in laminar and turbulent environments taking $\alpha = \beta = 1$.

(1.3) are shown side-by-side with the modified equations given in [43]:

$$
\begin{aligned}
\frac{\mathrm{d}Q}{\mathrm{d}z} &= 2\alpha M^{1/2} & \qquad \frac{\mathrm{d}Q}{\mathrm{d}z} &= 2\alpha M^{1/2} - 2\beta V \frac{Q}{M^{1/2}} \\
\frac{\mathrm{d}M}{\mathrm{d}z} &= \frac{QF}{M} & \qquad \frac{\mathrm{d}M}{\mathrm{d}z} &= \frac{QF}{M} - 2\beta V M^{1/2} \\
\frac{\mathrm{d}F}{\mathrm{d}z} &= -\mathrm{N}^2 Q & \qquad \frac{\mathrm{d}F}{\mathrm{d}z} &= -\mathrm{N}^2 Q - 2\beta V \frac{QF}{M}.
\end{aligned}
$$

The right column of equations have no analytic solution, but a numerical solution is found in [43]. The radii of plumes in laminar and turbulent, stillwater, environments are compared in Figure 1.6, using $\alpha = \beta = V = 1$, and $\mathrm{N}^2 = 0$. The plume radius in the laminar environment, given by $b = \frac{6\alpha}{5} z$, can theoretically increase infinitely, whereas the plume radius in a turbulent environment increases to a point, then falls back to zero. This turning point, where the radius begins to decrease, is the point at which the environment is now entraining fluid from the plume faster than the plume can entrain.

It is also possible to extend the MTT model to plumes with buoyancy reversal [46], unsteady plumes [47], non-Boussinesq plumes where the density difference between the plume and the environment is not small [48], plumes in layered, stratified environments [49] and many other applications. However, to validate these models, experimental data is required.

Plumes created experimentally will often not satisfy the intrinsic assumptions of the MTT model. There will be a source of finite area, or momentum will be imparted to the plume at the source. In this case, the MTT model is still applicable, but must be corrected close to the source using a virtual origin correction.

1.3.1.1 Virtual Origin Correction

In the MTT models discussed so far, there has been an intrinsic assumption from the initial conditions of (1.1) - (1.3). It is implicitly assumed that the source of the plume is a point source of buoyancy, with no momentum or mass. This is not the case in practice. More realistically, one should take initial conditions

$$M(z=0) = M_0, \quad Q(z=0) = Q_0, \quad F(z=0) = F_0. \tag{1.12}$$

Taking these initial conditions, and considering an unstratified environment, we non-dimensionalise (1.1) - (1.3) using

$$Q = Q_0 q, \quad M = M_0 m, \quad F = F_0 \tag{1.13}$$

to give

$$m^{5/2} - 1 = \frac{5F_0 Q_0^2}{8\alpha M_0^{5/2}}(q^2 - 1) = \mathit{\Gamma}_0(q^2 - 1) \tag{1.14}$$

where $\mathit{\Gamma}_0 = \dfrac{5F_0 Q_0^2}{8\alpha M_0^{5/2}}$ is a source Froude number, and is a measure of the ratio of buoyancy, mass and momentum fluxes at the plume source. This parameter, sometimes referred to as a laziness parameter or a modified

Richardson number, was first derived by Morton [50] and later extended by Kaye & Hunt [40]. Plumes may be classified into forced, pure and lazy based on this parameter. If $0 < \mathit{\Gamma}_0 < 1$ a plume is said to be forced, as it has insufficient buoyancy when compared to the momentum. A plume is pure if $\mathit{\Gamma}_0 = 1$, i.e. the source quantities are balanced. Finally, $\mathit{\Gamma}_0 > 1$ gives a lazy plume, where the plume has insufficient momentum compared to its buoyancy. An analogous quantity, $\mathit{\Gamma}(z) = \dfrac{5F(z)Q(z)^2}{8\alpha M(z)^{5/2}}$, is the Froude number away from the source. It was shown, by Hunt & Kaye [51], that $\mathit{\Gamma}(z) \to 1$ for any height sufficiently far from the plume source. That is, the quantities in a plume will tend to balance after a sufficiently large distance. This suggests that, for any type or shape of source, the plume will tend to the traditional, conical form. This is indeed seen in nature [52]. The self regulation of these quantities by the plume is clearly visible in lazy plumes, where the plume will taper in, or neck, very quickly to compensate for the lack of momentum at the source. This provides enough "lift" to allow the plume to rise in the traditional, conical form. Importantly, the analysis above assumes top hat profiles are used. The above also holds for Gaussian profiles, except in that case $\mathit{\Gamma}_0 = \dfrac{5F_0Q_0^2}{4\alpha M_0^{5/2}}$.

The addition of these distributed source conditions (i.e. not a point of zero mass, momentum and non-zero buoyancy) means that (1.8) are no longer correct in the near field. We note that the governing equations (1.1) - (1.3) are still valid. In an unstratified environment, buoyancy flux is constant such that, $F = F_0$, so the idealised source may be seen as a translation, in the vertical direction, of the more realistic source. The position that a plume with initial conditions $Q(z = z_*) = 0$, $M(z = z_*) = 0$, $F(z = z_*) = F_0$ must originate from in order to behave as $Q(z = 0) = Q_0 > 0$, $M(z = 0) = M_0 > 0$, $F(z = z_*) = F_0$ is known as the "virtual origin", and this correction is often referred to as the "virtual origin correction" [50, 40, 53]. This is shown schematically in Figure 1.7. We see that the location of this virtual origin,

z_*, is given by $z_* \to 0.853\frac{5b_0}{6\alpha}\Gamma_0^{-1/5}$ as the plume laziness tends to infinity. A detailed discussion of this is given in §3.4.3 and [40].

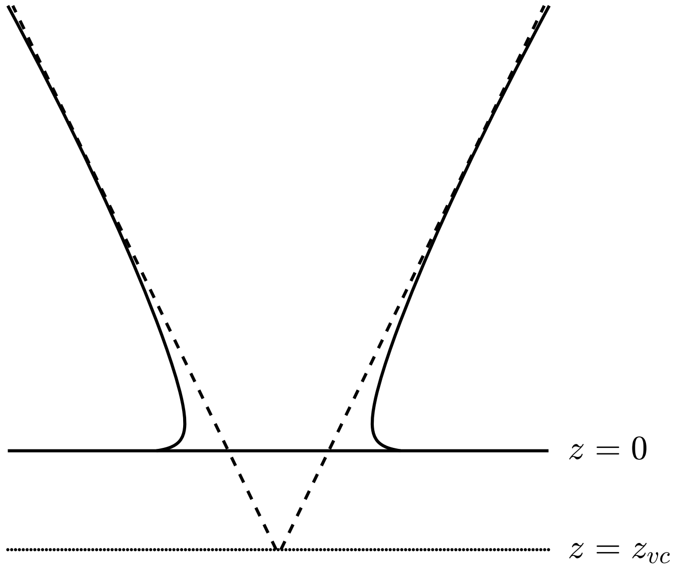

FIGURE 1.7: Schematic of the virtual origin correction for a lazy plume. The lazy plume has $\Gamma_0 = 39500$.

Chapter 2

Fieldwork

2.1 Motivation

The modelling in the subsequent chapters of this thesis will work towards determining the behaviour of plumes in both stationary and flowing environments. This is then validated using laboratory experiments. Laboratory experiments are a necessary simplification of natural complexity, enabling replication of key fluid behaviour for model validation not possible in the natural environment. While laboratory experiments give a physical representation of how fluid behaves, they are not necessarily the best representation of how fluid will behave in a natural environment due to the uncontrollable factors in a physical system in nature, specifically in rivers.

Uncontrollable factors, such as sediment size, roughness of the riverbed, temporary structures made by riverine life such as crayfish, and unique and dynamic channel geometry vary from river-to-river and can have unexpected consequences on the hydraulic environment, which will also vary in time in response to precipitation in the catchment. The mixing of water, and the development of plumes is common in rivers where tributaries hit the main branch of the river network and have different temperature and concentrations of sediment. Thermal plumes have also been identified downstream of power-plants, areas of groundwater upwelling, wastewater treatment plants and heat pumps. Since the hydraulic environment is highly variable both spatially and temporally over a range of scales from millimetres per second to hundreds of kilometres per millennia, and because of diurnal, seasonal and inter-annual changes in water temperature, the behaviour of thermal plumes is likely to be highly time and site specific. However, we hypothesise that generalisable patterns in plume behaviour are likely to exist based on laboratory studies and modelling work. Here, we will use aerial thermal imagery to investigate thermal plume behaviour at the confluence of tributaries in rivers, and determine whether generalisable patterns in plume behaviour exist. In particular, the aim of this investigation is to determine the distance downstream where a plume returns to the ambient river temperature.

2.2 Methodology

2.2.1 Data Collection

The data used in this chapter was collected at the Matapédia river, Canada at coordinates ($47.971°$ N, $-66.941°$ W). Airborne optical and thermal infrared (TIR) images were acquired during the summers of 2011 and 2012 by Dugdale *et al.* [54], who provided the raw imagery for this chapter. Imagery was obtained from a helicopter, using a custom-designed acquisition system consisting of a FLIR SC660 uncooled microbolometer TIR camera (640×480 pixels, NETD < 30mK, 7.5-13μm) and Canon EOS 550D digital SLR camera (5184×3456 pixels, standard RGB bands) as outlined in [54].

During the acquisition window, 1637 TIR images and a corresponding 1637 JPEG images were captured. From these images, we determined which images contained confluence plumes. This procedure extracted 66 images containing confluences with thermal plumes for further analysis. Using Forward Looking Infrared (FLIR), these 66 TIR files were converted to MAT (Microsoft Access Table) files containing the spatial and temperature information of the image. From these 66 MAT files, five were chosen for initial analysis. These small subset were selected based on river geometry and ratio of confluence width to river channel width. An example of a wide section of river with a wide confluence, wide river with a narrow confluence, a straight river with a straight confluence inflow, a straight river with an angled confluence inflow and an angled confluence inflow in a meandering river section. These five images were converted from pixel measurements to real world distances using the known camera resolution - each pixel corresponds to a square with side length 41.1 cm.

2.2.2 Image Processing

Once converted to real world distances, the image data was processed in order to determine an accurate trend between the temperature of the confluence plume and the downstream temperature of the ambient river. A threshold of 5 °C was used on the thermal data such that any temperatures greater than 5 °C warmer than the ambient river was set to this 5 degree maximum. The images were then cropped to only include the area nearby the confluence plume. Examples of the masked image and the masked and cropped image are given in Figure 2.1.

The confluence plume was always cooler than the ambient river, likely because the tributary channel is smaller than the main river by definition and, therefore, represents closer connectivity to the groundwater and shorter exposure duration to the solar radiation [55]. Therefore, we may determine the location of the plume by detecting the minimum of temperature in each row and column of the thermal data. The detected plume, for image 950, is

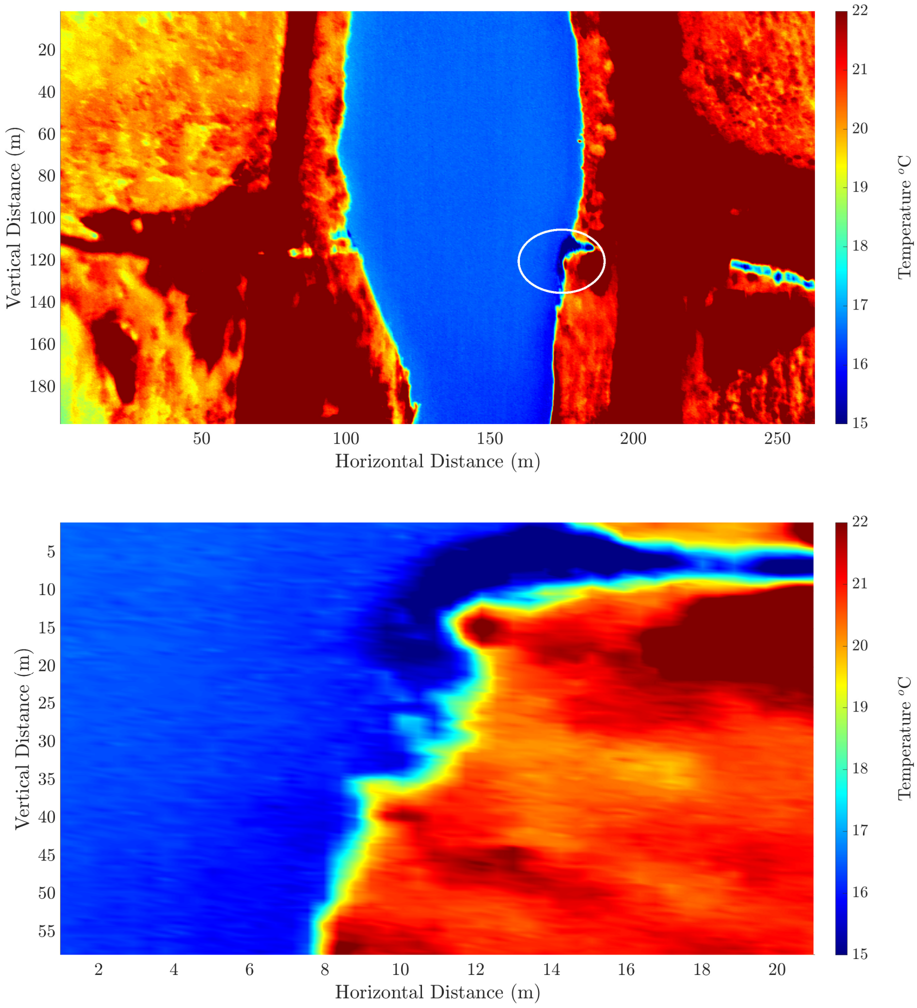

FIGURE 2.1: Examples of a masked thermal image from the Matapédia river (top) and a further cropped image to show only the tributary confluence plume (bottom). This image was taken at coordinates (48.15° N, −67.15° W).

given in Figure 2.2.

The plume was found using two distinct methods, the first is to scan along the columns of the thermal image and find the location of the thermal minimum, which will correspond to the centre of the plume in this column. Note that rows could be used instead of columns, but in these images there was insufficient thermal difference along given rows to adequately detect the plume. The second method used the centreline found in the previous method as an initial estimate, from which we consider each segment of the line formed by adjacent points. The normal line to each of these line segments is computed, the data along the normal line extracted and a single-peaked Gaussian fitted to this extracted data. The locations of the peaks are then taken as the updated centreline. This method was iterated until the centreline had converged. Note that this second method is discussed in detail in §6. The impact of the confluence plume on the ambient river was tracked

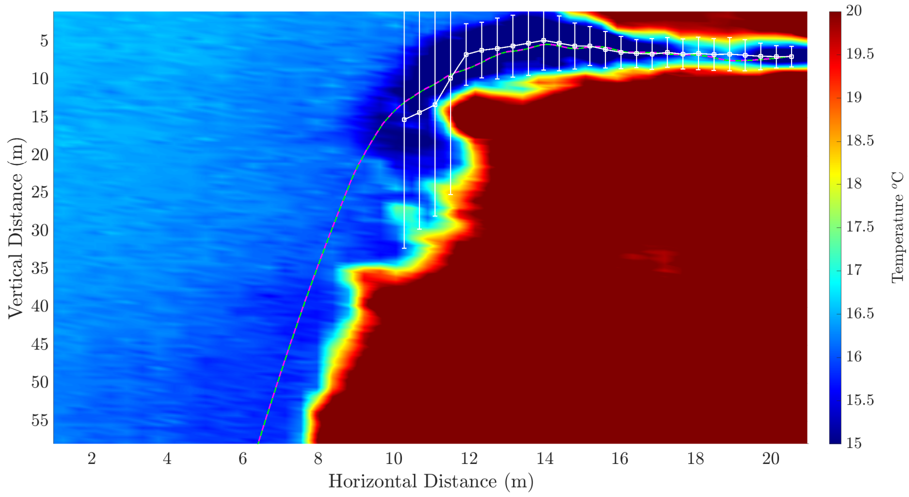

FIGURE 2.2: Plot of the detected plume in the Matapédia river, in image 950 of the sample data set. The white error barred method uses the Gaussian fitting method outline previously with the size of the error bars corresponding to one standard deviation of the fitted Gaussian, whereas the magenta and green line locates the minimum temperature in each column of pixels in the thermal imagery.

by scanning along this detected plume. Doing so, we see the temperature of the confluence plume increase as the fluid moves away from the plume inflow. This is the thermal recovery of the river. That is, we ascertain the temperature difference between the plume and the ambient river as a function of the downstream distance from the plume source. When this temperature difference returns to a small enough value, the river is said to have recovered from the impact of the confluence plume, and beyond this distance, the plume has no further *measurable* impact on the ambient river. We must also note that the river is gradually warming as we track upstream (source) to downstream (mouth), therefore this temperature deviation never truly returns to zero.

2.2.3 Data Analysis

Using the five selected images, we see that the thermal recovery of the river is a power decay law as shown in Figure 2.3. This specific example is taken from image 950 of the data set. By taking a power law of the form

$$\Delta T = T_a - T = a_1 d^{a_2} \tag{2.1}$$

where d is the distance downstream of the plume source, T_a is the ambient temperature of the river and T is the temperature of the plume a distance d from the plume source, we fit a power law to this temperature data. This power law for image 950 is shown in Figure 2.3. Note that, as discussed previously, the ambient temperature of the river increases from source to mouth. However, over the downstream distance travelled in each of these images (approximately 200m downstream) the ambient temperature is taken to be constant, and seen to be approximately constant.

By repeating the process outlined above for the remaining four selected confluence plumes, we see that these plumes all follow approximately the same trend. That is, the value of a_2 in (2.1) is approximately the same in each of the five test cases. By non-dimensionalising the temperature

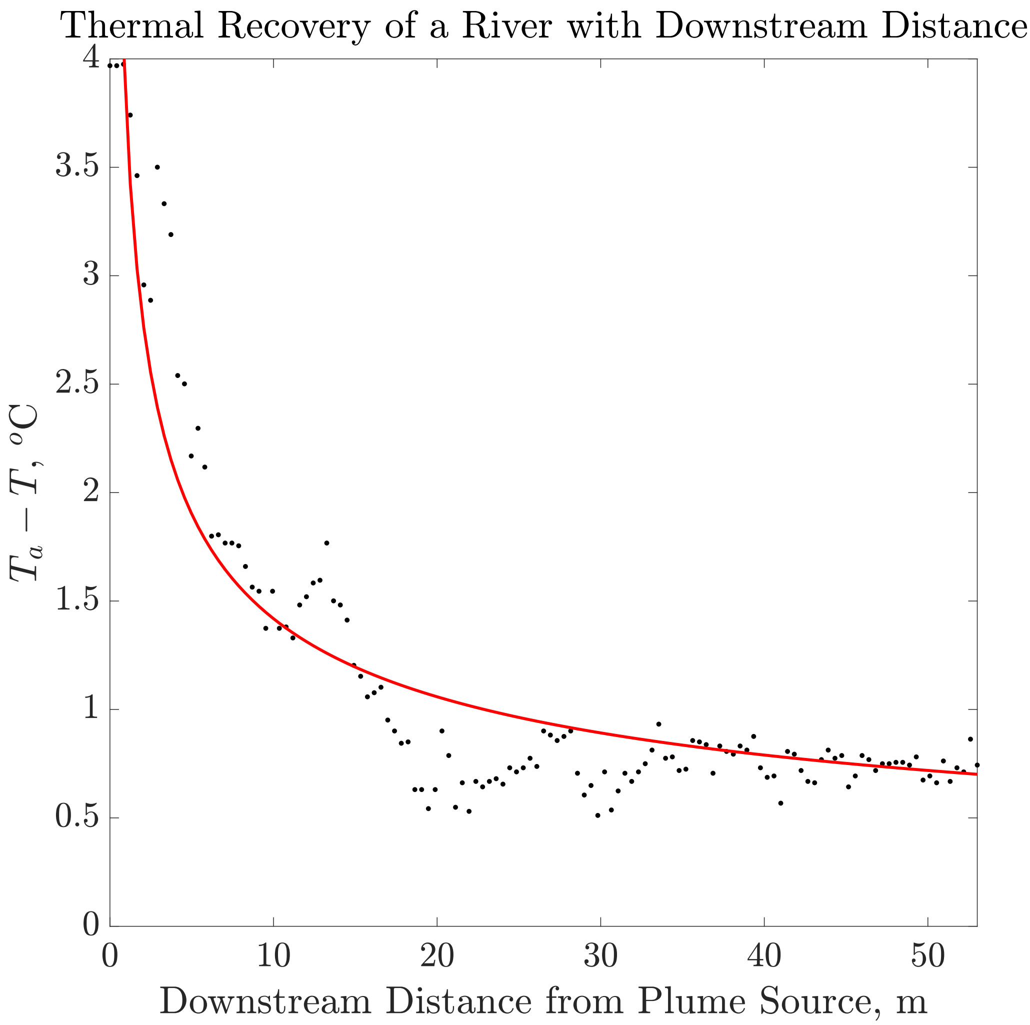

Figure 2.3: Comparison plot of the temperature deviation from the ambient temperature due to a confluence plume, and the corresponding power law approximation for data in image 950.

deviation using

$$\Theta = \frac{\Delta T}{T_{\text{ambient}}} = 1 - \frac{T}{T_a} \tag{2.2}$$

we plot the non-dimensional temperature deviation found in each plume image against the distance downstream. This is given in Figure 2.4. We see that in all cases, the slope is approximately the same which implies the same power law trend. However, it is important to note that this plot is still dimensional in the horizontal axis. To fully non-dimensionalise this, a "natural" length scale with which to rescale the distance is chosen.

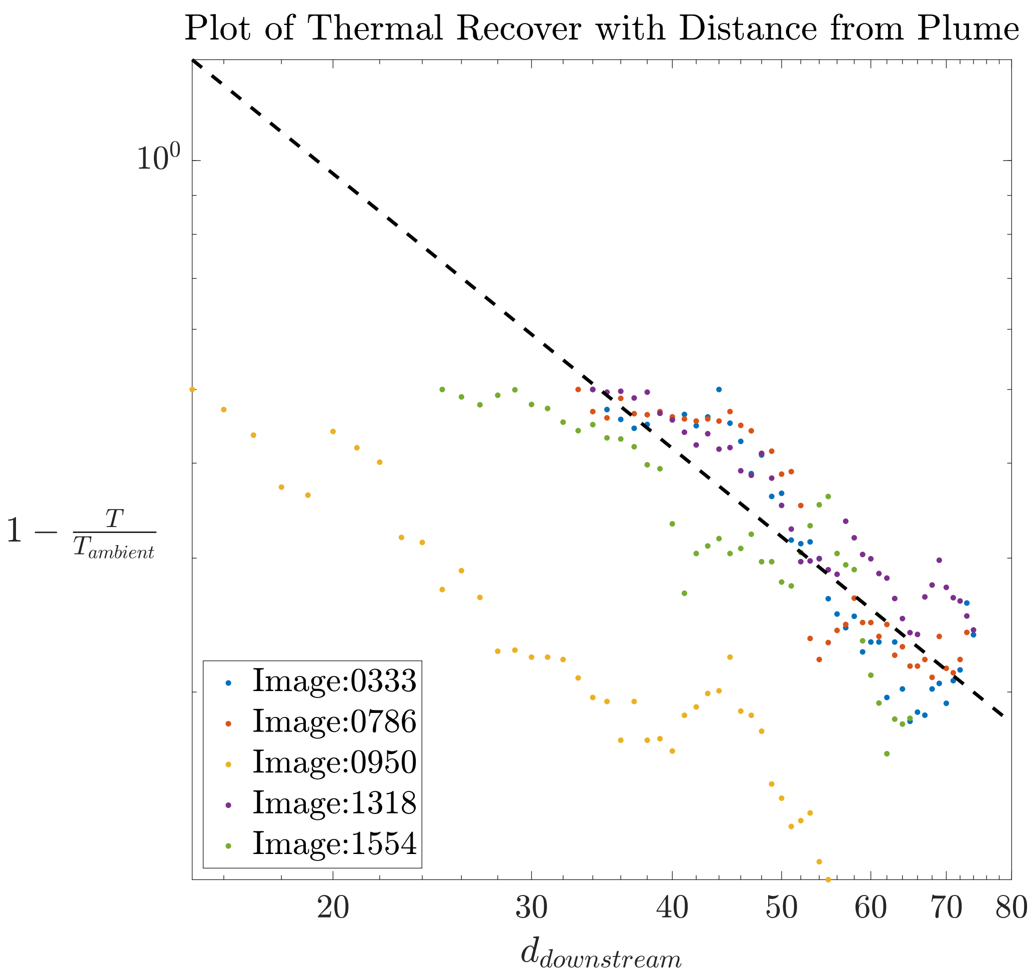

FIGURE 2.4: Plot of the thermal recovery of the Matapédia river as a function of downstream distance in five chosen plume case studies.

When non-dimensionalising height, or in this case downstream distance, from plume sources there are two natural length scales to take. These are the buoyancy length scale

$$\frac{l_b}{b_0} = \frac{b_0 w_0 g}{U_a^3} \left[\frac{T_a - T_0}{T_a} \right], \tag{2.3}$$

and the momentum length scale

$$\frac{l_m}{b_0} = \left(\frac{w_0}{U_a} \right)^2 \tag{2.4}$$

where the parameters in these length scales are given in Table 2.1. Here,

Property	Notation	Units
River Velocity	U_a	$\mathrm{m\,s^{-1}}$
Plume Source Velocity	w_0	$\mathrm{m\,s^{-1}}$
Plume Source Radius	b_0	m
Plume Source Temperature	T_0	°C
Ambient River Temperature	T_a	°C

Table 2.1: Physical quantities to non-dimensionalise the length of thermal recovery

a problem was encountered - from the thermal images, the values for river velocity and plume velocity could not be explicitly measurable. Alone, this wasn't a significant problem because quantities can be determined from gauging stations which record discharges through a section of river through time. However, at the time of collection, only two gauging stations were functioning, and neither was particularly close to the chosen plume sites. Instead, we must determine the required quantities using hydraulic geometry relationships.

2.2.4 Hydraulic Geometry

The key geometric characteristics of a river, namely depth, width and velocity, are well described using so-called "hydraulic geometry" equations [56, 57, 58, 59, 60]. These are power laws which express the above quantities in terms of the river discharge. Explicitly we have,

$$d = aQ^e, \qquad v = bQ^f, \qquad r = cQ^h \tag{2.5}$$

where $d, v,$ and r denote the river depth, velocity and width, and Q is the river discharge. The power laws given by (2.5), while empirical, are very commonly used in the literature to infer physical quantities of rivers and are well known as the "industry standard". It is important to note that this is not the standard notation used in the literature (typically w is used instead of r when referring to river width), but will be used for the extent of the discussion on hydraulic geometry to avoid the clash of notation with the later sections, where w denotes a plume velocity. The coefficients a, b, c, e, f and h are all determined quantitatively and vary river-to-river. Using an idealised model for the shape of a river channel, i.e. a cuboid, so that the river has a rectangular cross section, the cross-sectional area is given by $r \times d$ and therefore the river discharge is given by

$$Q = r \times d \times v. \tag{2.6}$$

Substituting (2.5) into this expression for discharge gives

$$Q = abcQ^{e+f+h} \tag{2.7}$$

from which we immediately see that

$$abc = 1 \text{ and } \; e + f + h = 1. \tag{2.8}$$

Therefore, it is only necessary to determine the hydraulic geometry equations for two of the three quantities. In the specific case of the thermal imagery, we are able to directly measure the width of the river, r, using pixel measurements and the known conversion between pixels and metres.

The most troublesome quantity to determine is in fact the river discharge, Q, without which no progress can be made in determining the river depth and velocity.

Discharge is known to vary with upstream catchment area as it represents the volume of water draining that area. Therefore, it is common to substitute Q for catchment area where discharge measurements are not available, and where relationships retain the same trends. Leclerc & Lapointe [61] (henceforth LL) calculated the hydraulic geometry for six rivers in the Bois-Francs region of Southern Quebec, nearby the Matapédia river. Therefore, if the width-discharge equation for the Matapédia is similar, we may simply use the width-discharge equation in LL, and thereby use their equations for depth and velocity too. Doing as was outlined above, we see that the width data of the Matapédia river was well approximated by the following power law:

$$r = 7.50Q^{0.52} \tag{2.9}$$

whereas the width law from LL is given by

$$r = 15.42Q^{0.51}. \tag{2.10}$$

These equations have similar powers, but their prefactor is noticeably different. This is due to several physical phenomena that will differ between rivers, such as sediment size, type of sediment and river slope. We note that this prefactor is more variable and less important to discerning river trends than the power in the power law. Therefore, while these prefactors have noticeable discrepancy, the behaviour of the Matapédia, at least for an initial model, may be approximated by the six rivers studied in LL. Therefore, we take the hydraulic geometry equations of LL but halve the prefactor, and apply these directly to the Matapédia river. LL only determined the equations for width and depth, the latter of which is given (with the modified prefactor) by

$$d = 0.56Q^{0.28} \tag{2.11}$$

but by using (2.8), we determine the velocity hydraulic geometry equation from the two that are known. Explicitly, the river velocity is given by

$$v = 0.23Q^{0.21}. \tag{2.12}$$

The set of equations formed by (2.10), (2.11) and (2.12) complete the hydraulic geometry of the Matapédia river. Returning to (2.3) and (2.4), we are now able to infer the river velocity, U_a, at each of the plume locations by determining the discharge at these sources in ArcGIS. The last quantity required to non-dimensionalise the data is the plume velocity, w_0.

To determine the initial plume velocity, we use a conservation of flux argument. By assuming that, at the meeting point between the river and the confluence plume, the depths of the two bodies of water are approximately equal such that we may take $d_{\text{river}} = d_{\text{plume}}$. These depth measurements may be taken from (2.11). Furthermore, we measure the river width and the plume width at the meeting point. From ArcGIS, we also find the river discharge. By conservation of flux, we argue that the ratio of discharges must equal the ratio of the cross-sectional areas. Therefore,

$$\begin{aligned} \frac{Q_{\text{river}}}{Q_{\text{plume}}} &= \frac{d \times r_{\text{river}}}{d \times r_{\text{plume}}} = \frac{r_{\text{river}}}{r_{\text{plume}}} \\ \Rightarrow Q_{\text{plume}} &= \frac{r_{\text{plume}}}{r_{\text{river}}} \times Q_{\text{river}}. \end{aligned}$$

Using (2.6), we deduce that the velocity of the plume at the meeting point, w_0 is given by

$$w_0 = \frac{Q_{\text{plume}}}{d \times r_{\text{plume}}}.$$

This gives all the required physical quantities to non-dimensionalise the x-axis given in Figure 2.4. Performing this non-dimensionalisation, choosing the momentum length scale as the length scale, we produce Figure 2.5. We see that by non-dimensionalising, four of the recovery curves are well approximated by the same power law :

$$1 - \frac{T}{T_a} = 4 \left(\frac{d_{\text{downstream}}}{l_m} \right)^{-1.1}.$$

However, the data from image 786 does not collapse onto this power law. This is because the geometry of the confluence at the location of image 786 is vastly different to the other four case studies. Differences include the curvature of the confluence path (the other four are more-or-less straight entrances), shrubbery at the inflow of the confluence plume, and a significantly wider confluence. These factors lead to this image not being well approximated by the same power law as the others. We note that the gradient exhibited by the data from image 786 is approximately the same as that of the other images, with the data having been shifted down on Figure 2.5. The similar slopes shown on Figure 2.5 suggest that the trend across river confluences is broadly similar, with the thermal recovery able to be modelled by

$$1 - \frac{T}{T_a} \propto \left(\frac{d_{\text{downstream}}}{l_m} \right)^{-1.1}. \tag{2.13}$$

2.3 Discussion

The fieldwork performed in this chapter has been to determine how far downstream a temperature change associated with an inflow of water is

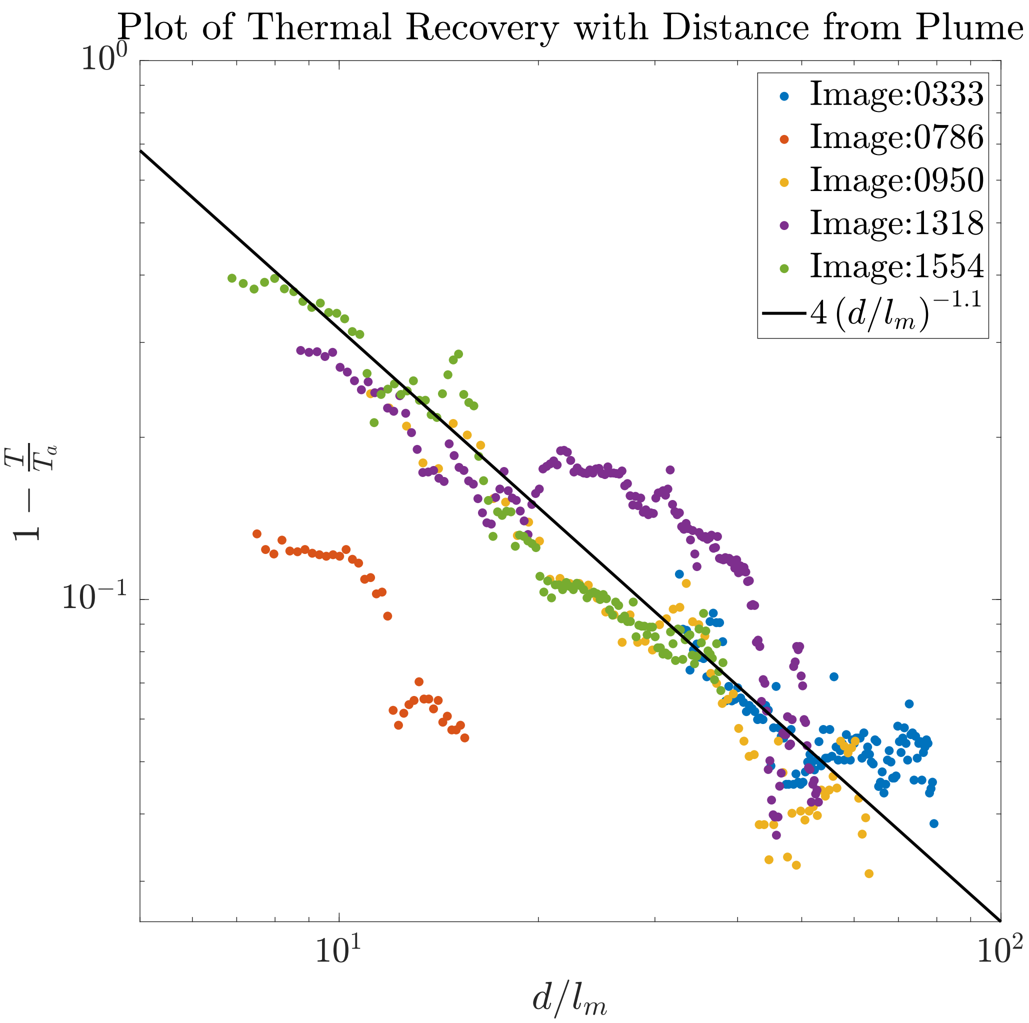

FIGURE 2.5: Non-dimensional plot of thermal recovery as a function of distance

discernible from the ambient temperature. In doing so, we saw that all five case studies from the data set acquired by Dugdale *et al.* [54] exhibit similar behaviour. Explicitly, the rivers recover from the change in temperature at a rate proportional to the distance downstream of the source of the change raised to the power 1.1 - the further from the source of the change, the smaller the change in temperature experienced by the river. This not only fits with the intuition one would naturally have but also gives a remarkably simple formula with which to estimate the thermal impact on a river due to a change in temperature, in this case from a confluence plume. By using hydraulic geometry, we found a non-dimensional power law which was accurate up to a constant of proportionality for all chosen case studies, which were chosen to give a sample of the expect river and confluence geometries, as outlined previously.

This non-dimensional power law, given in (2.13), gives a tool with which to estimate, for any confluence on the Matapédia river, the distance downstream after which the temperature change caused by the confluence is no longer measurable. From this, we are able to quickly give an estimate of the potential regions of where, for example, a thermal barrier may be created. While this is not something that can be prevented when dealing with natural confluences such as in the above work, it is critically important when considering man-made temperature changes, such as from waste water plants, heat pumps, sewage plants and so on. Note that the method outlined in this chapter could be directly applied to these scenarios, as each of the above result in a thermal plume entering a river. The difference between physical scenarios is expected to be the value of the constant of proportionality in (2.13). By knowing how far downstream these temperature changes are no longer "experienced" by the river, we determine the distance between these features that is required to ensure no combined thermal impact on the river, which would significantly reduce the change of a thermal barrier being created, and lessen the chance of damage to riverine life. While there are likely to be substantial errors associated with these estimates given the paucity of data that exists, and the need to interpolate key terms using existing standard equations, this error is unlikely to change the general trend in temperature change downstream (i.e. the power law behaviour) and is more likely to alter the relative position of individual confluence plumes (i.e. the relative magnitude).

2.4 Conclusions

In this chapter, we have examined the behaviour of the Matapédia river in response to thermal changes caused by confluence plumes. By tracking the change in temperature caused by the confluence, we detected a plume of water cooler than the ambient river. This change in temperature is then tracked downstream until the river returns to its ambient temperature. In doing so, we saw that the temperature returned to the ambient levels following a power law. This power law was seen in multiple confluences across the Matapédia river, and by non-dimensionalising with the momentum length scale, most of the data collapses to a single non-dimensional power law. The only exception to this was when a confluence was unexpectedly wide which skewed this data away from the other examples. However, in this case we saw the same trend in the data, and the data followed the expected power in the power law.

Future work could focus on the influence of channel geometry on plume extent and geometry as preliminary results in this chapter indicate that this may have an important effect on the relationship. This could be important in future to the placement of thermal discharge from power-plants, wastewater treatment plants or heat pumps because some channel geometries may extend thermal impacts for longer distances than some other geometries.

Subsequent results chapters in this thesis extend the preliminary, contextual findings of this chapter - in particular tracking the behaviour of plumes downstream of their sources. The fieldwork in this chapter was unable to vary parameters such as cross-flow velocity, number of plumes and source separation (when considering multiple plumes), all of which are the focus of §4, §5 and §6.

Chapter 3

Coalescence of Non-Interacting Plumes in a Stationary Environment

3.1 Introduction

In this chapter, we examine the coalescence of turbulent, axisymmetric plumes. Individual plumes are well studied and their behaviour is well known, but the behaviour of multiple plumes is relatively unknown. The coalescence of two laminar plumes was studied by Moses *et al.* [62, 63], whereas two coalescing turbulent plumes was first studied by Kaye & Linden [38] (henceforth KL04) and Linden [64]. A theoretical, infinite line of plumes was investigated by Rooney [65]. However, the intermediate cases are not well understood, and will be investigated here.

We begin by assuming that these plumes do not interact, and can instead merge together without entraining any fluid from one another. The case for two non-interacting plumes is given in KL04, and covers the two distinct cases where both plumes are of equal strength, and where one plume is stronger than the other. A similar argument is used to extend this modelling to an arbitrary number of equal strength plumes. To do this, we revisit the work of KL04. For consistency, identical notation to that in [38] is used.

In KL04, it was shown that the merging of two turbulent plumes with point sources at the same height, z, must be described in terms of the buoyancy fluxes of each plume, denoted $\hat{F}_1$ and $\hat{F}_2$ (by convention $\hat{F}_1 \geq \hat{F}_2$), and the horizontal separation of the plume origins, χ_0 [38]. Therefore, by dimensional analysis, the height at which these two plumes can be considered to behave as a single plume, henceforth the merging height z_m, must be described by a function of source separation, χ_0, and the ratio of buoyancy fluxes of the two plumes. Dimensionally, we see that

$$\frac{z_m}{\chi_0} = f\left(\frac{\hat{F}_2}{\hat{F}_1}\right) \tag{3.1}$$

for some function f. Therefore, it is expected that the merging height will increase linearly with the separation distance. Note that this differs from the laminar case, where the merging height increases with the square root of the separation distance [62, 63]. It is important to note that the merging height found using this non-interacting analysis is an upper bound on the merging height. This analysis does not consider the plume-to-plume interaction which would cause the plumes to entrain one another and therefore merge sooner than if they were not to interact.

The following set of notation is introduced to be consistent with the existing literature. The subscript "m" will be used to denote any quantities at the merging height, and the superscript "NI" denotes the value for the non-interacting model. A non-dimensional height, λ, is scaled on the source separation: $\lambda = \frac{z}{\chi_0}$. We also introduce a rescaled separation of the plume axes at any height, χ, where $\chi(z=0) = \chi_0$, such that $\phi = \frac{\chi}{\chi_0}$. Finally, we introduce a quantity γ, given by $\gamma = \frac{b}{\chi}$ which is the ratio of plume radius to the centreline separation between plumes at the same height. We rescale with χ instead of χ_0 to preserve this ratio at any height. Note that the plume radius, b, is the solution to the steady MTT equations given in (1.9). Explicitly, for non-interacting plumes, $b = \frac{6\alpha}{5}z$, where α is the entrainment coefficient as defined in §1.3.1. Finally, the ratio of buoyancy fluxes is denoted by $\psi = \frac{\hat{F}_2}{\hat{F}_1} \leq 1$. Two plumes will be said to be equal if $\psi = 1$, and not equal if $\psi < 1$. A schematic of the merging plumes is given in Figure 3.1.

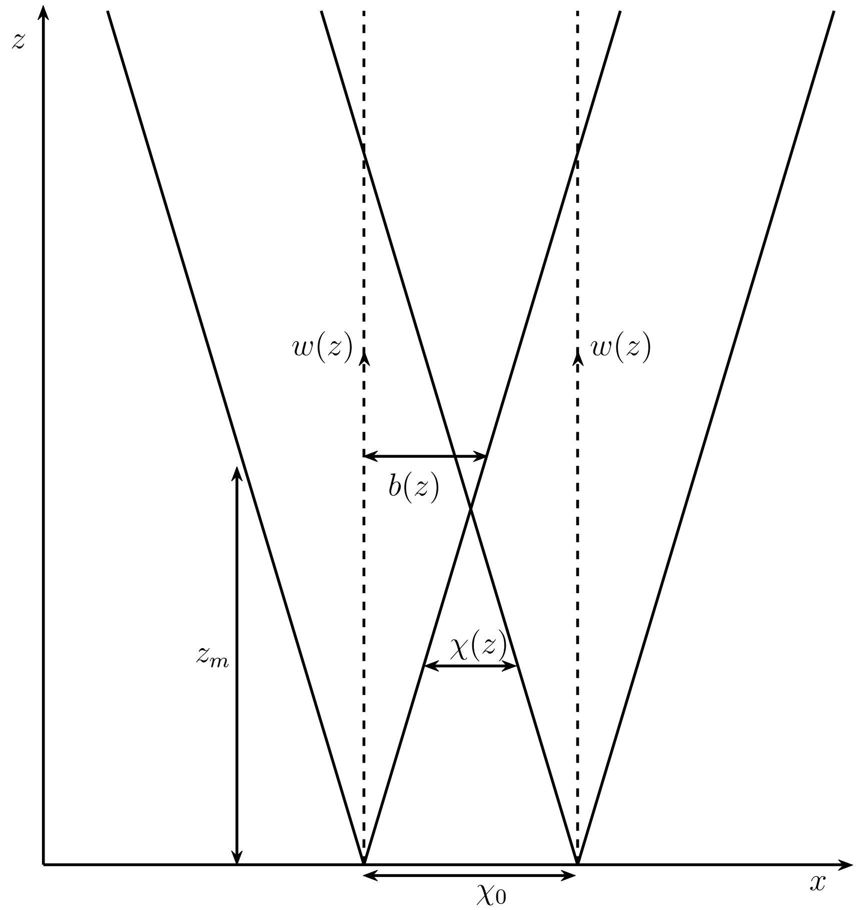

Figure 3.1: Schematic for the merging of two plumes.

3.2 Coalescence of Two Plumes

3.2.1 Two Equal Plumes

To replicate the two plume model of KL04, we consider equal plumes, $\psi = 1$, which do not interact as they merge. From MTT, we know that the ensemble average of the buoyancy and velocity of a turbulent plume are well approximated by a Gaussian, with the peak of buoyancy at the plume centreline. Therefore, it is reasonable to model the buoyancy of two turbulent plumes as a two-peaked Gaussian, with the peaks located at the centreline of each plume. Under these assumptions, we take a buoyancy profile function, for two plumes of equal strength, separated a distance χ_0 at $z = 0$, of the form

$$g'(x,z) \sim g'(0,z)E(x,z) \tag{3.2}$$

where E is given by

$$E(x,z) = \exp\left(-\left(\frac{x - \frac{\chi_0}{2}}{b}\right)^2\right) + \exp\left(-\left(\frac{x + \frac{\chi_0}{2}}{b}\right)^2\right). \tag{3.3}$$

We plot (3.3) with $\alpha = 0.1$, $\chi_0 = 1$ and $-2 \leq \frac{x}{\chi_0} \leq 2$ to give Figure 3.2. We see that E has two local maxima until a height, z_m, at which point there is a single local maxima at $x = 0$.

Therefore, the merging height is defined, as in KL04, to be the height at which the value at the centreline first becomes a local maximum. That is, the height at which there is a turning point in the gradient of E at $x = 0$. Mathematically, we find

$$z_m = \min\left\{ z \in \mathbb{R} \mid \left.\frac{\partial^2 E}{\partial x^2}\right|_{(0,z)} < 0 \right\} \tag{3.4}$$

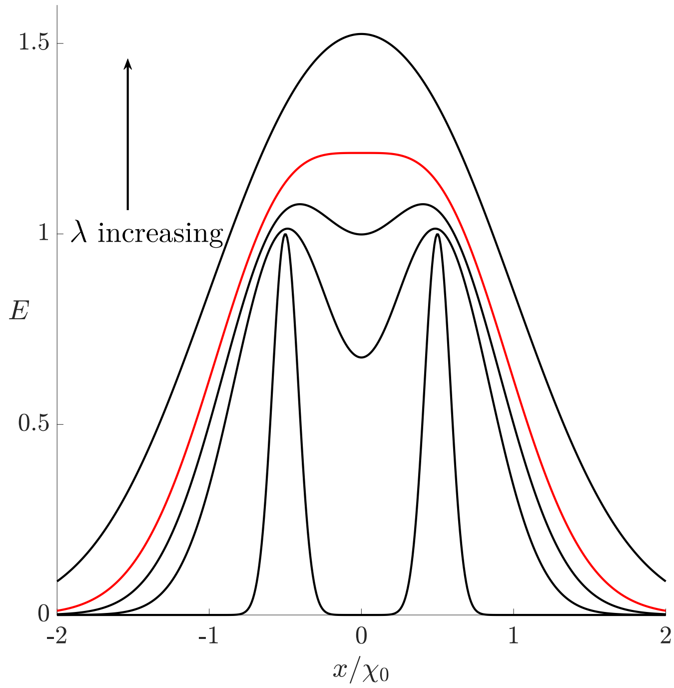

Figure 3.2: Contours of (3.3), with $\alpha = 0.1$ at $\lambda = 1, 4, 5, 5.89, 8$. The contour at the merging height is given in red.

which, using E as in (3.3), gives $b_m = \frac{\chi_0}{\sqrt{2}}$. By using $b_m = \frac{6\alpha}{5} z_m$, this may be rearranged to give

$$\frac{z_m}{\chi_0} = \lambda_m^{NI} = \frac{5}{6\alpha\sqrt{2}}. \tag{3.5}$$

Taking $\alpha = 0.1$, we see that two non-interacting plumes of equal strength will merge 5.89 source separation distances above the sources of the plumes. We note that this argument is derived under the assumption that the plumes do not interact.

3.3 An Arbitrary, Finite, Number Of Plumes

The work recapped in §3.2 was completed in KL04, and was exclusively for a system of two plumes. We extend the existing work from the literature to an arbitrary, finite, number of non-interacting plumes. We should note that, although the plumes do not interact, adding another plume to a line of two will change the merging height. This can be seen by considering Figure 3.4 where the plumes are shown to have non-zero tails in their Gaussian buoyancy profile. These non-zero contributions lead to a buoyancy profile where the newly introduced plume has an impact on the configuration, regardless of the assumption of no interaction, and therefore changes the merging height.

The plumes will be configured such that the system will always be centred around $x = 0$. In doing this, we encounter a problem. The definitions used in KL04 for equal, non-interacting, plumes to merge relies on there being a local minimum of buoyancy at $x = 0$, which will be true for an even number of plumes. An odd number of plumes, configured as above, will always have a plume centred at $x = 0$, which ensures that $x = 0$ will always be a local maximum of buoyancy. Therefore, we must treat these two cases separately.

3.3.1 An Even Number of Plumes

To preserve the symmetry of the configuration about $x = 0$, and to maintain the same plume separation distances at the source, we define an $E(x, z)$ for n (where n is even) plumes by

$$E(x,z) = \sum_{j=1}^{n/2} \left\{ \exp\left(- \left(\frac{x + \frac{2j-1}{2}\chi_0}{b} \right)^2 \right) + \exp\left(- \left(\frac{x - \frac{2j-1}{2}\chi_0}{b} \right)^2 \right) \right\}. \tag{3.6}$$

As the system is still symmetric about $x = 0$, we may directly use (3.4), which yields

$$\sum_{j=1}^{n/2} \left\{ \left(2(2j-1)^2\chi_0^2 - 4b^2 \right) \exp\left(- \frac{(2j-1)^2\chi_0^2}{4b^2} \right) \right\} = 0. \tag{3.7}$$

By dividing (3.7) by $4b^2$, and introducing $\sqrt{q} = \frac{\chi_0}{2b}$ which is proportional to the merging height given in (3.9), (3.7) becomes

$$\sum_{j=1}^{n/2} \left\{ \left(2(2j-1)^2 q - 1 \right) \exp\left(-(2j-1)^2 q \right) \right\} = 0 \tag{3.8}$$

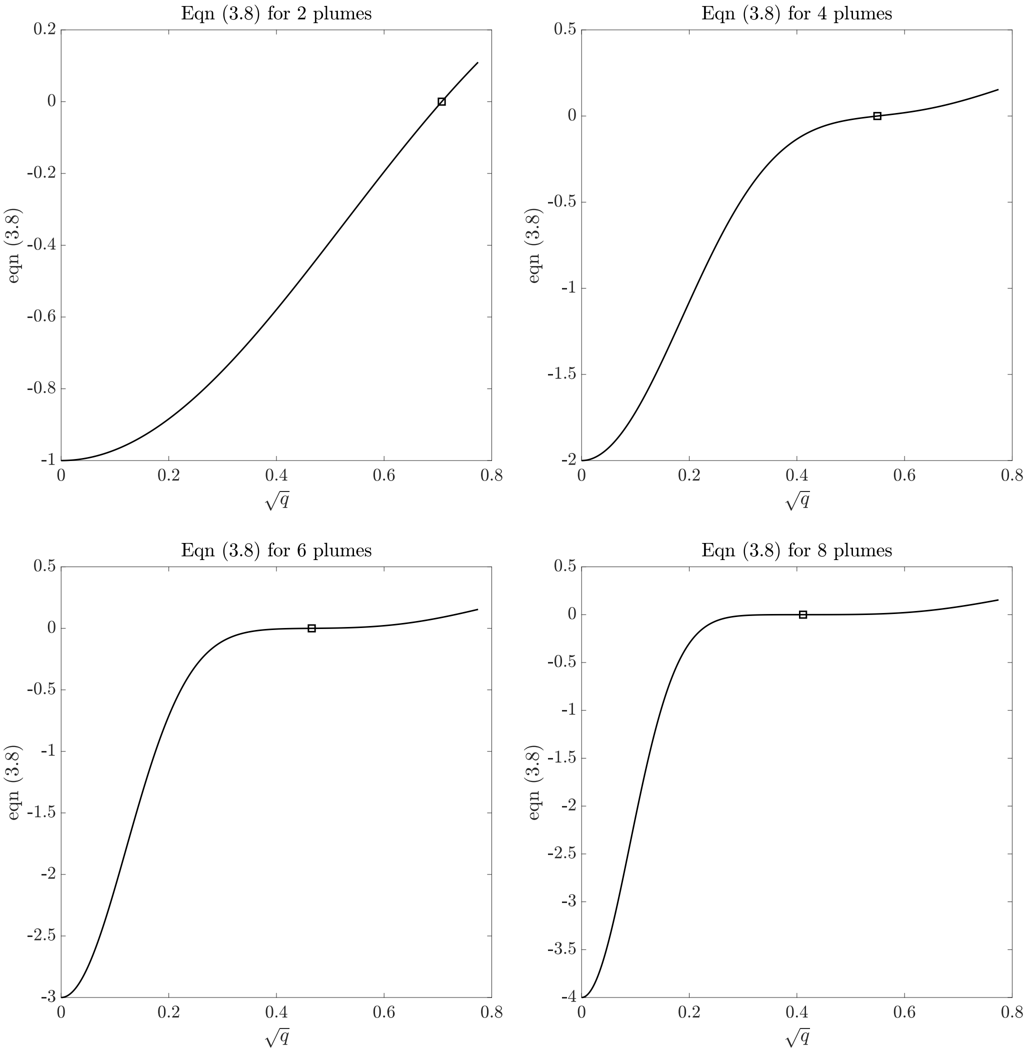

Figure 3.3: Plots of the LHS of (3.8) for $n = 2, 4, 6$ and 8 plumes. The $\sqrt{q}$ value where (3.8) is satisfied is shown by the black square.

which may be solved numerically for $\sqrt{q}$ using the "fzero" function in MATLAB which uses MINPACK's hybrd and hybrj algorithms [66]. Solutions to (3.8) are plotted for $n = 2, 4, 6$, and 8 in Figure 3.3.

Furthermore, by definition, $2\sqrt{q} = \frac{\chi_0}{b}$, and from the solutions to the steady MTT equations, $b = \frac{6\alpha}{5}z$. Hence, we find that $\frac{z}{\chi_0} = \frac{5}{12\alpha\sqrt{q}}$. Therefore, at the merging height, z_m^{NI}, we have

$$\frac{z_m^{NI}}{\chi_0} = \lambda_m^{NI} = \frac{5}{12\alpha\sqrt{q_m}}. \tag{3.9}$$

We also confirm that, when $n = 2$, $\sqrt{q_m} = \frac{1}{\sqrt{2}}$, $\lambda_m^{NI} = \frac{5}{6\alpha\sqrt{2}}$, which is the same merging height given in (3.5).

3.3.2 An Odd Number of Plumes

For an odd number of plumes, n, we define $E(x,z)$ with

$$E(x,z) = \sum_{j=-(n-1)/2}^{(n-1)/2} \exp\left(-\left(\frac{x - j\chi_0}{b}\right)^2\right) \tag{3.10}$$

which is plotted in Figure 3.4 for $\alpha = 0.1$, $\chi_0 = 1$, and $-2 \leq \frac{x}{\chi_0} \leq 2$. However, we can no longer use (3.4), since we see in Figure 3.4 that $x = 0$ is now always a local maximum. Instead, we must determine the first height at which there is no trough in the buoyancy profile. This is given by

$$z_m = \min\left\{z \in \mathbb{R} \mid \exists x \in \mathbb{R} \text{ s.t.} \frac{\partial E}{\partial x} = \frac{\partial^2 E}{\partial x^2} = 0\right\} \tag{3.11}$$

Explicitly, for three plumes, this gives

$$ue^{-u^2} + \frac{u+v}{2} e^{-\left(\frac{u+v}{2}\right)^2} + ve^{-v^2} = 0 \tag{3.12}$$

$$(2u^2 - 1)e^{-u^2} + \left(\frac{1}{2}(u+v)^2 - 1\right) e^{-\left(\frac{u+v}{2}\right)^2} + (2v^2 - 1)e^{-v^2} = 0. \tag{3.13}$$

where $u = \frac{x - \chi_0}{b}$ and $v = \frac{x + \chi_0}{b}$. Rearranging the definitions of u and v gives

$$\gamma = \frac{b}{\chi_0} = \frac{2}{v - u}. \tag{3.14}$$

Finally, by solving (3.12) - (3.13) numerically using MATLABs “fsolve” function, we find $(u_m, v_m) = (-2.39, 0.520)$ and therefore $\gamma_m = 0.686$. Recall that, by definition, $b = \frac{6\alpha}{5} z$. Rearranging for z, we find that

$$\lambda_m^{NI} = \frac{z_m}{\chi_0} = \frac{5\gamma_m}{6\alpha} \tag{3.15}$$

and for three plumes, this gives a merging height $\lambda_m^{NI} = \frac{0.572}{\alpha} = 5.72$ with an entrainment coefficient value $\alpha = 0.1$.

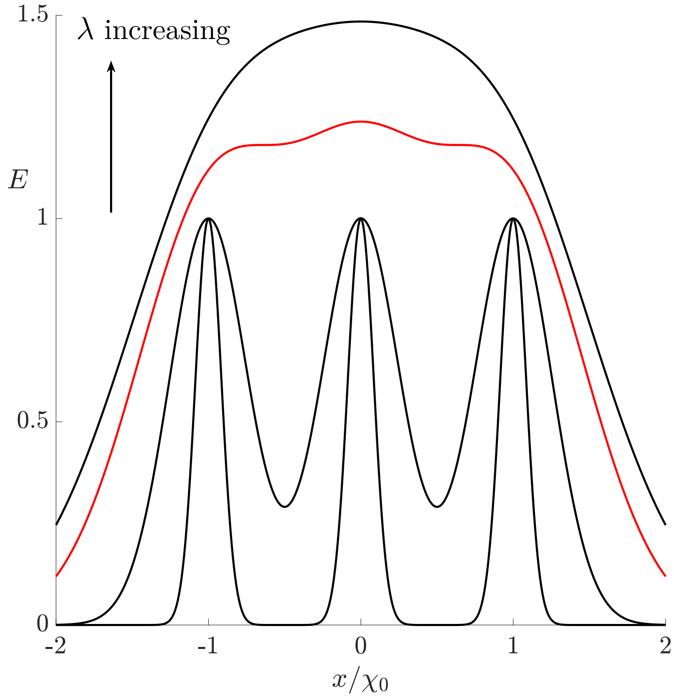

FIGURE 3.4: Contours of (3.10) with three plumes at $\lambda = 1, 3, 5.72, 7$. The contour at the merging height is given in red.

In order to generalise to n plumes in a line (where n is odd), we note that

$$\frac{x + k\chi_0}{b} = u\left(\frac{1}{2} - \frac{k}{n-1}\right) + v\left(\frac{1}{2} + \frac{k}{n-1}\right) \tag{3.16}$$

and

$$\gamma = \frac{b}{\chi_0} = \frac{n-1}{v-u} \tag{3.17}$$

where $u = \dfrac{x - \frac{n-1}{2}\chi_0}{b}$ and $v = \dfrac{x + \frac{n-1}{2}\chi_0}{b}$.

Condition (3.11) is given by

$$\sum_{j=-(n-1)/2}^{(n-1)/2} \left(u \left[\frac{1}{2} + \frac{j}{n-1} \right] + v \left[\frac{1}{2} - \frac{j}{n-1} \right] \right) \times \exp \left(- \left(u \left[\frac{1}{2} + \frac{j}{n-1} \right] + v \left[\frac{1}{2} - \frac{j}{n-1} \right] \right)^2 \right) = 0 \tag{3.18}$$

$$\sum_{j=-(n-1)/2}^{(n-1)/2} \left(2 \left(u \left[\frac{1}{2} + \frac{j}{n-1} \right] + v \left[\frac{1}{2} - \frac{j}{n-1} \right] \right)^2 - 1 \right) \times \exp \left(- \left(u \left[\frac{1}{2} + \frac{j}{n-1} \right] + v \left[\frac{1}{2} - \frac{j}{n-1} \right] \right)^2 \right) = 0. \tag{3.19}$$

By solving (3.18) - (3.19) numerically for u and v, we determine the non-dimensional merging height for an odd line of non-interacting plumes :

$$\lambda_m^{NI} = \frac{5}{6\alpha} \frac{n-1}{v_m - u_m}. \tag{3.20}$$

By solving (3.8), (3.18) and (3.19), and using (3.9) and (3.20), we find the non-interacting merging height for 2-15 plumes. These are given in Table 3.1.

An interesting pattern can be seen in Figure 3.5 - the non-interacting merging heights appear in pairs that are similarly valued. For example we see that the merging heights for $n = 2$ and $n = 3$ are similar, and $n = 4$ is similar to $n = 5$ etc. We also see that the odd numbered plumes in these pairs have a lower merging height than the corresponding even number. This is because the central plume in the odd numbered line is always a maximum, and the trough disappears last at $x = \pm \frac{\chi_0}{2}$, whereas in the even numbered lines the local minimum becomes a local maximum at $x = 0$.

No. of Plumes	$\lambda_m^{NI}\alpha$
2	0.5892
3	0.5713
4	0.7583
5	0.7460
6	0.8949
7	0.8849
8	1.0127
9	1.0041
10	1.1179
11	1.1102
12	1.2138
13	1.2068
14	1.3025
15	1.2963

TABLE 3.1: Non-dimensional merging heights of up to 15 plumes in a line.

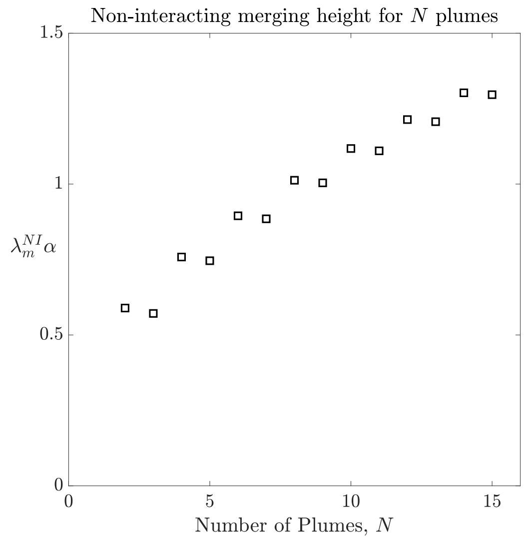

FIGURE 3.5: Plot of the non-dimensional merging heights given in Table 3.1.

3.4 The Merged Plume

This chapter has worked towards finding the height at which a number of non-interacting plumes in a line merge into a single larger plume. We now investigate the behaviour of the larger plume, henceforth the merged plume. This behaviour has been examined for two plumes, by KL04, which will now be extended to an arbitrary finite number.

3.4.1 Physical Quantities in the Merged Plume

Once the smaller, constituent plumes have merged at $z = z_m$, we have a single, larger plume, from which a number of quantities can be determined from the power law solution to the steady MTT equations (1.8) - (1.9). Recall that the subscript m denotes the value of a quantity at the merging height. Using the standard notation, we denote the radius of the plume b, the vertical velocity by w, and the modified gravity by g'. Define mass, momentum and buoyancy fluxes in terms of these quantities, as given in (1.8), using the notation of [67, 47, 38, 40, 32].

Recall that Q, M, and F define specific mass, momentum and buoyancy fluxes, which are given by

$$Q = b^2 w, \quad M = b^2 w^2, \quad F = b^2 w g'. \tag{3.21}$$

Recall also, that Q, M, and F are known from the power law solutions to MTT given in (1.8)

$$Q(z) = \frac{6\alpha}{5}\left(\frac{9\alpha}{10}\right)^{1/3} F_0^{1/3} z^{5/3}, \quad M(z) = \left(\frac{9\alpha}{10}\right)^{2/3} F_0^{2/3} z^{4/3}, \quad F(z) = F_0$$

where α is the entrainment coefficient and F_0 is the buoyancy flux at $z = 0$. Let overbarred quantities denote quantities in the merged plume. To compute the fluxes in the merged plume, we assume that all quantities are conserved from the constituent plumes. That is, for the mass flux for example

$$\bar{Q} = \sum_{\text{plumes}} Q_m.$$

Recall that it is assumed that all plumes are equal, so each Q_m is equal, and similarly for M_m and F_m. Therefore $\bar{Q} = nQ_m, \bar{M} = nM_m$ and $\bar{F} = nF_m = nF_0$. By also substituting $z = \lambda\chi_0$, we find that

$$\bar{Q} = n \times \frac{6\alpha}{5}\left(\frac{9\alpha}{10}\right)^{1/3} F_0^{1/3} z^{5/3} \tag{3.22}$$

$$\bar{M} = n \times \left(\frac{9\alpha}{10}\right)^{2/3} F_0^{2/3} z^{4/3} \tag{3.23}$$

$$\bar{F} = n \times F_0. \tag{3.24}$$

From (3.21), we see that the plume radius is given by $b = \frac{Q}{\sqrt{M}}$. Using direct substitution of (3.22) - (3.23), we find the radius of the merged plume

$$\bar{b} = \frac{6\alpha}{5} n^{1/2} z = \frac{6\alpha}{5} n^{1/2} \lambda\chi_0. \tag{3.25}$$

Note that this scales with the square root of the number of plumes, not linearly. Similarly, since $w = \frac{M}{Q}$, we see that

$$\bar{w} = \frac{5}{6\alpha}\left(\frac{9\alpha}{10}\right)^{1/3} F_0^{1/3} z^{-1/3} = \frac{5}{6\alpha}\left(\frac{9\alpha}{10}\right)^{1/3} F_0^{1/3} \lambda^{-1/3} \chi_0^{-1/3} \tag{3.26}$$

which is exactly the vertical velocity of a single plume given by (1.9), and is independent of the number of plumes. By computing $g' = \frac{F}{Q}$, we also arrive at the same expression for the modified gravity as given by (1.9):

$$\bar{g'} = \frac{5}{6\alpha}\left(\frac{10}{9\alpha}\right)^{1/3} F_0^{2/3} z^{-5/3} = \frac{5}{6\alpha}\left(\frac{10}{9\alpha}\right)^{1/3} F_0^{2/3} \lambda^{-5/3} \chi_0^{-5/3} \tag{3.27}$$

Therefore, it has been shown that the radius of the merged plume depends on the number of constituent plumes, but the modified gravity and vertical velocity are independent of the number of constituent plumes. It should be noted that there is an intrinsic assumption built into this analysis - namely that the merged plume is circular such that it obeys the MTT similarity solutions. This assumption is reasonable for a small number of plumes, but for larger n, the merged plume becomes more elliptic and therefore this assumption is no longer valid.

3.4.2 Laziness of the Merged Plume

In §1.3.1.1, the concept of a source Froude number, or a laziness parameter was introduced. This was used to classify a plume into one of three categories: forced, pure or lazy. Recall that the source Froude number is defined as

$$\mathit{\Gamma}_0 = \frac{5F_0Q_0^2}{8\alpha M_0^{5/2}} \tag{3.28}$$

where a subscript zero denotes evaluation of the quantity at $z = 0$. A plume is said to be forced if $0 < \mathit{\Gamma}_0 < 1$, pure if $\mathit{\Gamma}_0 = 1$ and lazy if $\mathit{\Gamma}_0 > 1$. For the merged plume, we would classify based not on the source Froude number, but rather using the Froude number at the merging height. This will henceforth be referred to as the merged Froude number, and is defined by

$$\mathit{\Gamma}_m = \frac{5\bar{F}_m\bar{Q}_m^2}{8\alpha \bar{M}_m^{5/2}} \tag{3.29}$$

where a subscript m refers to evaluation at $z = z_m$. Direct substitution of (3.22) - (3.24) into (3.29) gives

$$\mathit{\Gamma}_m = n^{1/2} \tag{3.30}$$

which, for any line of plumes (assuming that a line can not be a single plume), will be greater than one. Therefore, the merged plume will always be lazy. This result - that the merged plume is always lazy - suggests that the merged plume will always have a velocity deficit when compared to its buoyancy. The merged plume would then exhibit the behaviour shown by a single lazy plume. The plume would taper in, or neck, to correct for the velocity deficit, then continue to rise with the expected conical shape.

We also note that this result follows physical intuition since a lazy plume typically occurs from a distributed, or area, source whereas a pure plume is assumed to occur from a point source. At the merging height, the merged plume has non-zero mass, momentum and area from which it follows that the source is an area source and would be expected to be either lazy or forced. Using (3.26), we see that the centreline velocity of the plume does not increase when the plumes merge, but (3.25) shows that the area of the plume increases. Therefore, a velocity deficit would be expected which leads to a lazy plume.

3.4.3 Virtual Origin of the Merged Plume

It was discussed in §1.3.1.1 that the MTT power law solutions are not valid for general initial conditions. The power law assumes that there is a "point source of buoyancy", which is represented by non - zero buoyancy flux but zero momentum and mass fluxes at the origin, $z = 0$. We see, from (3.22) - (3.24), that the merged plume will not satisfy this condition. Instead, it will have a so-called "distributed source", which has the more general condition of finite mass, momentum and buoyancy flux at the source. In order to match the merged plume to a power law solution, we must compute the virtual origin.

To do this, we note that the merged plume is a single plume which, if we treat the merging height as its origin, has source conditions $Q(z = z_m) = \bar{Q}$, $M(z = z_m) = \bar{M}$ and $F(z = z_m) = \bar{F}$. The virtual origin of a lazy plume was studied by Hunt & Kaye [40], and since the merged plume has been shown, by (3.30), to always be lazy, this work is directly applicable. The working required to arrive at this asymptotic formula for the virtual origin is replicated below.

Recall that the rate of change of mass flux of a plume was given by (1.1), which for convenience we rewrite below:

$$\frac{\mathrm{d}Q}{\mathrm{d}z} = 2\alpha M^{1/2}$$

where α is the entrainment coefficient. We non-dimensionalise (1.1) using $Q = q^*\bar{Q}$, $M = m^*\bar{M}$, and $z = z^*\frac{5}{6\alpha}\frac{\bar{Q}}{\bar{M}^{1/2}} = z^*\frac{5}{6\alpha}\bar{b}_m$, where $\bar{b}_m = \bar{b}(z = z_m)$, to give

$$\frac{3}{5}\frac{\mathrm{d}q^*}{\mathrm{d}z^*} = {m^*}^{\frac{1}{2}}. \tag{3.31}$$

Integrating (3.31) gives

$$z^* = \frac{3}{5}\int_1^{q^*} \frac{\mathrm{d}\bar{q}}{{m^*}^{\frac{1}{2}}} \tag{3.32}$$

and recalling from (1.14) that

$${m^*}^{\frac{5}{2}} = \Gamma_m({q^*}^2 - 1) + 1 \Rightarrow {m^*}^{\frac{1}{2}} = \Big(\Gamma_m({q^*}^2 - 1) + 1\Big)^{1/5},$$

We express (3.32) as

$$\begin{aligned} z^* &= \frac{3}{5}\int_1^{q^*} \Gamma_m^{-1/5}\left(\bar{q}^2 - \left(\frac{\Gamma_m - 1}{\Gamma_m}\right)\right)^{-1/5}\mathrm{d}\bar{q} \\ &= \frac{3}{5}\int_1^{q^*} \Gamma_m^{-1/5}\left(\bar{q}^2 - \xi\right)^{-1/5}\mathrm{d}\bar{q} \\ &= \frac{3}{5}\int_1^{q^*} \Gamma_m^{-1/5}(\bar{q})^{-2/5}\left(1 - \tau\right)^{-1/5}\mathrm{d}\bar{q}. \end{aligned} \tag{3.33}$$

By binomially expanding $(1-\tau)^{-1/5}$, (3.33) gives

$$\begin{aligned}
\Gamma_m^{1/5} z^* &= \frac{3}{5}\int_1^{q^*} (\bar{q})^{-2/5}\left\{1+\frac{1}{5}\tau+\frac{1}{5}\frac{6}{5}\frac{1}{2!}\tau^2+\dots\right\}\mathrm{d}\bar{q} \\
&= \frac{3}{5}\int_1^{q^*}\left\{(\bar{q})^{-2/5}+\frac{\xi}{5}(\bar{q})^{-12/5}+O\left((\bar{q})^{-17/5}\right)\right\}\mathrm{d}\bar{q} \\
&= {q^*}^{3/5}-(1-\frac{3}{35}\xi-\frac{9}{425}\xi^2-\dots)+O\left({q^*}^{-7/5}\right) \\
&\sim {q^*}^{3/5}-(1-\delta) \qquad (3.34)
\end{aligned}$$

where

$$\delta=\frac{3}{35}\xi+\frac{9}{425}\xi^2+\dots=\frac{3}{5}\sum_{k=1}^{\infty}\left\{\frac{\xi^k}{5^{k-1}k!(10k-3)}\prod_{j=1}^{k}(1+5(j-1))\right\}. \qquad (3.35)$$

Rearranging (3.34), we see that

$$\begin{aligned}
{q^*}^{3/5} &= \Gamma_m^{1/5}z^*+(1-\delta)=\Gamma_m^{1/5}(z^*+z^*_{\mathrm{avs}}) \\
\Rightarrow q^* &= \Gamma_m^{1/3}\left(z^*+z^*_{\mathrm{avs}}\right)^{5/3} \qquad (3.36)
\end{aligned}$$

where $z^*_{\mathrm{avs}}=\Gamma_m^{-1/5}(1-\delta)$. In the limit as $\Gamma_m\to\infty$, $\xi=\frac{\Gamma_m-1}{\Gamma_m}\to 1$ and $\delta\to 0.147$, and therefore $z^*_{\mathrm{avs}}\to 0.853\Gamma_m^{-1/5}$. This is the asymptotic limit for the location of the virtual origin, where z^*_{avs} is the dimensionless distance below the source of the merged plume that the virtual origin is located. That is, the virtual origin is at $z^*=-z^*_{\mathrm{avs}}$. Outside of this limit, (3.34) must be computed directly.

We find the dimensional virtual origin by multiplying by $\frac{5}{6\alpha}\frac{\bar{Q}_m}{\bar{M}_m^{1/2}}=n^{1/2}\lambda_m\chi_0$. Explicitly, this gives

$$z_{\mathrm{avs}}=0.853\Gamma_m^{-1/5}n^{1/2}\lambda_m\chi_0 \qquad (3.37)$$

but, since $\Gamma_m = n^{1/2}$, this reduces to

$$z_{\text{avs}} = 0.853 n^{2/5} \lambda_m \chi_0. \tag{3.38}$$

It is important to note that this is the distance below the merging height, not the distance below the source of the constituent plumes. Explicitly, z_{avs} is the distance below z_m, not $z = 0$. To find the distance below the sources of the constituent plumes, we subtract the merging height, $\lambda_m \chi_0$, from (3.38) to give

$$z_{\text{virt}} = (0.853 n^{2/5} - 1) \lambda_m \chi_0. \tag{3.39}$$

This gives the asymptotic limit for the location of the virtual origin of the merged plume, as a function of only the number of plumes, the merging height and the source separation. We note again that this result implicitly assumes that the cross-section of the merged plume is circular. As discussed in §3.4.1, this assumption breaks down when the number of plumes is large.

3.4.4 Impact of the Merged Plume on the Environment

Finally, we investigate the effects of the merged plume on the ambient environment. Physically, this could be a change in the temperature, salinity, or causing a flow in the environment. We will limit ourselves to a change in temperature. Recall that, when deriving the MTT steady plume equations, the Boussinesq approximation was used. This assumes that density differences are small, and therefore negligible except in buoyancy terms. These density differences are captured in the modified gravity, g'.

As we consider the merged plume, we find the distance from the merging height that the thermal effects are negligible. This is denoted z_{neg}, and the corresponding modified gravity by g'_{neg}. We deem the effects to be negligible if they fall to $\zeta\%$ of the value at the source. Mathematically, this is given by

$$g'_{\mathrm{neg}} = \frac{\zeta}{100} g'_m. \tag{3.40}$$

Using (3.27) and simplifying, we see that

$$\begin{aligned} z_{\mathrm{neg}}^{-5/3} &= \frac{\zeta}{100} z_m^{-5/3} \\ \Rightarrow z_{\mathrm{neg}} &= \left(\frac{100}{\zeta}\right)^{3/5} z_m. \end{aligned} \tag{3.41}$$

This is the distance from the merging height, to determine the distance from the source of the constituent plumes, we subtract z_m:

$$z_* = \left[\left(\frac{100}{\zeta}\right)^{3/5} - 1\right] z_m$$

which may be non-dimensionalised by dividing through by χ_0 to give

$$\lambda_* = \left[\left(\frac{100}{\zeta}\right)^{3/5} - 1\right] \lambda_m. \tag{3.42}$$

This is a non-dimensional formula for the vertical distance, from the constituent plumes, that the buoyancy effects of these plumes has dropped to $\zeta\%$ of the ambient value, and is therefore deemed negligible.

We note that this quantity could also be reached using the conservation of tracer concentration flux. Suppose that we have a tracer of concentration $c(z)$, which is conserved in the plume. The conservation of tracer may then be given by

$$\frac{\mathrm{d}}{\mathrm{d}z}(b^2 wc) = 0, \tag{3.43}$$

which states that there is no tracer outside of the plume. This is identical to (1.3) in a uniform environment with tracer concentration replaced by modified gravity, g'. Therefore, from here, the argument follows as above.

3.5 Arrays of Non-Interacting Plumes

Currently, all existing work on merging plumes has assumed that the plumes are configured in a line. We extend the work on plumes in a line to plumes in an $n \times n$ grid by generalising the formulation of the buoyancy profile E. We continue to assume that plumes do not interact, and therefore can generalise E immediately to another spatial dimension. This generalisation is demonstrated for a 2×2 grid, and will then be used for an arbitrary $n \times n$ grid. As before, we configure the system such that all plumes are separated by a distance χ_0; all plumes are of equal strength, and the configuration is centred at the origin. This again requires us to treat the odd and even cases separately.

3.5.1 A 2×2 Grid of Plumes

The schematic of a 2×2 grid of plumes is given in Figure 3.6.

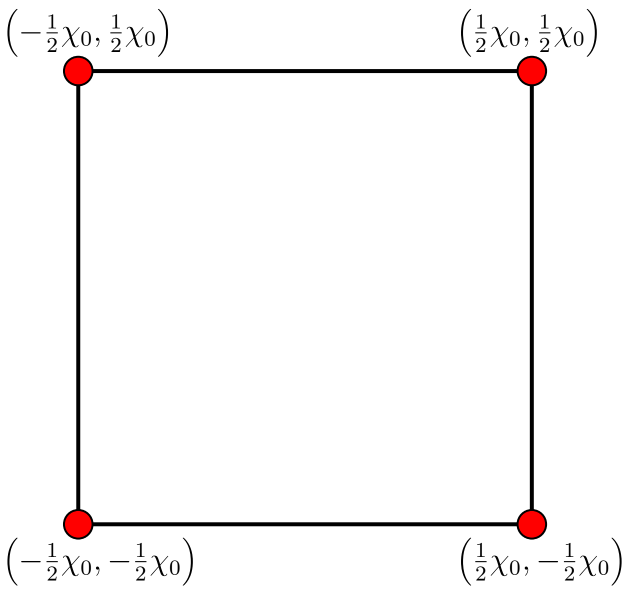

Figure 3.6: Schematic of the 2×2 array of plumes.

As with the non-interacting plumes in a line §3.2, define the buoyancy profile by

$$g'(x,y,z) \sim g'(0,0,z)E(x,y,z) \tag{3.44}$$

where $E(x,y,z)$ is defined by

$$E(x,y,z) =$$
$$\exp\left(-\left(\frac{(x-\frac{1}{2}\chi_0)^2+(y-\frac{1}{2}\chi_0)^2}{b^2}\right)\right)+\exp\left(-\left(\frac{(x-\frac{1}{2}\chi_0)^2+(y+\frac{1}{2}\chi_0)^2}{b^2}\right)\right)$$
$$+\exp\left(-\left(\frac{(x+\frac{1}{2}\chi_0)^2+(y-\frac{1}{2}\chi_0)^2}{b^2}\right)\right)+\exp\left(-\left(\frac{(x+\frac{1}{2}\chi_0)^2+(y+\frac{1}{2}\chi_0)^2}{b^2}\right)\right).$$

By noting that each row and each column of this grid is a line of two plumes, they will merge simultaneously at the merging height for two plumes in a line. Therefore it is reasonable to expect that the entire grid will have merged at approximately the merging height of two plumes in a line. Using the same argument as §3.2, we would expect the plumes to have merged when there is a single peak, and from the symmetry of the system, we see that the origin is the last place to switch from a minimum to a maximum. Therefore, we use an analogous merging condition to determine when an even 2D array has merged. We seek the first height, z, where the origin is no longer a local minima. This is when the Hessian of E vanishes at the origin:

$$H := \frac{\partial^2 E}{\partial x^2}\frac{\partial^2 E}{\partial y^2} - \left(\frac{\partial^2 E}{\partial x \partial y}\right)^2 = 0 \quad \text{at } (x,y)=(0,0). \tag{3.45}$$

By computing (3.45), we see that $b_m = \frac{\chi_0}{\sqrt{2}}$. Using the steady plume radius, $b_m = \frac{6\alpha}{5}z_m$, we find that $\lambda_m = \frac{5}{6\alpha\sqrt{2}}$. We note that this is identical to (3.5), meaning that a non-interacting 2×2 grid merges at the same height as a line of two plumes. This is confirmed by evaluating (3.5.1) at various heights, and plotting the corresponding contours, as shown in Figure 3.7. We see that the first height at which a single peak appears is indeed given by (3.5).

This method is now generalised to a general $n \times n$ grid.

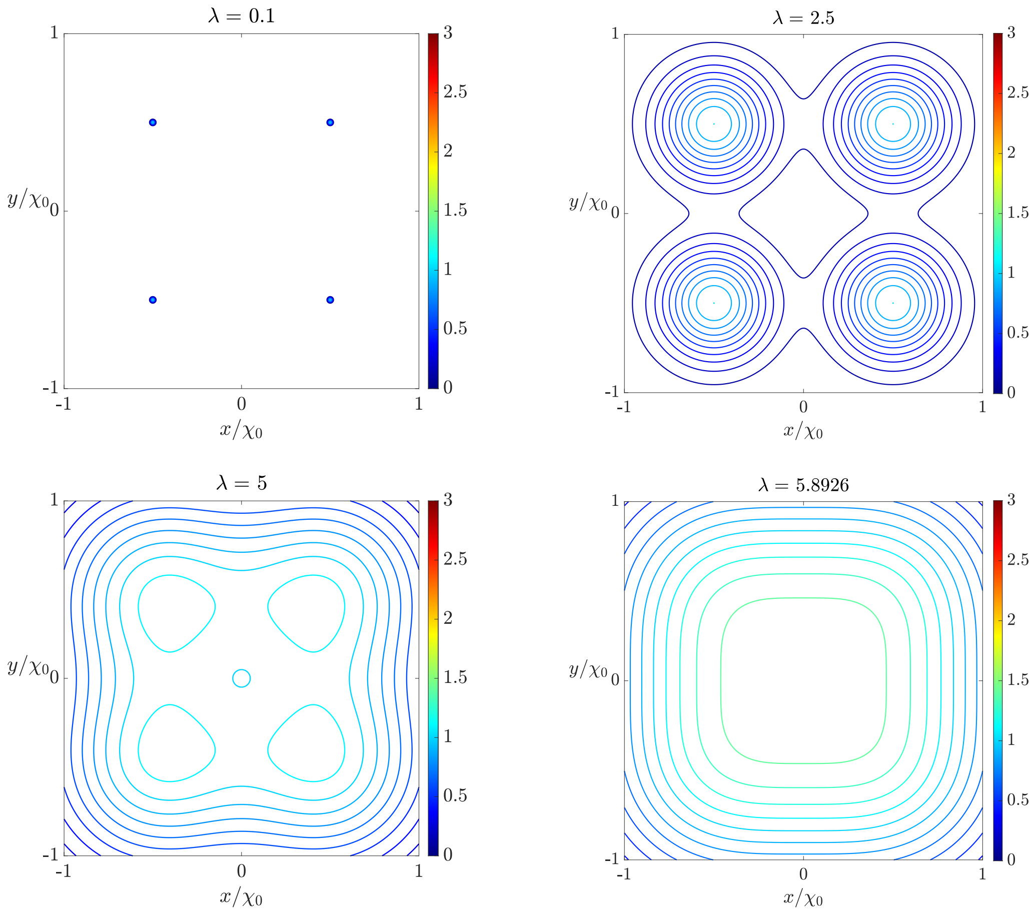

Figure 3.7: Plot of contours of (3.5.1) with $\chi_0 = 1$ and $\alpha = 0.1$ at $\lambda = 0.1, 2.5, 5$ and $\frac{5}{6\alpha\sqrt{2}}$. We see the four peaks merging, and have fully merged in the both right panel.

3.5.2 An Even Grid of Plumes

We define $E(x,y,z)$ as

$$\begin{aligned} E(x,y,z) = \sum_{j=1}^{n/2}\sum_{i=1}^{n/2} \Bigg\{ &\exp\left(-\frac{(x-\frac{2i-1}{2}\chi_0)^2+(y-\frac{2j-1}{2}\chi_0)^2}{b^2}\right) \\ &+\exp\left(-\frac{(x+\frac{2i-1}{2}\chi_0)^2+(y-\frac{2j-1}{2}\chi_0)^2}{b^2}\right) \\ &+\exp\left(-\frac{(x-\frac{2i-1}{2}\chi_0)^2+(y+\frac{2j-1}{2}\chi_0)^2}{b^2}\right) \\ &+\exp\left(-\frac{(x+\frac{2i-1}{2}\chi_0)^2+(y+\frac{2j-1}{2}\chi_0)^2}{b^2}\right)\Bigg\}. \end{aligned} \tag{3.46}$$

where n is the number of plumes. As with the 2×2 grid, we expect each row and column of an $n\times n$ grid to merge at the same height as a line of n. Therefore it is again reasonable to expect the $n\times n$ grid to merge at approximately the merging height for a line of n.

By computing the Hessian of E using (3.45), we find a general condition for an $n\times n$ grid to have merged. Using $q=\frac{\chi_0^2}{4b^2}$, this condition is

$$\begin{aligned} &\left\{\sum_{j=1}^{n/2}\sum_{i=1}^{n/2}\Big(2(2j-1)^2q-1\Big)\exp\Big[-q\Big((2j-1)^2+(2i-1)^2\Big)\Big]\right\}\times \\ &\left\{\sum_{j=1}^{n/2}\sum_{i=1}^{n/2}\Big(2(2i-1)^2q-1\Big)\exp\Big[-q\Big((2j-1)^2+(2i-1)^2\Big)\Big]\right\}=0. \end{aligned} \tag{3.47}$$

Taking $n=2$, we find $2b^2-\chi_0^2=0$ which leads to $\lambda_m^{NI}=\frac{5}{6\alpha}\frac{1}{\sqrt{2}}$. That is, we return to the 2×2 grid case above. Solving (3.47) numerically shows that, for any even $n\times n$ grid, we arrive very closely to the behaviour of n plumes in a line. By comparing the merging heights for a line of n plumes and an $n\times n$ grid of plumes, we arrive at the same merging height for up to 500 decimal places, as determined using Maple. A simulation of (3.46) with $n=4$ is given in Figure 3.8, using $\alpha=0.1$ and $\chi_0=1$, we show that the plume has merged at the height given in Table 3.1.

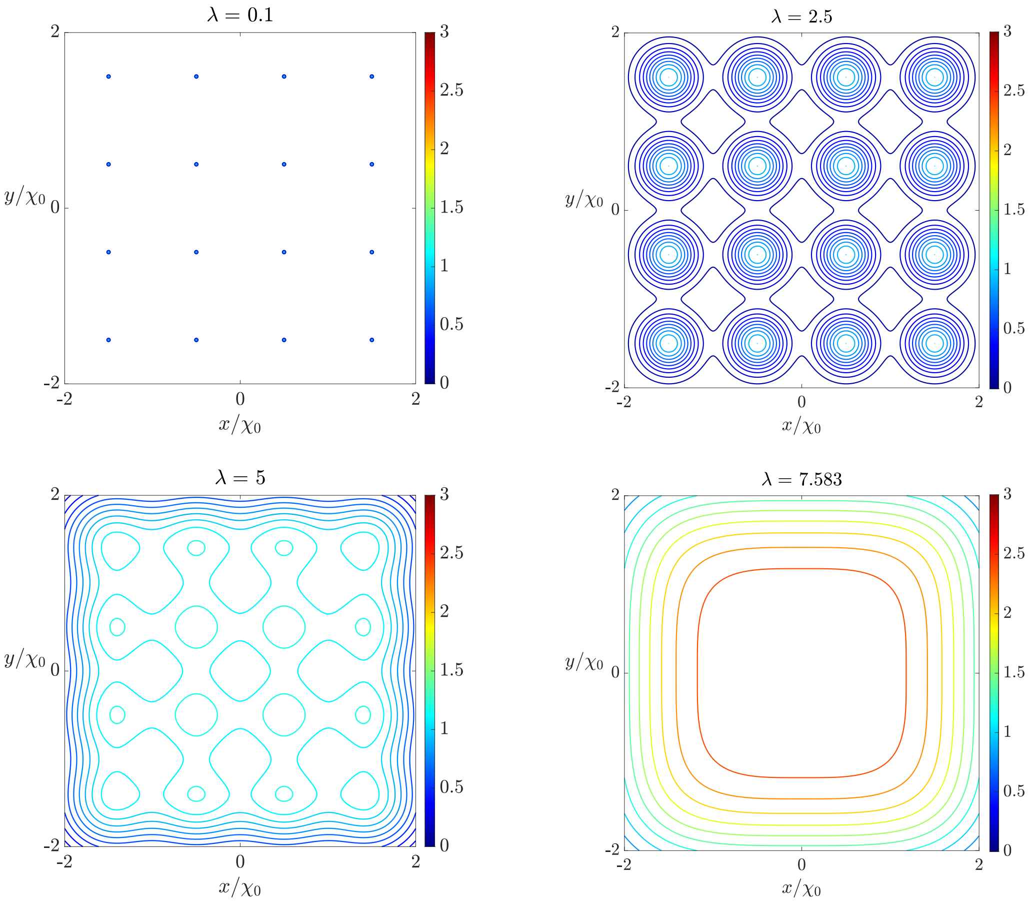

FIGURE 3.8: Contour plots of (3.46) with $n = 4$ is given in using $\alpha = 0.1$ and $\chi_0 = 1$ at $\lambda = 0.1, 2.5, 5$ and $\frac{0.7583}{\alpha}$. The final panel is at the merging height for four plumes in a line. We see the first height at which a single peak occurs at $\lambda = 7.58$ as expected.

3.5.3 An Odd Grid of Plumes

As before, we configure the grid of plumes such that it is centred around the origin. This gives E of the form

$$E(x, y, z) = \sum_{j=-\frac{n-1}{2}}^{\frac{n-1}{2}} \sum_{k=-\frac{n-1}{2}}^{\frac{n-1}{2}} \left\{ \exp\left(-\frac{(x + k\chi_0)^2 + (y + j\chi_0)^2}{b^2} \right) \right\} \quad (3.48)$$

As with the odd plumes in a line, we will have a plume centred at the origin. Therefore, we cannot use the same argument as the even array of plumes. Instead, we use a method analogous to that used in §3.3.2. Explicitly, we naturally extend to 3D with the following merging condition:

$$\frac{\partial E}{\partial x} = 0, \quad \frac{\partial E}{\partial y} = 0, \quad H = \frac{\partial^2 E}{\partial x^2}\frac{\partial^2 E}{\partial y^2} - \left(\frac{\partial^2 E}{\partial x \partial y}\right)^2 = 0 \tag{3.49}$$

which may be computed directly to give

$$\sum_{j=-R}^{R}\sum_{k=-R}^{R}(u+kv)\exp(-\Delta) = 0 \tag{3.50}$$

$$\sum_{j=-R}^{R}\sum_{k=-R}^{R}(w+jv)\exp(-\Delta) = 0 \tag{3.51}$$

$$\begin{aligned}&\sum_{j=-R}^{R}\sum_{k=-R}^{R}\Big((2u+2kv)^2-2\Big)\exp(-\Delta)\\ \times&\sum_{j=-R}^{R}\sum_{k=-R}^{R}\Big((2w+2jv)^2-2\Big)\exp(-\Delta)\\ -&\left\{\sum_{j=-R}^{R}\sum_{k=-R}^{R}(2u+2kv)(2w+2jv)\exp(-\Delta)\right\}^2 = 0\end{aligned} \tag{3.52}$$

where $R = \frac{n-1}{2}$, $u = \frac{x}{b}$, $v = \frac{\chi_0}{b}$, $w = \frac{y}{b}$ and $\Delta = (u+kv)^2 + (w+jv)^2$. By solving (3.50) - (3.52) numerically, we return approximately to the merging heights found for the odd plumes in a line in §3.3.2. Therefore, we have shown that, for a non-interacting $n \times n$ grid of plumes, the merging height is close to the merging height of n plumes in a line. This was validated by direct comparison for up to 500 decimal places, again using Maple. An example of the merging of 3×3 grid of non-interacting plumes is given in Figure 3.9.

3.5.4 A Non-Interacting Triangle of Plumes

Finally, consider an equilateral triangle of non-interacting plumes, where each edge has length χ_0, as shown in Figure 3.10.

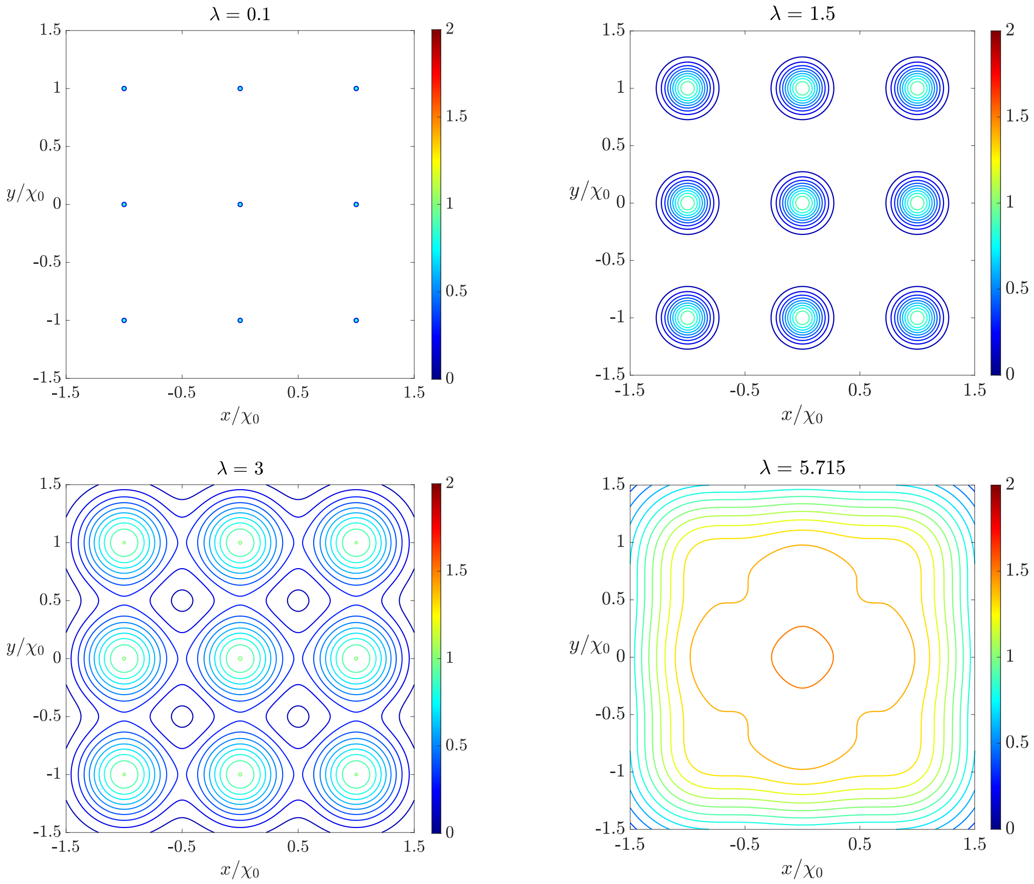

Figure 3.9: Plot of contours of (3.48) with $\chi_0 = 1$ and $\alpha = 0.1$ at $\lambda = 0.1, 1.5, 3$ and 5.715. We see the three peaks merging, and have fully merged in the both right panel.

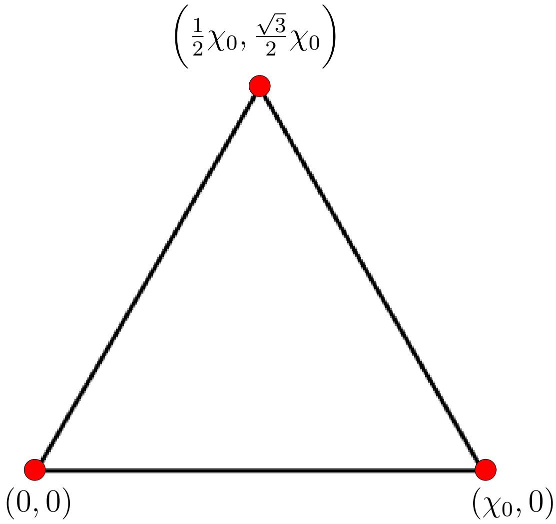

FIGURE 3.10: Schematic of the equilateral triangular plume configuration.

Again, we assume that these plumes are of equal strength, and therefore define $E(x, y, z)$ as

$$\begin{aligned} E(x,y,z) = \exp\left(-\frac{x^2+y^2}{b^2}\right) + \exp\left(-\frac{(x-\chi_0)^2+y^2}{b^2}\right) \\ + \exp\left(-\frac{\left(x-\frac{\chi_0}{2}\right)^2+\left(y-\frac{\sqrt{3}}{2}\chi_0\right)^2}{b^2}\right). \end{aligned} \tag{3.53}$$

In previous cases, we have determined that the plume configuration has merged when there is a single local maximum. We argue that the last place to merge would be the centre of the triangular configuration. Here the centre is defined as the centroid: the location of the centre of mass of the triangle, and is located at $(x, y) = \left(\frac{\chi_0}{2}, \frac{\sqrt{3}\chi_0}{6}\right)$. Therefore, the condition for the configuration to have merged is given by

$$H := \frac{\partial^2 E}{\partial x^2}\frac{\partial^2 E}{\partial y^2} - \left(\frac{\partial^2 E}{\partial x \partial y}\right)^2 = 0 \quad \text{at } (x,y) = \left(\frac{\chi_0}{2}, \frac{\sqrt{3}\chi_0}{6}\right) \tag{3.54}$$

which may be solved analytically to give

$$\left(\frac{(2\chi_0^2 - 6b^2)}{b^4} \exp\left(-\frac{\chi_0^2}{3b^2} \right) \right)^2 = 0. \tag{3.55}$$

This gives $\chi_0 = b\sqrt{3}$ and therefore $\lambda_m^{NI} = \dfrac{5}{6\alpha\sqrt{3}}$.

3.6 Summary

In this chapter, we have extended the work of Kaye & Linden [38] from two non-interacting, turbulent plumes to an arbitrary, finite number of non-interacting, turbulent, plumes. The dimensional argument of Kaye & Linden shows that the merging height of a line of plumes increases linearly with the source separation. We have found an expression for the merging height of a line of plumes, which is valid assuming that they don't interact as they merge. This is a very strong assumption, and will only be approximately true in practice. Therefore, the work done in this chapter is only able to find an upper bound on the merging height of a line of plumes. We would expect the plumes to interact as they merge, so the merging height would be lower than this non-interacting model predicts.

As well as extending the work of [38], we compute the value of physical quantities at the merging height, z_m, including the plume radius assuming that the merged plume is circular at the merging height. This approximation breaks down for large n, but is reasonable for small n. We have shown that at the merging height, the plume radius, b_m, increases with the square root of the number of plumes, but the modified gravity g'_m and vertical velocity, w_m, are both independent of the number of plumes. A merged Froude number, which is defined similarly to the source Froude number but evaluated at the merging height, was determined and, using the values of the physical quantities at the merging height, shown to always be greater than one for a line of plumes. That is, once the plumes have merged, the merged plume will always be “lazy”. This allowed an asymptotic limit for the virtual origin to be calculated, by using the theory developed in [40]. We also find a non-dimensional distance from the source of the plumes after which the environmental impact is negligible. This is done by arguing that the impact of a plume on the environment is primarily captured in the buoyancy, and therefore in the modified gravity. This distance is of particular interest as it shows how far away from the sources of a line of plumes that this line of plumes will have an effect on the environment, and is seen to scale approximately linearly for small n, and approximately like $\sqrt{n}$ for large n.

Finally, we investigated the behaviour of non-interacting arrays of plumes. By extending the model for a non-interacting line of plumes to 2D, we determine a merging height for a general $n \times n$ grid. We saw that the merging height of an $n \times n$ grid is very similar to a line of n plumes. This is also extended to an equilateral triangle, and a non-dimensional merging height is found for this triangular configuration. We discovered that the equilateral triangle had a merging height lower than both two and three plumes in a line. This suggests that the additional dimension has a notable effect on the merging height. We note that this additional plume, forming the triangle from the line, is closer to the merging point - the centroid of the triangle - than the corners of the $n \times n$ grid are to the centre of the square. This supports that the triangular array should merge lower than these $n \times n$ grids, as was shown in §3.5.4.

Chapter 4

Coalescence of Interacting Plumes in a Stationary Environment

4.1 Introduction

The existing work on the merging of two non-interacting plumes [38, 64, 68] was extended in §3. This extended the modelling from two non-interacting plumes to an arbitrary, finite number of plumes; in a line, a grid and a triangle. There is a significant assumption made in this earlier modelling: that the plumes can merge together without interacting. This is not the case in practice, as the plumes would entrain one another, forcing them to merge closer to their sources than if they do not interact. Therefore, while the non-interacting model may be used to find an upper bound on the merging height, any realistic model must account for the interaction between plumes. Kaye & Linden [38] (KL04) modelled the merging height of two interacting plumes, which we extend to an arbitrary, finite number of plumes and to two special cases of arrays of plumes: a 2×2 square grid and an equilateral triangle. we first recap the interacting model of KL04, who considered interacting plumes of equal strength.

4.2 Two Interacting Plumes

We again seek to find the merging height of a configuration of plumes. To determine this merging height for two plumes, we recreate the work of KL04. Recall that this merging height, denoted z_m, is the height at which a configuration of plumes behave as a single plume. For consistency with previous work, we introduce the following notation. The subscript m denotes any quantity evaluated at $z = z_m$. A non-dimensional height, $\lambda = \frac{z}{\chi_0}$, a rescaled separation of plume axes at any height, $\phi = \frac{\chi}{\chi_0}$, and a rescaled plume radius, $\gamma = \frac{b}{\chi}$, are also introduced, where χ is the separation of the plume axes at a height and $\chi_0 = \chi(z = 0)$. Recall that the steady plume radius, for a single plume, is given by $b = \frac{6\alpha}{5}z$, which was found by Morton, Taylor and Turner (MTT) [33]. An idealised configuration is given in Figure 4.1 showing the buoyancy profile at three chosen heights, including at the merging height.

It has been shown experimentally that the velocity field outside a plume is approximately horizontal [69]. Gaskin *et al.* [70] also determined, experimentally, that the entrainment field from individual plumes may be added to give an overall entrainment field provided the ambient velocities are of the same order as the entrainment velocity. Combining these results, the mean entrainment velocity field of two plumes, separated a distance χ, over a horizontal plane across the two plumes may be modelled as two vertical line sinks of strength $-m(z)$ with origins at $x = 0$ and $x = \chi$.

$m(z)$ is determined by noting that the strength of a line sink is given by

$$m(z) = \int_0^{2\pi} \alpha b(z) w(z) \, \mathrm{d}\theta,$$

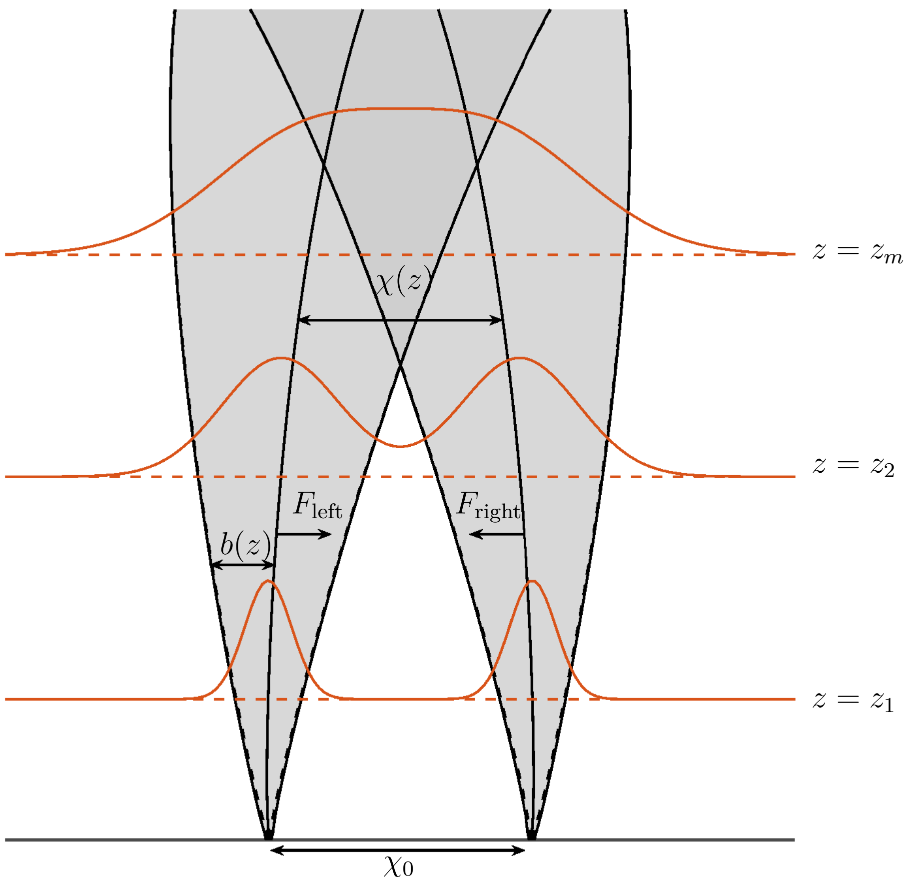

Figure 4.1: Schematic of two interacting plumes. The dashed blue lines show the edges of the plume, the solid black lines represent the centreline of the plumes and solid red lines show the buoyancy profile at the height shown by the dashed red lines.

where w is the vertical velocity of fluid inside a plume, α is the entrainment coefficient, and b is the steady plume radius. This gives $m = 2\pi b\alpha w$ assuming that the entrainment coefficient, α is constant, and there is no θ dependence in b and w.

We determine the entrainment of one plume on the other by modelling the centreline of each plume as an infinite line sink of strength $-m(z)$, analogous to an infinite, current carrying wire. In this case, the entrainment felt by the left plume from the right is given by $F_{\text{left}} = \frac{m}{2\pi}\frac{1}{r'}$, where $r'(z)$ is the distance between the two plumes. That is $F_{\text{left}} = \frac{b\alpha w}{\chi}$. By symmetry, the entrainment felt by the right plume from the left is given by $F_{\text{right}} = -\frac{b\alpha w}{\chi} = -F_{\text{left}}$. Therefore, the velocity of the right plume relative to the left, u, is given by

$$u = F_{\text{right}} - F_{\text{left}} = -\frac{2b\alpha w}{\chi}. \tag{4.1}$$

By assuming that each plume is passively advected by the entrainment field of the other, the rate of change of axial separation with height is given by the ratio of vertical to horizontal velocities at the plume axis. This gives

$$\frac{\mathrm{d}\chi}{\mathrm{d}z} = \frac{\frac{\mathrm{d}\chi}{\mathrm{d}t}}{\frac{\mathrm{d}z}{\mathrm{d}t}} = \frac{u}{w} = -\frac{1}{w}\frac{2b\alpha w}{\chi}. \tag{4.2}$$

Using $\chi = \chi_0\phi$, $z = \lambda\chi_0$ and $b = \frac{6\alpha}{5}\lambda\chi_0$, and noting that $\phi(z=0) = 1$ and $\lambda(z=0) = 0$, we find

$$\begin{aligned} \frac{\mathrm{d}\phi}{\mathrm{d}\lambda} &= -\frac{12\alpha^2\lambda}{5\phi} \\ \Rightarrow \phi^2 - 1 &= -\frac{12}{5}\alpha^2\lambda^2. \end{aligned} \tag{4.3}$$

Recall that $\gamma = \dfrac{b}{\chi}$. By evaluating at the merging height and substituting, we find that

$$\gamma_m = \frac{6\alpha\lambda_m\chi_0/5}{\chi_0\phi_m}.$$

That is,

$$\phi_m = \frac{6\alpha\lambda_m}{5\gamma_m}. \tag{4.4}$$

Evaluating (4.3) at the merging height and substituting (4.4) into (4.3) gives

$$\lambda_m \alpha = \left(\frac{36}{25\gamma_m^2} + \frac{12}{5}\right)^{-1/2}. \tag{4.5}$$

Finally, recall that $\gamma_m = \frac{1}{\sqrt{2}}$ from (3.5), and therefore (4.5) becomes

$$\lambda_m^I = \frac{1}{\alpha}\sqrt{\frac{25}{132}} \approx \frac{0.435}{\alpha}. \tag{4.6}$$

This is the merging height from the KL04 interacting model and was supported by experiments performed in [38, 68]. Note that the use of $\gamma_m = \frac{1}{\sqrt{2}}$ found in §3 is appropriate as the correction for the merging of these plumes assumes only passive advection [38].

4.3 An Arbitrary, Finite Number of Interacting Co-Linear Plumes

The existing models for interacting plumes in a stationary environment only consider two plumes. The existing work is now extended to an arbitrary, finite number of co-linear plumes. In the modelling by Kaye & Linden, the fact that there were only two plumes meant that the plumes were both entrained equally by the other. This is not the case for more than two plumes. We outline the method for three co-linear plumes using a similar method, but require a modified model for an arbitrary number of co-linear plumes.

4.3.1 Three Interacting Co-Linear Plumes

We consider three co-linear, equispaced, plumes of equal strength. For convenience, centre the sources of these plumes at $x = -\chi_0$, $x = 0$ and $x = \chi_0$. These plumes are modelled by line sinks of strength $-m(z)$ located at $x = -\chi(z)$, $x = 0$ and $x = \chi(z)$ respectively.

To follow the same method as §4.2, we must find the mean entrainment field. Recall that the entrainment of one plume on another can be shown to take the form

$$F = -\frac{m}{2\pi}\frac{1}{r'} \tag{4.7}$$

where $r'(z)$ is the distance between the plumes being considered. A derivation of this formula is given in §8.2. From [70], we are able to add these contributions. That is, the entrainment felt by one plume from two plumes would be the sum of each F from (4.7). Therefore, the entrainment felt by the leftmost plume, denoted F_{left}, is given by

$$F_{\text{left}} = b\alpha w\left(\frac{1}{\chi} + \frac{1}{2\chi}\right)$$

where χ and 2χ are the distances from the leftmost plume to the middle and the rightmost respectively. By symmetry, we also have

$$F_{\text{right}} = -b\alpha w\left(\frac{1}{\chi} + \frac{1}{2\chi}\right) = -F_{\text{left}}$$

for the rightmost plume. Finally, the central plume is entrained equally, but in opposite directions, by the leftmost and rightmost plumes. Explicitly,

$$F_{\text{mid}} = 0.$$

The central plume is, by definition, at the midpoint between the left and right plume, and has zero horizontal velocity component. Therefore, we expect the centreline of this central plume to be the horizontal position where this line of plumes will merge. Hence, we do not define u as in the two plume case, where u was the velocity of the right plume relative to the left. Instead, we define u to be the velocity of the central plume relative to the left. That is,

$$u = F_{\text{mid}} - F_{\text{left}},$$

or by symmetry, the velocity of the central plume relative to the right

$$u = F_{\text{right}} - F_{\text{mid}}.$$

In either case, we arrive at

$$\frac{\mathrm{d}\chi}{\mathrm{d}z} = -\frac{1}{w}\frac{3b\alpha w}{2\chi}, \tag{4.8}$$

where χ is the distance between the left and central, or right and central plumes, or more generally

$$\frac{\mathrm{d}\chi}{\mathrm{d}z} = \frac{u}{w}. \tag{4.9}$$

(4.8) is solved using the same method as §4.2 and we see that

$$\lambda_m \alpha = \left(\frac{36}{25\gamma_m^2} + \frac{9}{5}\right)^{-1/2}. \tag{4.10}$$

Unlike the two plume case, γ_m - which is defined by $\gamma_m = \frac{b}{\chi}|_{z=z_m}$ and is given by (3.14) - is not known analytically. Recall that, from §3.3, a numerical solution for γ_m was found for an odd number of co-linear plumes. For three plumes, we found that $\gamma_m = 0.686$. Again, using the non-interacting value of γ_m is appropriate as we assume only passive advection. Substituting this into (4.10), we determine a merging height of

$$\lambda_m^I \approx \frac{0.454}{\alpha}. \tag{4.11}$$

We now generalise this method to n interacting co-linear plumes. As in the non-interacting case, we consider the odd and even cases separately.

4.3.2 An Interacting Line of an Odd Number Of Plumes

4.3.2.1 Special Case: Three Plumes

Suppose, as above, that we have three interacting co-linear plumes, configured with sources

$$(-\chi_0, 0), (0, 0), (\chi_0, 0).$$

To develop a more general model, for the merging of an arbitrary number of plumes, we model these plumes using line sinks positioned at

$$(\chi_1, z), (\chi_2, z), (\chi_3, z)$$

where $\chi_2 = 0$ and $\chi_3 = -\chi_1$.

Using (4.7), we see that the entrainment velocity of plume 1, located at (χ_1, z), is given by

$$F_1 = b\alpha w \left(\frac{1}{\chi_3 - \chi_1} + \frac{1}{\chi_2 - \chi_1} \right) \tag{4.12}$$

$$= b\alpha w \left(\frac{1}{-2\chi_1} + \frac{1}{-\chi_1} \right) \tag{4.13}$$

$$= b\alpha w \left(-\frac{3}{2\chi_1} \right). \tag{4.14}$$

Similarly, for plume 2, we see

$$F_2 = b\alpha w \left(\frac{1}{\chi_3 - \chi_2} + \frac{1}{\chi_1 - \chi_2} \right) \tag{4.15}$$

$$= b\alpha w \left(\frac{1}{-\chi_1 - \chi_2} + \frac{1}{\chi_1 - \chi_2} \right) = b\alpha w \left(\frac{1}{-\chi_1} + \frac{1}{\chi_1} \right) = 0 \tag{4.16}$$

and by symmetry about $x = 0$, we take $F_3 = -F_1$. For each plume, we assume that the change in centreline position with height is given by

$$\frac{\mathrm{d}\chi_k}{\mathrm{d}z} = \frac{F_k}{w}. \tag{4.17}$$

Explicitly, for three plumes, the system of equations are

$$\frac{\mathrm{d}\chi_1}{\mathrm{d}z} = -\frac{3b\alpha}{2\chi_1} \tag{4.18}$$

$$\frac{\mathrm{d}\chi_2}{\mathrm{d}z} = 0 \tag{4.19}$$

$$\chi_3 = -\chi_1 \tag{4.20}$$

subject to $\chi_1(0) = -\chi_0, \chi_2(0) = 0$ and $\chi_3(0) = \chi_0$. Solving (4.18) - (4.20) analytically, we find that

$$\chi_1 = \left(\chi_0^2 - \frac{9\alpha^2}{5}z^2\right)^{\frac{1}{2}} \tag{4.21}$$

$$\chi_2 = 0 \tag{4.22}$$

$$\chi_3 = -\left(\chi_0^2 - \frac{9\alpha^2}{5}z^2\right)^{\frac{1}{2}}. \tag{4.23}$$

From this analytic solution, we determine the buoyancy profile, E, defined by

$$\begin{aligned} E(x,z) = \exp\left(-\left[\frac{x-\chi_1}{b}\right]^2\right) + \exp\left(-\left[\frac{x-\chi_2}{b}\right]^2\right) \\ + \exp\left(-\left[\frac{x-\chi_3}{b}\right]^2\right). \end{aligned} \tag{4.24}$$

By substituting the analytic solution for χ_1, χ_2 and χ_3, the buoyancy profile is given by

$$
\begin{aligned}
E(x,z) = \exp\left(-\left[\frac{x-(\chi_0^2-\frac{9\alpha^2 z}{5})^{1/2}}{\frac{6\alpha z}{5}}\right]^2\right) + \exp\left(-\left[\frac{x}{\frac{6\alpha z}{5}}\right]^2\right) \\
+ \exp\left(-\left[\frac{x+(\chi_0^2-\frac{9\alpha^2 z}{5})^{1/2}}{\frac{6\alpha z}{5}}\right]^2\right).
\end{aligned}
\tag{4.25}
$$

The merging height of this system is found by applying the method outlined in §3.3.2. We find that $\lambda_m^I \alpha = 0.454$, which is the same merging height found in §4.3.1. We may also solve (4.18) - (4.20) numerically. By doing so, and determining the number of peaks given in (4.24), we further validate this model by arriving at a merging height of $\lambda_m^I \alpha = 0.454$, as expected from the analytic solution.

4.3.2.2 General Case: An Odd Number of Plumes

Suppose that we have n, where n is odd, interacting co-linear plumes, configured such that the line is centred about $x = 0$. This requires the plumes to be centred at

$$
\left(-\frac{n-1}{2}\chi_0, 0\right), \left(-\frac{n-3}{2}\chi_0, 0\right), \ldots, (0,0), \ldots, \left(\frac{n-1}{2}\chi_0, 0\right).
$$

This is modelled as a line of n line sinks of strength $-m(z)$ at

$$
(\chi_1, z), (\chi_2, z), \ldots, \left(\chi_{(n+1)/2}, z\right), \ldots, (\chi_n, z).
$$

These plumes are labelled, left to right, as plume 1,2,...n. For plume 1, we see that the entrainment velocity is given by

$$
\begin{aligned}
F_1 &= b\alpha w\left(\frac{1}{\chi_n-\chi_1} + \frac{1}{\chi_{n-1}-\chi_1} + \ldots \frac{1}{\chi_2-\chi_1}\right) && (4.26) \\
&= b\alpha w \sum_{j=2}^{n} \frac{1}{\chi_j-\chi_1} && (4.27)
\end{aligned}
$$

For an arbitrary plume number, k, where $1 < k \leq \frac{n-1}{2}$ we find that the entrainment velocity is given by

$$F_k = b\alpha w\left(\frac{1}{\chi_n - \chi_k} + \cdots + \frac{1}{\chi_{k+1} - \chi_k} - \left[\frac{1}{\chi_k - \chi_{k-1}} + \ldots \frac{1}{\chi_k - \chi_1}\right]\right) \tag{4.28}$$

$$= b\alpha w\left(\underbrace{\sum_{j=k+1}^{n} \frac{1}{\chi_j - \chi_k}}_{\text{right of } k^{th} \text{ plume}} - \underbrace{\sum_{j=1}^{k-1} \frac{1}{\chi_k - \chi_j}}_{\text{left of } k^{th} \text{ plume}}\right) \tag{4.29}$$

$$= b\alpha w \sum_{\substack{j=1 \\ j\neq k}}^{n} \frac{1}{\chi_j - \chi_k}. \tag{4.30}$$

By the symmetry of the system, we also have $\chi_n = -\chi_1$, $\chi_{n-1} = -\chi_2$ and in general $\chi_{n-k+1} = -\chi_k$ for $k \leq \frac{n-1}{2}$. Finally, $\chi_{(n+1)/2} = 0$, again by the symmetry of the configuration. This yields the following system of equations

$$\frac{\mathrm{d}\chi_k}{\mathrm{d}z} = \frac{F_k}{w} \quad \text{for } 1 \leq k \leq \frac{n-1}{2} \tag{4.31}$$

$$\chi_k = 0 \quad \text{for } k = \frac{n+1}{2} \tag{4.32}$$

$$\chi_k = -\chi_{n+1-k} \quad \text{for } \frac{n+3}{2} \leq k \leq n \tag{4.33}$$

subject to $\chi_k(0) = -\left(\frac{n-(2k-1)}{2}\right)\chi_0$. The system of equations given by (4.31) - (4.33) can be solved numerically to give the centreline of each plume as a function of height. There will not, in general, be an analytic solution for these centrelines, so the merging height can not be found using the method outlined in §3.3.2. Instead, the buoyancy profile, E, is computed and the number of peaks found using MATLAB peak detection which determines all local maxima by comparison of neighbouring values. Once this number of peaks has reduced from n to 1, the system of plumes has merged, and the lowest height for which this is seen is the merging height, z_m^I. This merging height may then be non-dimensionalised as previously, to give $\lambda_m^I = \frac{z_m^I}{\chi_0}$.

However this model overlooks the physical behaviour of the system. Implicit in this model is the assumption that the plumes all merge simultaneously, at the same height. While this is true for $n = 3$, this isn't the case in general. Instead, we see that the outer two plumes merge first (that is, plumes 1 and 2 merge, as do plumes $n-1$ and n), then these merged plumes merge with the adjacent plume and so on until a single plume remains. Furthermore, the strength of these merged plumes is no longer the same as the plumes that have yet to merge. Indeed, in §3.4, it was shown that the radius of the merged plume at the merging height, b_m, increases with the number of plumes that have merged. Explicitly, we showed in (3.25) that $b_m = \sqrt{n}b$, where b is the radius of an "unmerged" plume at the merging height.

Therefore, we initially have n equal co-linear plumes. These n plumes will merge into $n-2$ because plumes 1 and 2 have merged, as have plumes n and $n-1$. Each merged plume is $\sqrt{2}$ times stronger than each of the remaining $n-2$ plumes (see §3.4 or KL04). Hence, we must consider the merging behaviour of non-equal plumes.

Consider two plumes, with specific buoyancy fluxes F_1 and F_2, where $F_1 \geq F_2 \, \forall z$. We define the ratio of fluxes, $\psi = \frac{F_2}{F_1} \leq 1$. It was shown, in KL04, that the buoyancy profile of two non-equal plumes is given by

$$E(x, z, \psi) = \exp\left(-\left[\frac{x-\chi_1}{b_1}\right]^2\right) + \psi^{\frac{2}{3}} \exp\left(-\left[\frac{x-\chi_2}{b_2}\right]^2\right) \qquad (4.34)$$

where subscripts 1 and 2 refer to the values of these quantities on plumes 1 and 2 respectively. When $\psi = 1$, we return to the equal plume case as expected. We note that (4.34) has an inherent lack of symmetry, as is shown in Figure 4.2, meaning that $\chi_2 \neq -\chi_1$.

The buoyancy profile given in (4.34) may be readily extended to n non-equal

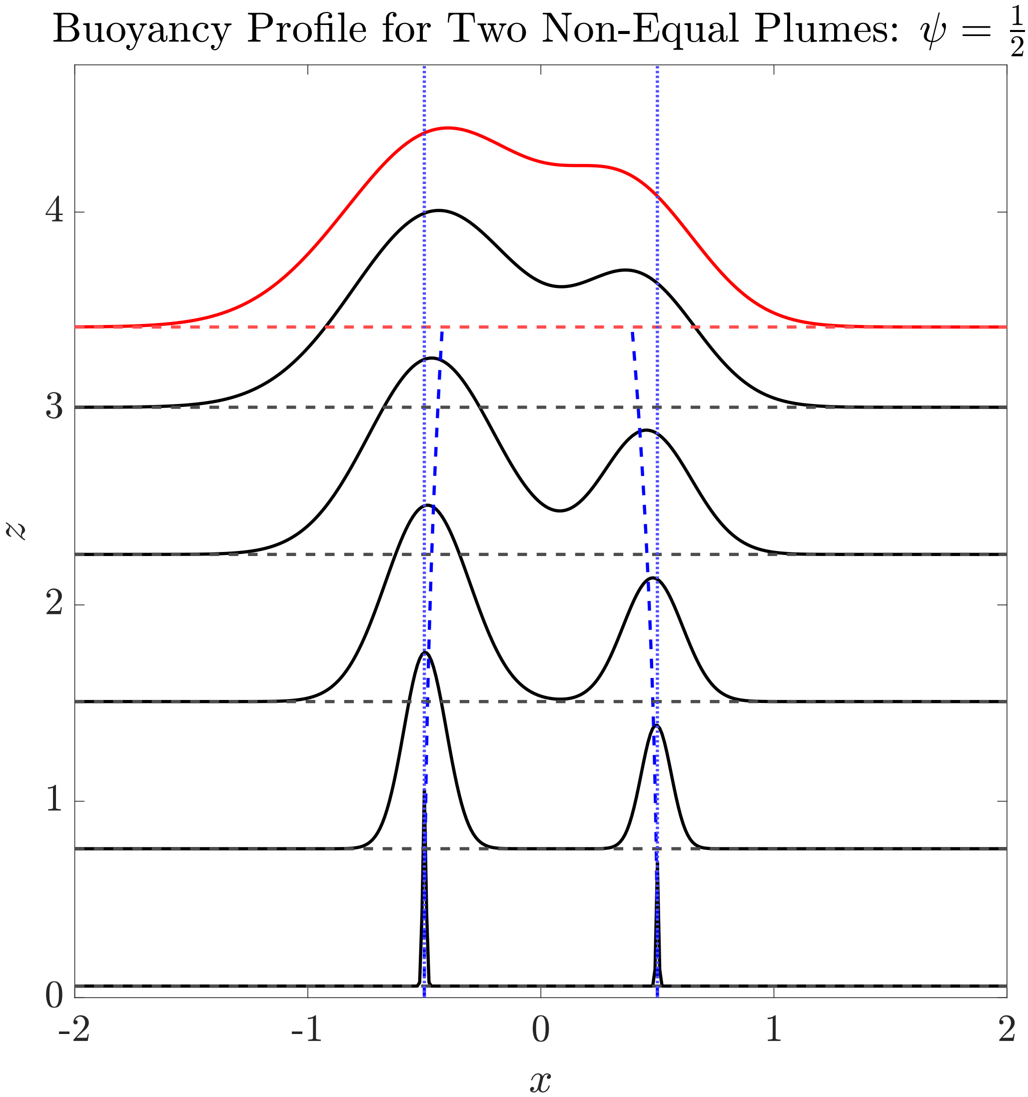

Figure 4.2: Buoyancy profile given by (4.34), with $\psi = \frac{1}{2}$, $\alpha = 0.1$ and $b_1 = \sqrt{2}b_2$. The buoyancy profile at the merging height ($\lambda_m^I = 3.41$) is given in red, and the centreline locations χ_1 and χ_2 are given in blue. The vertical blue lines are $x = \pm\frac{1}{2}\chi_0$, and are to illustrate the asymmetry of χ_1 and χ_2.

plumes, where k of these plumes have specific buoyancy flux F_1, and $n-k$ have specific buoyancy flux F_2, where $\frac{F_2}{F_1} = \psi \leq 1$. This more general buoyancy profile is given by

$$E(x,z,\psi) = \sum_{j=1}^{k/2} \exp\left(-\left[\frac{x-\chi_j}{b_1}\right]^2\right) + \psi^{\frac{2}{3}} \sum_{j=\frac{k}{2}+1}^{n+1-\frac{k}{2}} \exp\left(-\left[\frac{x-\chi_j}{b_2}\right]^2\right) + \sum_{j=n+2-\frac{k}{2}}^{n} \exp\left(-\left[\frac{x-\chi_j}{b_1}\right]^2\right) \tag{4.35}$$

where $b_1 = \sqrt{\frac{1}{\psi}} b_2$. Note that the first sum corresponds to the merged plumes on the left side of the line of plumes, the third corresponds to the merged plumes on the right, and the second to the "unmerged" central plumes. Taking $k=2$, we return to the case discussed above (provided that n is odd). An example will be given for $n=5$, and we note that the details may be extended to an arbitrary odd number of plumes.

To compute the merging height for $n=5$, we begin with five equal plumes. Labelling the centrelines of these plumes $\chi_1, \chi_2, \ldots, \chi_5$ where $\chi_3 = 0$, $\chi_4 = -\chi_2$ and $\chi_5 = -\chi_1$ by symmetry. First, we consider the change in the centreline of the first plume. Using (4.30) and (4.31) with $k=2$, we see that

$$\frac{\mathrm{d}\chi_1}{\mathrm{d}z} = b\alpha \left[\frac{1}{\chi_5 - \chi_1} + \frac{1}{\chi_4 - \chi_1} + \frac{1}{\chi_3 - \chi_1} + \frac{1}{\chi_2 - \chi_1}\right]. \tag{4.36}$$

By applying the symmetry conditions: $\chi_3 = 0, \chi_4 = -\chi_2$ and $\chi_5 = -\chi_1$, (4.36) reduces to

$$\frac{\mathrm{d}\chi_1}{\mathrm{d}z} = b\alpha \left[\frac{1}{-\chi_1 - \chi_1} + \frac{1}{-\chi_2 - \chi_1} + \frac{1}{-\chi_1} + \frac{1}{\chi_2 - \chi_1}\right] \tag{4.37}$$

$$= b\alpha \left[-\frac{3}{2\chi_1} - \frac{1}{\chi_2 + \chi_1} + \frac{1}{\chi_2 - \chi_1}\right] \tag{4.38}$$

subject to $\chi_1(0) = -2\chi_0$. Similarly, for the second plume, we see that

$$\frac{\mathrm{d}\chi_2}{\mathrm{d}z} = b\alpha\left[\frac{1}{\chi_5-\chi_2}+\frac{1}{\chi_4-\chi_2}+\frac{1}{\chi_3-\chi_2}+\frac{1}{\chi_1-\chi_2}\right] \tag{4.39}$$

$$= b\alpha\left[\frac{1}{-\chi_1-\chi_2}+\frac{1}{-\chi_2-\chi_2}+\frac{1}{-\chi_2}+\frac{1}{\chi_1-\chi_2}\right] \tag{4.40}$$

$$= b\alpha\left[-\frac{3}{2\chi_2}-\frac{1}{\chi_2+\chi_1}-\frac{1}{\chi_2-\chi_1}\right] \tag{4.41}$$

subject to $\chi_2(0) = -\chi_0$. With five plumes, the system of equations describing the location of the centrelines, χ_j for $j = 1, 2, \dots 5$ are given by

$$\frac{\mathrm{d}\chi_1}{\mathrm{d}z} = b\alpha\left[-\frac{3}{2\chi_1}-\frac{1}{\chi_2+\chi_1}+\frac{1}{\chi_2-\chi_1}\right] \tag{4.42}$$

$$\frac{\mathrm{d}\chi_2}{\mathrm{d}z} = b\alpha\left[-\frac{3}{2\chi_2}-\frac{1}{\chi_2+\chi_1}-\frac{1}{\chi_2-\chi_1}\right] \tag{4.43}$$

$$\chi_3 = 0 \tag{4.44}$$

$$\chi_4 = -\chi_2 \tag{4.45}$$

$$\chi_5 = -\chi_1 \tag{4.46}$$

subject to $\chi_k(0) = -\frac{n-(2k-1)}{2}\chi_0$. This system of equations is solved using a forward Euler spatial stepping, and the buoyancy profile

$$E(x,z) = \sum_{j=1}^{5} \exp\left(-\left[\frac{x-\chi_j}{b}\right]^2\right) \tag{4.47}$$

computed until (4.47) has three peaks, instead of five. Suppose that this first occurs at $z = z_1$. We now have three plumes of non-equal strength which we label 1, 2, 3 and their centrelines $\bar{\chi_1}, \bar{\chi_2}, \bar{\chi_3}$ respectively. As plume 1 now contains two of the initial plumes (the previous plumes 1 and 2), and similarly plume 3, these new plumes have twice the buoyancy flux of the new plume 2. The ODE describing the location of $\bar{\chi_1}$ is given by

$$\frac{\mathrm{d}\bar{\chi_1}}{\mathrm{d}z} = \frac{b_3\alpha}{\bar{\chi_3} - \bar{\chi_1}} + \frac{b_2\alpha}{\bar{\chi_2} - \bar{\chi_1}} \tag{4.48}$$

$$= \frac{b_1\alpha}{-2\bar{\chi_1}} + \frac{b_2\alpha}{-\bar{\chi_1}} \tag{4.49}$$

subject to $\bar{\chi_1}(z_1) = \frac{1}{2}\left(\chi_1 + \chi_2\right)|_{z=z1}$ and $b_1 = \sqrt{2}b_2$. We also apply $\bar{\chi_2} = 0$ and $\bar{\chi_3} = -\bar{\chi_1}$. For this intermediate line of plumes, the buoyancy profile is given by

$$E(x,z) = \exp\left(-\left[\frac{x-\bar{\chi_1}}{b_1}\right]^2\right) + \left(\frac{1}{2}\right)^{\frac{2}{3}} \exp\left(-\left[\frac{x}{b_2}\right]^2\right) + \exp\left(-\left[\frac{x-\bar{\chi_3}}{b_1}\right]^2\right). \tag{4.50}$$

Iteratively solving for $\bar{\chi_1}$, applying the symmetry conditions for $\bar{\chi_2}$ and $\bar{\chi_3}$, we determine (4.50) for each z. The merging height of the line of five plumes is then given by the first height z for which (4.50) has a single peak. This single peak is found using MATLAB peak detection. We find that, for $n = 5$, the merging height is given by $\lambda_m^I\alpha = 0.55$. Taking $\alpha = 0.1$ and $\chi_0 = 1$, we produce Figure 4.3.

4.3.3 An Interacting Line of An Even Number of Plumes

The interacting case for a line of an even number of plumes is also configured such that the line of plumes is centred about $x = 0$. This is done by centring the plumes at

$$(x,z) = \left(-\frac{n-1}{2}\chi_0, 0\right), \ldots, \left(-\frac{n-(2k-1)}{2}\chi_0, 0\right), \ldots, \left(\frac{n-1}{2}\chi_0, 0\right).$$

Therefore, we model this as line sinks placed at

$$x = \chi_1, \ldots, \chi_k, \ldots, \chi_n.$$

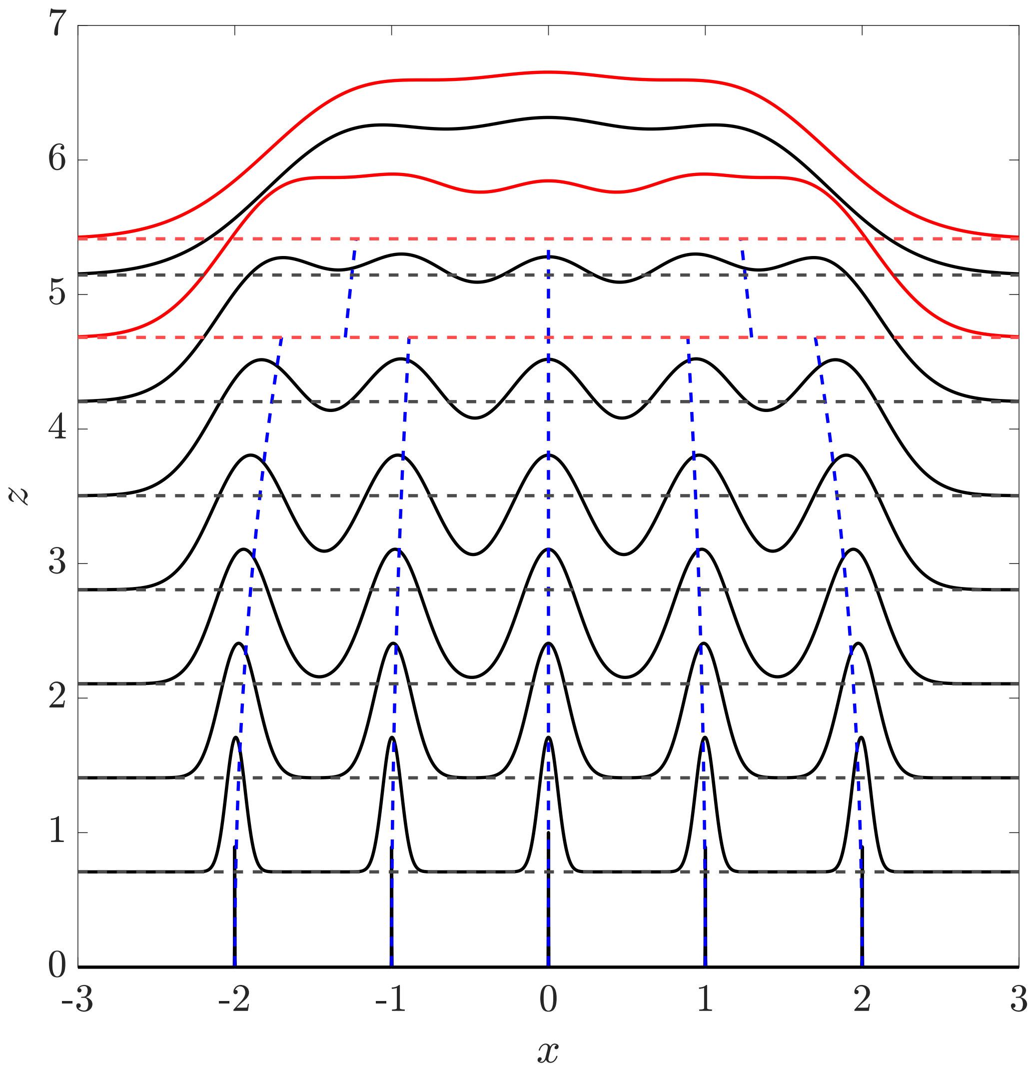

Figure 4.3: Plot of the buoyancy profiles computed for the merging of five equal strength plumes. The centrelines are given in blue, buoyancy profiles in black and the buoyancy profiles at the height of five peaks merging to three, and three to one are given in red.

However, we note that this configuration does not have a plume source located at $x = 0$. That is, the midpoint of the configuration is not necessarily a maximum, and won't be until the line of plumes has merged. Instead of the intial system of equations given by (4.31) - (4.33), the initial system is given by

$$\frac{\mathrm{d}\chi_k}{\mathrm{d}z} = \frac{F_k}{w} \quad \text{for } 1 \leq k \leq \frac{n}{2} \tag{4.51}$$

$$\chi_k = -\chi_{n-k+1} \quad \text{for } \frac{n}{2} + 1 \leq k \leq n \tag{4.52}$$

where F_k is given by (4.29). From here, the method is identical to the odd case. Computing this model for $n = 2, 3, \ldots, 15$, we tabulate the merging heights of the line of n equal strength plumes, which are given in Table 4.1. The behaviour of four interacting co-linear plumes is given in Figure 4.4, using $\alpha = 0.1$, and $\chi_0 = 1$.

The merging heights for up to 15 plumes using the non-interacting model derived in §3 as well as the aforementioned co-linear plumes are given in Figure 4.5.

4.4 Arrays of Interacting Plumes

As in §3, we extend the model of a line of interacting plumes to account for an array of plumes. We consider two specific cases: an equilateral triangle and a 2×2 square grid. As before, we assume that the entrainment of one plume on another is given by (4.7), where r' is the distance between the plumes. As the arrays are two-dimensional, r' is the Euclidean distance between the interacting plumes.

Number of plumes	$\alpha\lambda_m^I$
2	0.435
3	0.454
4	0.558
5	0.588
6	0.612
7	0.720
8	0.764
9	0.818
10	0.973
11	1.074
12	1.116
13	1.116
14	1.193
15	1.203

Table 4.1: Non-dimensional interacting merging heights for up to 15 plumes.

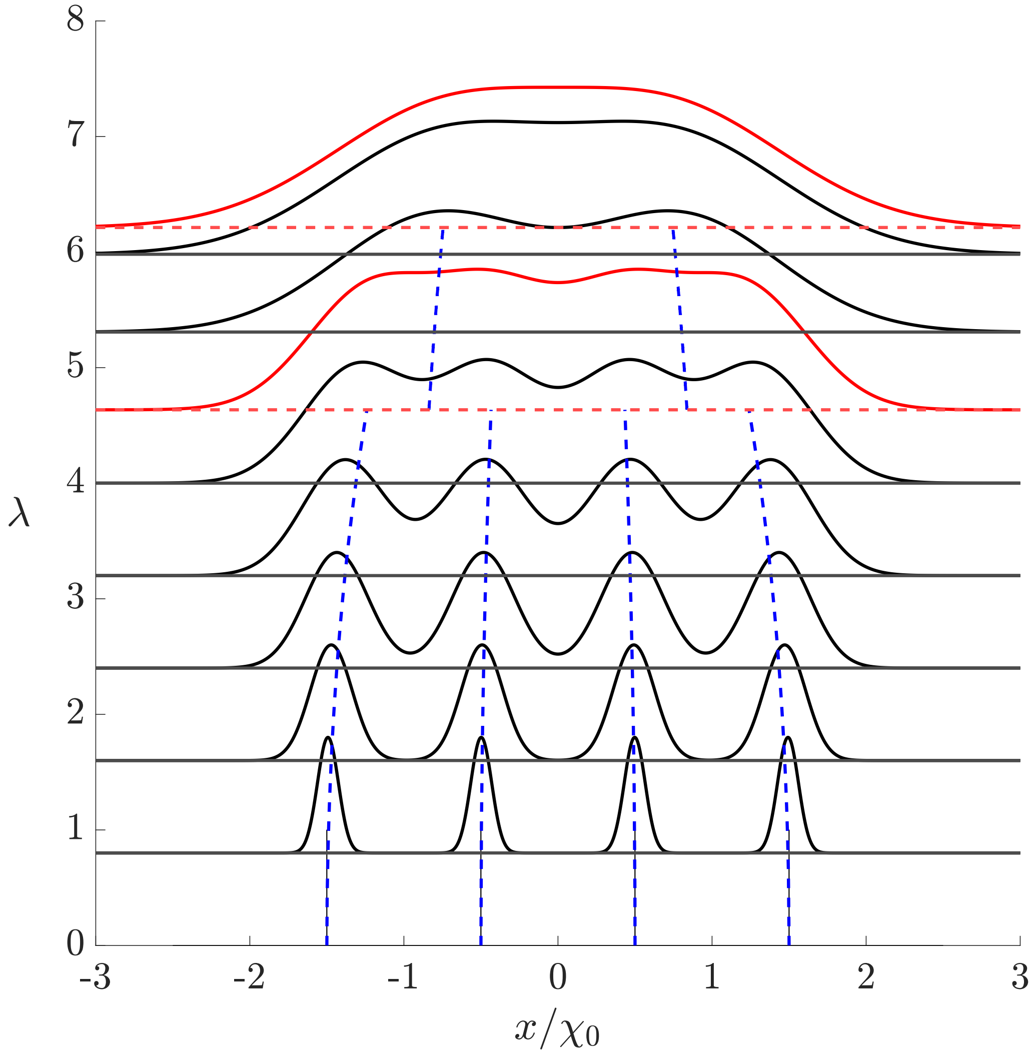

Figure 4.4: plot of the buoyancy profiles computed for the merging of four equal strength plumes. The centrelines are given in blue, buoyancy profiles in black, and the profiles at the height where four peaks merges into two, and two to one are given in red.

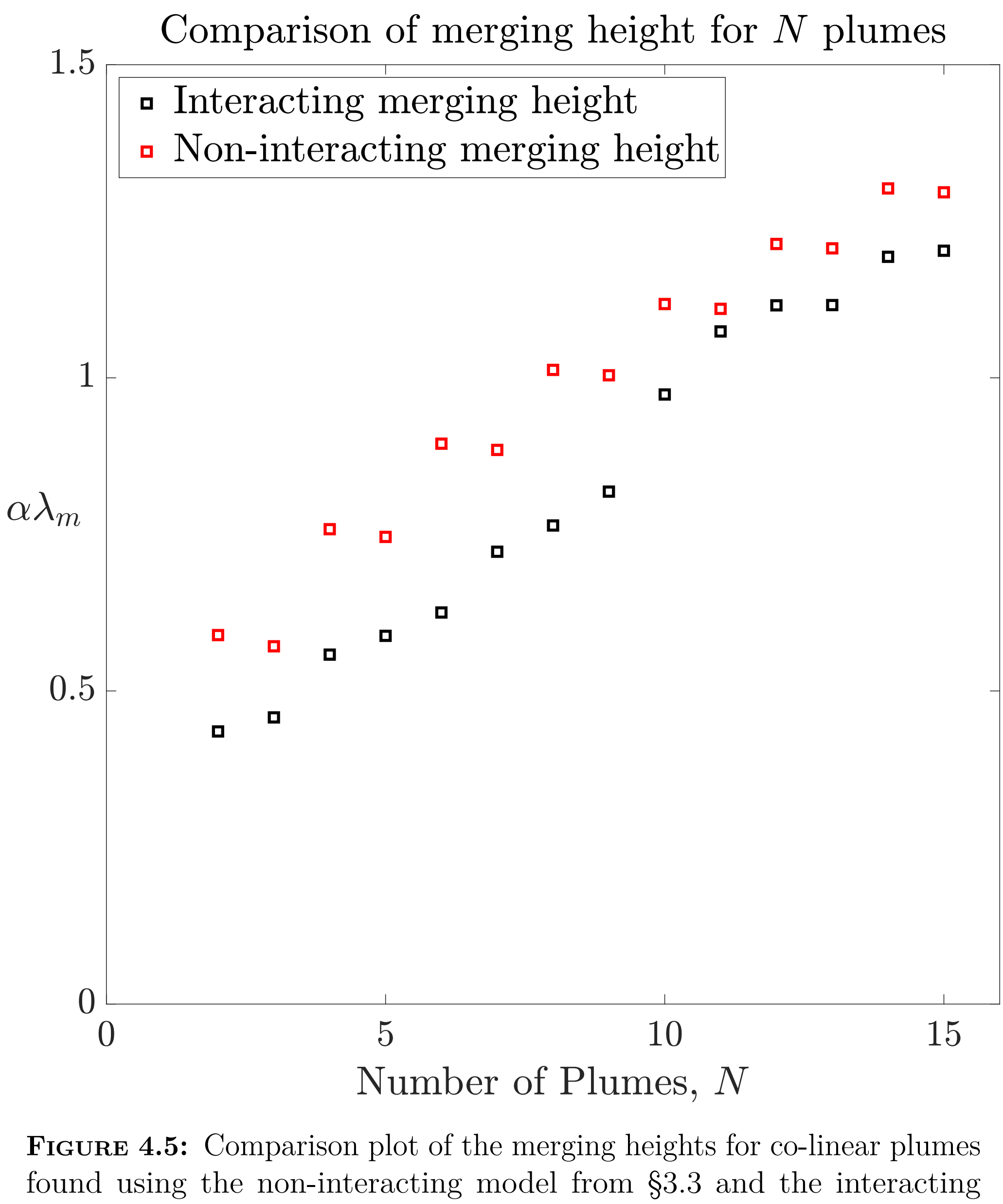

FIGURE 4.5: Comparison plot of the merging heights for co-linear plumes found using the non-interacting model from §3.3 and the interacting model derived in §4.3.

4.4.1 An Equilateral Triangle of Interacting Plumes

We consider an equilateral triangle of interacting plumes where each plume has the same strength. This configuration is given in Figure 4.6. From this schematic, we see that each plume is entrained by two others. We extend the method outlined in §4.3 as follows: denote the location of the centreline of the k^{th} plume by $\boldsymbol{\chi}_k = (\chi_{k,i}, \chi_{k,j})$. We then assume that the merging in each direction is independent, i.e. that the merging in the x direction is independent of that in the y. We then formulate ODEs for each component of each centreline as outlined in section §4.3.2.

Consider a triangular array with sources located at $\left(-\frac{1}{2}\chi_0, 0\right)$, $\left(\frac{1}{2}\chi_0, 0\right)$ and $\left(0, \frac{\sqrt{3}}{2}\chi_0\right)$. Labelling the plumes located at the above positions as $\boldsymbol{\chi}_1$, $\boldsymbol{\chi}_2$ and $\boldsymbol{\chi}_3$ respectively, we generate the following system of equations

$$\frac{\mathrm{d}}{\mathrm{d}z}\left(\chi_{1,i}\right) = b\alpha\left[\frac{1}{\chi_{3,i}-\chi_{1,i}} + \frac{1}{\chi_{2,i}-\chi_{1,i}}\right] \tag{4.53}$$

$$\frac{\mathrm{d}}{\mathrm{d}z}\left(\chi_{1,j}\right) = b\alpha\left[\frac{1}{\chi_{3,j}-\chi_{1,j}}\right] \tag{4.54}$$

$$\chi_{2,i} = -\chi_{1,i} \quad \text{due to symmetry about } x=0 \tag{4.55}$$

$$\chi_{2,j} = \chi_{1,j} \quad \text{as these centrelines are in the same vertical plane} \tag{4.56}$$

$$\chi_{3,i} = 0 \quad \text{by symmetry about } x=0 \tag{4.57}$$

$$\frac{\mathrm{d}}{\mathrm{d}z}\left(\chi_{3,j}\right) = b\alpha\left[\frac{2}{\chi_{1,j}-\chi_{3,j}}\right] \tag{4.58}$$

subject to $\left(\chi_{1,i}, \chi_{1,j}\right)|_{z=0} = \left(-\frac{1}{2}\chi_0, 0\right)$, $\left(\chi_{2,i}, \chi_{2,j}\right)|_{z=0} = \left(\frac{1}{2}\chi_0, 0\right)$ and $\left(\chi_{3,i}, \chi_{3,j}\right)|_{z=0} = \left(0, \frac{\sqrt{3}}{2}\chi_0\right)$. This is given in Figure 4.6.

By solving the above system of equations, we capture the behaviour of each centreline in both x and y directions. We then define a buoyancy function, extended to an additional spatial dimension, given by

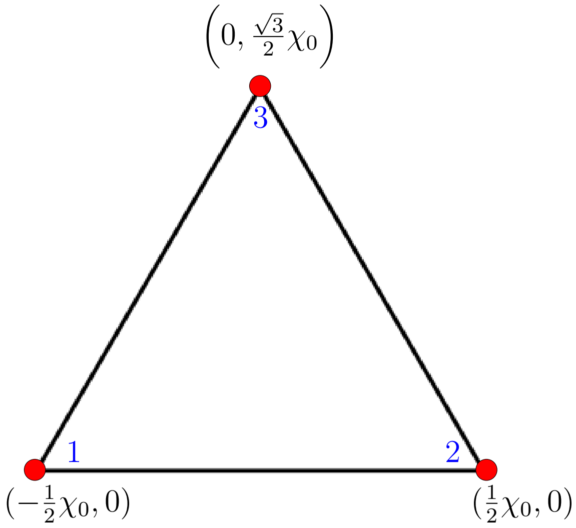

Figure 4.6: Schematic of the equilateral triangular plume configuration.

$$E(x, y, z) = \sum_{k=1}^{3} \exp\left(-\left[\frac{(x-\chi_{k,i})^2 + (y-\chi_{k,j})^2}{b(z)^2}\right]\right). \tag{4.59}$$

As in section §4.3.2, we seek the first height at which equation has a single peak. For a 2D array, the surface given by (4.59) is plotted, and the number of peaks of this surface are determined using MATLAB peak detection. (4.59) is plotted iteratively until the first height of a single peak is determined. This is the merging height, λ_m^I, of the triangular array of plumes and is found to be $\lambda_m^I = \frac{0.318}{\alpha}$.

4.4.2 A 2 × 2 Grid of Interacting Plumes

Finally, we consider a 2×2 grid of plumes, where the sides of the grid are χ_0 and therefore the diagonal distance between corners is $\sqrt{2}\chi_0$. Labelling the corners of the square, starting in the bottom left, anti-clockwise as 1,2,3 and 4, the plume sources are given by $\left(\chi_{1,i}, \chi_{1,j}\right)|_{z=0} = \left(-\frac{1}{2}\chi_0, -\frac{1}{2}\chi_0\right)$, $\left(\chi_{2,i}, \chi_{2,j}\right)|_{z=0} = \left(\frac{1}{2}\chi_0, -\frac{1}{2}\chi_0\right)$, $\left(\chi_{3,i}, \chi_{3,j}\right)|_{z=0} = \left(\frac{1}{2}\chi_0, \frac{1}{2}\chi_0\right)$ and $\left(\chi_{4,i}, \chi_{4,j}\right)|_{z=0} = \left(-\frac{1}{2}\chi_0, \frac{1}{2}\chi_0\right)$.

As in section §4.4.1, we formulate a system of equations to describe the centrelines of the plumes in this grid, given by

$$\frac{\mathrm{d}}{\mathrm{d}z}\left(\chi_{1,i}\right) = b\alpha\left[\frac{1}{\chi_{3,i}-\chi_{1,i}} + \frac{1}{\chi_{2,i}-\chi_{1,i}}\right] \tag{4.60}$$

$$\frac{\mathrm{d}}{\mathrm{d}z}\left(\chi_{1,j}\right) = b\alpha\left[\frac{1}{\chi_{4,j}-\chi_{1,j}} + \frac{1}{\chi_{3,j}-\chi_{1,j}}\right] \tag{4.61}$$

$$\chi_{2,i} = -\chi_{1,i} \tag{4.62}$$

$$\chi_{2,j} = \chi_{1,j} \tag{4.63}$$

$$\chi_{3,i} = \chi_{2,i} \tag{4.64}$$

$$\chi_{3,j} = -\chi_{1,j} \tag{4.65}$$

$$\chi_{4,i} = \chi_{1,i} \tag{4.66}$$

$$\chi_{4,j} = \chi_{3,j} \tag{4.67}$$

subject to the above initial conditions, shown in Figure 4.7. The buoyancy

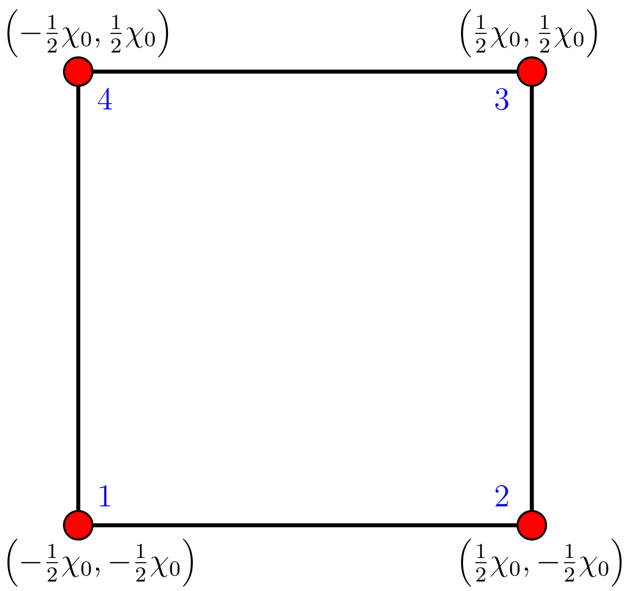

FIGURE 4.7: Schematic of the 2×2 array of plumes.

profile is then given by

$$E(x, y, z) = \sum_{k=1}^{4} \exp\left(-\left[\frac{(x-\chi_{k,i})^2 + (y-\chi_{k,j})^2}{b(z)^2}\right]\right). \tag{4.68}$$

By determining the first height at which equation has a single peak, we find the merging height $\lambda_m^I = \frac{0.361}{\alpha}$.

4.5 Experimental Data

The modelling work of §3 and §4 aimed to find a non-dimensional height at which a line, or array, of plumes will behave as as single, larger plume. This height is defined as the merging height or height of coalescence. We experimentally find this merging height, and compare to the values predicted by the interacting and non-interacting models in §3.3 and §4.3. The notation of KL04 is used to allow for direct comparison. We denote the experimental merging height by z_{me}, and the corresponding experimental, non-dimensional merging height by λ_{me}. Recall also that the non-dimensional merging heights from the non-interacting and interacting models are given by λ_m^{NI} and λ_m^I respectively.

4.5.1 Experimental Set Up

Experiments were performed in a perspex tank with dimenions 750 mm $\times$ 650 mm $\times$ 650 mm. This tank was filled with freshwater of density $\rho = 1000\,\mathrm{kg\,m^{-3}}$, which was measured by a sodium chloride refractometer. The plumes were created using a saline solution of density $\rho = 1033\,\mathrm{kg\,m^{-3}}$, again measured with a sodium chloride refractometer. This solution was created using 20 litres of freshwater mixed thoroughly with 1.03 kg of sodium chloride. The plumes were visualised using 3 grams of E151 brilliant black dye and 0.3 grams of yellow tartrazine dye.

The footage was collected at 30 frames per second using a camera with a 25 mm lens. To ensure constant lighting, a uniform intensity light sheet was placed behind the perspex tank. All other light sources were removed from the laboratory. This was done to remove "noise" from the data. The experimental set up is given schematically in Figure 4.8.

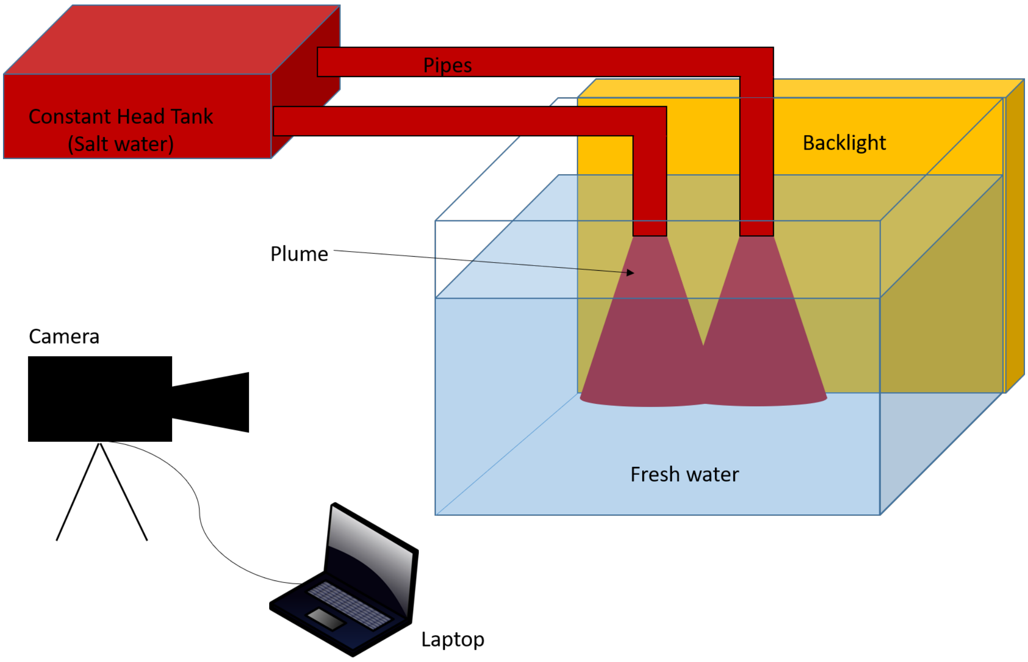

Figure 4.8: Schematic of the experimental set up used for the merging plumes in a stationary environment experiments.

To ensure that the plumes created were fully turbulent, a set of four custom plume nozzles were created following the design by Dr Paul Cooper, Department of Mechanical Engineering, University of Wollongong, NSW, Australia shown in Figure 4.9.

Due to the number of plume nozzles available, we performed experiments with a single plume and lines of two, three and four plumes. Each of these plumes has the same strength, and all lines of plumes are configured such that each plume is separated by the same distance from its nearest neighbour.

4.5.2 Experimental Technique

Single plume experiments were performed to determine the entrainment coefficient of each nozzle. We then performed experiments focused on merging heights. The method for these experiments is given as follows:

1. Set the nozzle separation (skip this step for an experiment using only

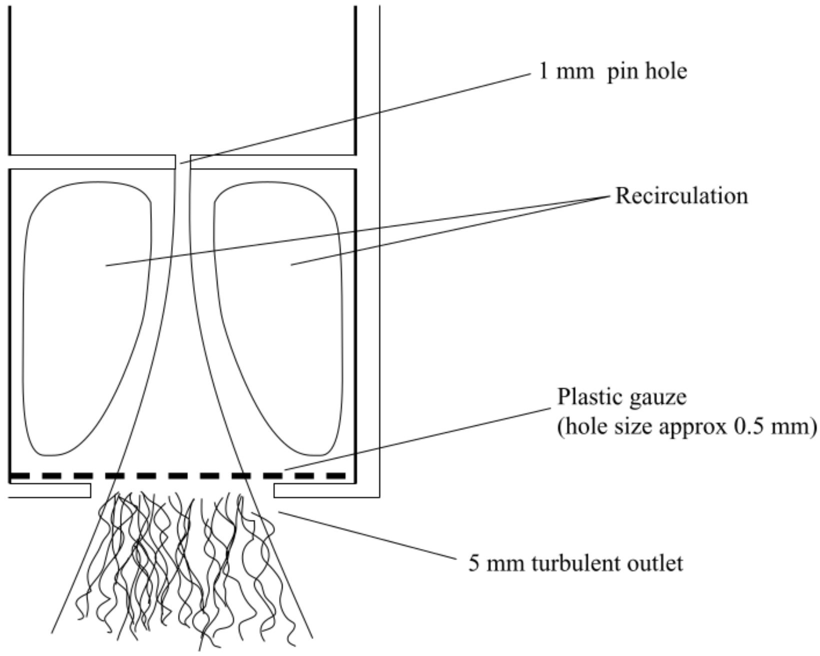

Figure 4.9: Design of the nozzle used to create a turbulent plume. This is Figure 10 of KL04.

one nozzle).

2. Fill the perspex tank to 700 mm with freshwater. Ensure that the tank has no internal flow before continuing. This is achieved, based on preliminary experimentation, by waiting approximately 45 minutes between the end of filling and the start of the experiment.

3. By very carefully running a long thin sponge along the front glass panel, so as not to introduce an internal flow, remove any bubbles from the front of the perspex tank. If currents were present, the experimental was delayed until they ceased.

4. Record 300 frames of background footage. This was used later to remove background noise from plume imagery (explained later in §4.5.4).

5. Turn on all nozzles being used and allow to run for 30 seconds. This allows the plume(s) to establish.

6. Begin recording the experiment. Record for 45 seconds.

7. Stop recording, turn off nozzles and drain the water from the perspex tank.

8. Increase the nozzle separation by 5 mm. Repeat method until the configuration no longer merges before reaching the bottom of the tank.

4.5.3 The Entrainment Coefficient

To compare experimental data to predictions from the modelling in §3.3 - §4.3, we must find the entrainment coefficient. Recall that the derivation of the plume ODE model (1.1) - (1.3) assumes that the velocity of entrained fluid is proportional to the mean centreline vertical velocity inside the plume at the same height. That is, $u_e \propto w$. The constant of proportionality is the entrainment coefficient, denoted α. For a steady plume, we may determine α by measuring the plume radius, b. Recall that $b = \frac{6\alpha}{5}z$. Therefore, by computing the plume radius of a single plume from the experimental footage, we may determine α. Doing so, we found that the average entrainment coefficient of plumes generated from each nozzle is $\alpha = 0.086$. Importantly, this is close to the value used by Lai [71] ($\alpha = 0.085$) and slightly lower than the value used in KL04 ($\alpha = 0.09$). The experiments were performed using a nozzle radius (b_0) of 2.5 mm, an initial velocity (w_0) of $0.088\,\mathrm{m\,s^{-1}}$ and a modified gravity (g_0') of $0.392\,\mathrm{m\,s^{-2}}$. This resulted in a source Froude number $\Gamma_0 = 0.921$ (i.e. a forced plume) and therefore a virtual origin correction of 2.10 cm was used in the experiments in this chapter. The source Froude number was computed using (3.28), and the virtual origin correction was found using the method given in §3.4.3.

4.5.4 Processing Experimental Data

The footage captured in these plume experiments must be processed to determine the merging height. We first performed the dye attenuation technique, outlined in [68], in Digiflow (documentation found at `http://www.dampt.cam.ac.uk/lab/digiflow/`). The background image is subtracted from each frame of the recorded footage. We then time-average these frames to give the processed, time-averaged, plume configuration behaviour in a single image. An example of this technique is given in Figure 4.10. This is done because the modelling in §3 and §4 only considers steady plumes. An example of instantaneous behaviour is given in Figure 4.11, and the time-averaged behaviour is given in Figure 4.12.

The merging height may be determined using the time-averaged image. Recall, from §3.2, that the buoyancy profile of a plume is well approximated by a Gaussian, centred at the midline of the plume. Furthermore, it was shown, by [72], that the buoyancy profile of a line of plumes may be approximated by a superposition of these Gaussians. Using this, we outline finding the merging height of two plumes, and note that it can be extended to an arbitrary line by adding more Gaussians, as shown in (4.70).

For each row of pixels of the time-averaged two-plume image, we fit a function of the form

$$G = \frac{a_1}{a_2\sqrt{2\pi}} \exp\left(-\frac{(x-a_3)^2}{2a_2^2}\right) + \frac{a_4}{a_5\sqrt{2\pi}} \exp\left(-\frac{(x-a_6)^2}{2a_5^2}\right) \tag{4.69}$$

where a_3 and a_6 are the positions of maximum buoyancy, i.e. the centre of each plume. For n plumes, G would take the form

$$G = \sum_{k=1}^{n} \frac{a_{3k-2}}{a_{3k-1}\sqrt{2\pi}} \exp\left(-\frac{(x-a_{3k})^2}{2a_{3k-1}^2}\right). \tag{4.70}$$

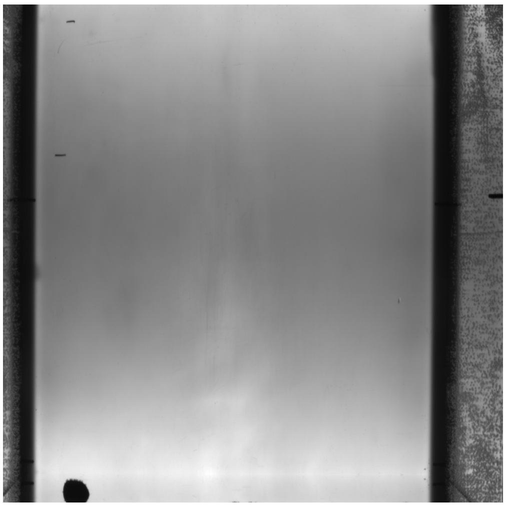

(a) Background image for dye attenuation.

(b) Raw plume image for dye attenuation.

(c) Plume image with background subtracted.

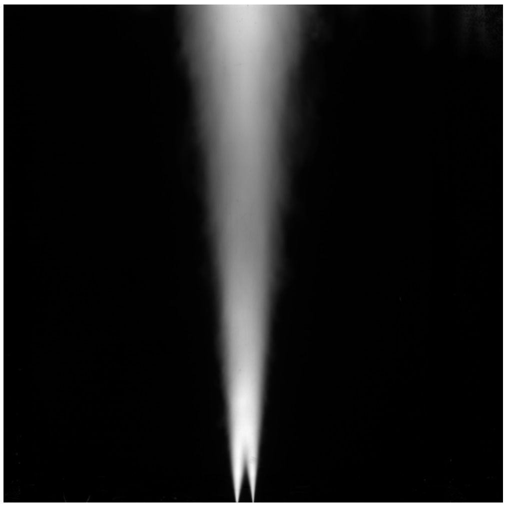

(d) Time-average of all “subtracted” plume images.

FIGURE 4.10: Schematic of the dye attenuation technique. Figure 4.10b - Figure 4.10a gives Figure 4.10c, a so-called “subtracted image”. Time-averaging all subtracted images gives Figure 4.10d.

FIGURE 4.11: An instantaneous snapshot of the behaviour of two, three and four co-linear plumes 21.3 seconds after filming started. The plumes are configured such that each plume is separated from the adjacent plumes by $\chi_0 = 25\,\mathrm{mm}$.

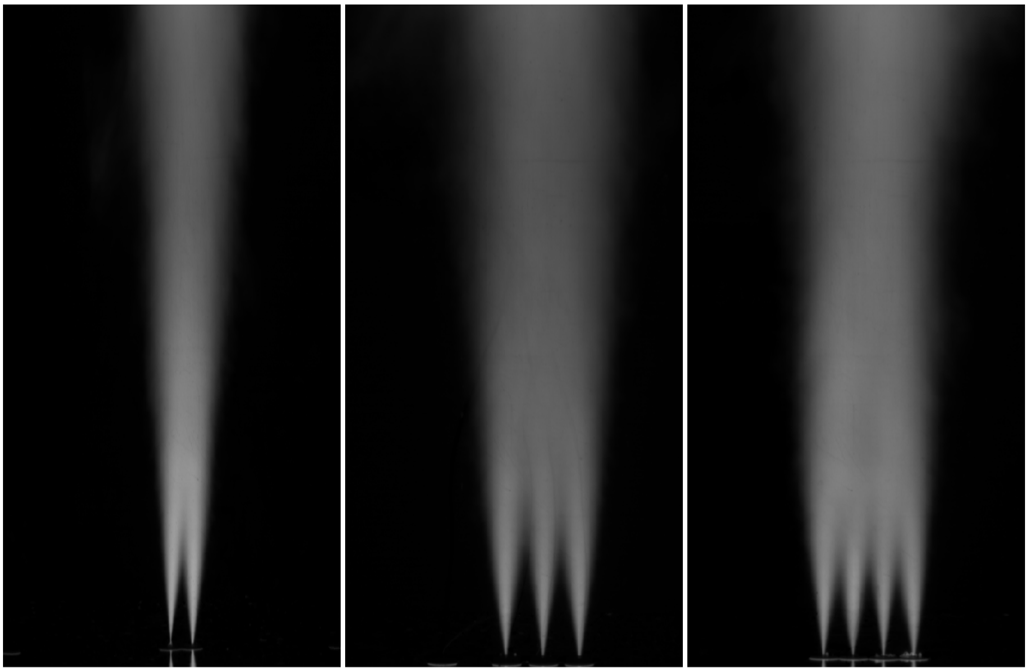

FIGURE 4.12: Time-averaged behaviour of two, three and four co-linear plumes. The plumes are configured such that each plume is separated from the adjacent plumes by χ_0 =25 mm, and the data is formed from the frames of the 45 second video.

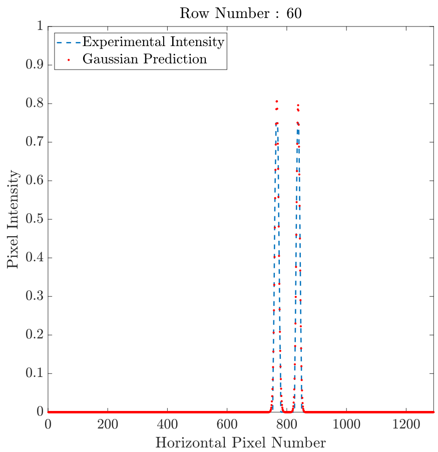

(a) Light intensity profile at the source of the plumes

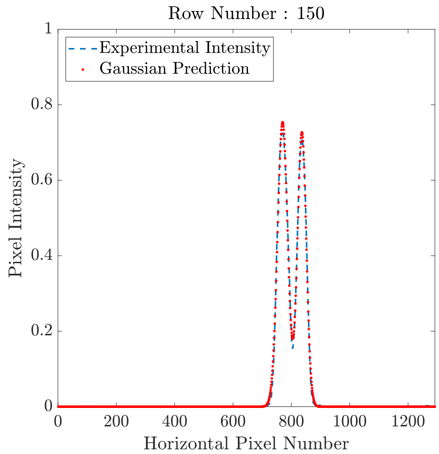

(b) Light intensity profile at 35% of the merging height.

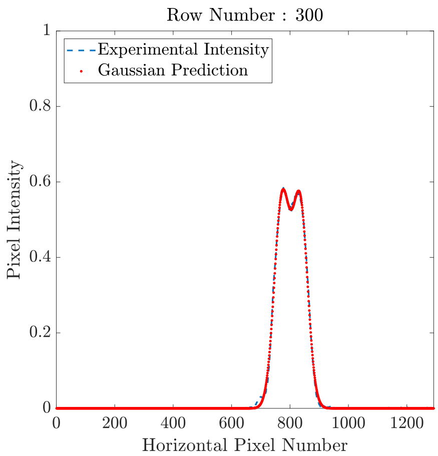

(c) Light intensity profile at 72% of the merging height.

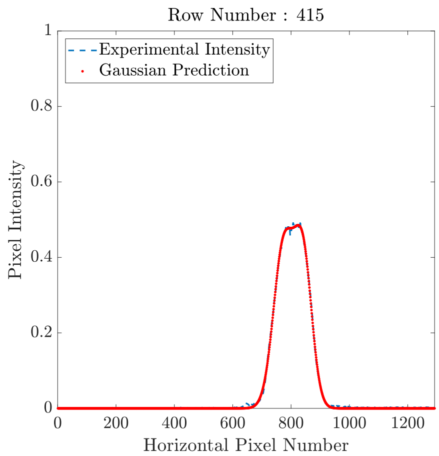

(d) Light intensity profile at the merging height.

FIGURE 4.13: Light intensity data from stillwater experiments for two plumes, separated 43mm, at various distances from the source.

By fitting (4.69) to each row of pixels, we find the two peaked Gaussian that best fits the experimental data. This is repeated for each row of pixels until (4.69) has a single maximum. This gives the vertical pixel at which the plumes have merged. This can then be converted to a real-world distance using the "edit coordinates" function in Digiflow. This converts pixel measurements to real-world measurements, based on known distances, using a least squares mapping. The real-world distance is the merging height of the system.

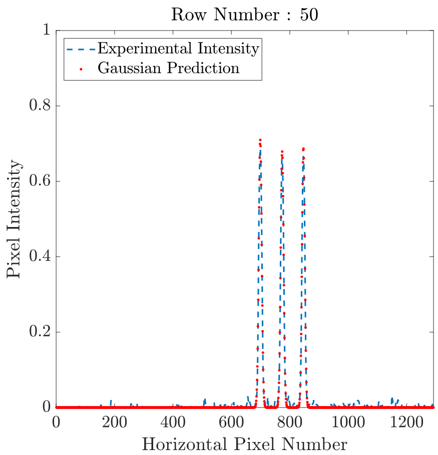

(a) Light intensity profile at the source of the plumes

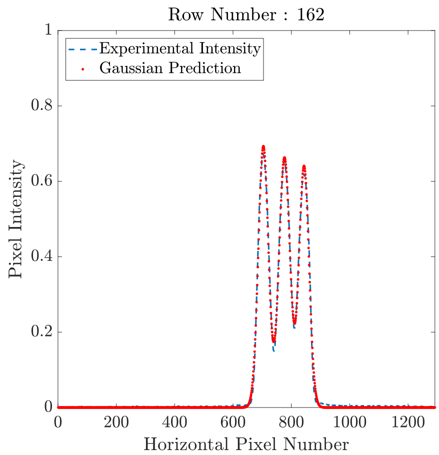

(b) Light intensity profile at 40% of the merging height.

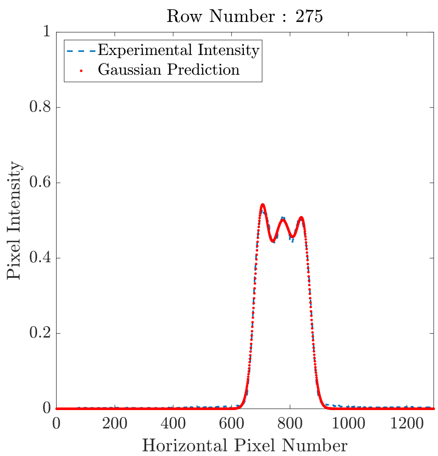

(c) Light intensity profile at 70% of the merging height.

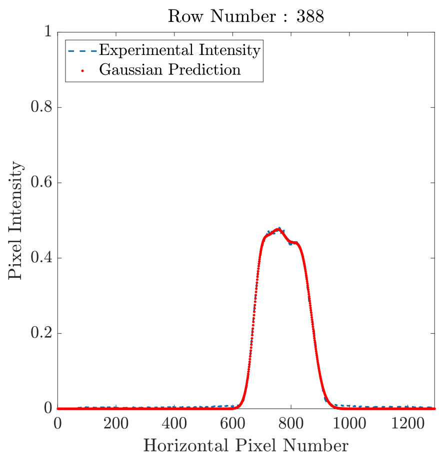

(d) Light intensity profile at the merging height.

FIGURE 4.14: Light intensity data from stillwater experiments for three plumes, separated 43mm, at various distances from the source.

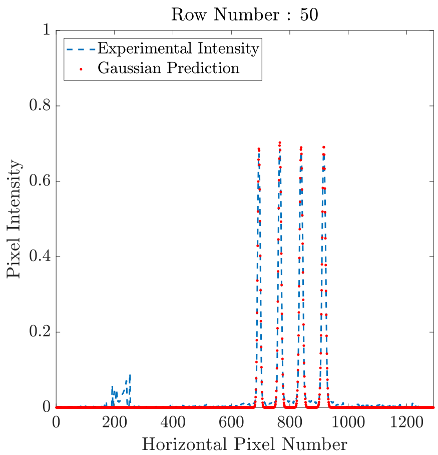

(a) Light intensity profile at the source of the plumes

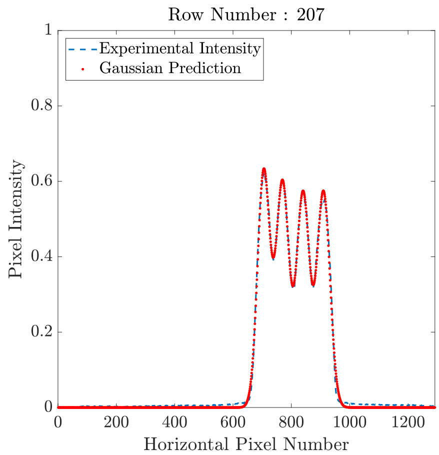

(b) Light intensity profile at 40% of the merging height.

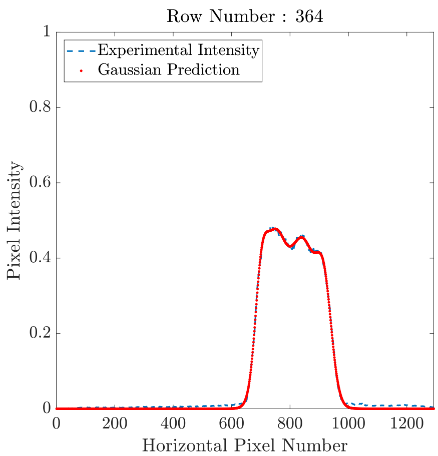

(c) Light intensity profile at 70% of the merging height.

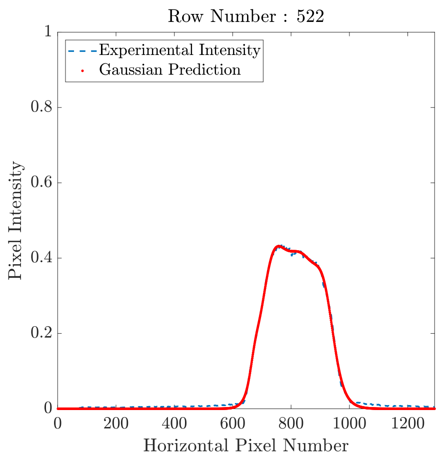

(d) Light intensity profile at the merging height.

FIGURE 4.15: Light intensity data from stillwater experiments for four plumes, separated 43mm, at various distances from the source.

4.6 Results

4.6.1 Extracting λ_{me}

Following the procedure outlined in §4.5.2 and §4.5.4, the merging heights of each plume configuration was determined as shown in Figure 4.13 - Figure 4.15. By fitting a line of the form $z_{\text{me}} = \lambda_{\text{me}}\chi_0$ to the merging heights, we found the non-dimensional merging height for each configuration. The values for each configuration are given in Table 4.2. The merging heights for each configuration, as a function of separation, are plotted in Figure 4.16 - 4.20. The error bars shown in the aforementioned plots are computed by splitting each video into thirds and determining the merging height for each of these thirds. The standard deviation of these merging heights is the magnitude of the error bars. These error bars are given, as a percentage, in table 4.3, in accordance with the following correction for the array imagery data. Furthermore, the magnitude of these error bars falls well within the variation expected from simulating a turbulent system such as this.

Configuration	λ_{me}	λ_m^I
Line of two	5.09	5.08
Line of three	5.32	5.30
Line of four	6.30	6.48
Equilateral triangle	2.01	3.70
2×2 square grid	1.81	4.20

Table 4.2: Non-dimensional merging heights of all experimental configurations and corresponding model merging heights with the uncorrected array data.

Note that the imagery collected for the triangular and 2×2 grid array of plumes was only visualised by one camera, meaning it appeared as three or four co-linear plumes respectively. This led to an experimental merging height significantly lower than expected by the models in §4.4.1 and §4.4.2.

To correct for this, we simulated the array models for each experiment, and obtained the "true" merging height (the merging height of the array) and the "observed" merging height (the merging height obtained from the viewpoint in my experiments). A linear mapping was found between the observed and true merging heights for these arrays. By applying this mapping to the experimental data (and the error bars) for the arrays of plumes, the visualisation error in these experiments was corrected. The experimental data, including the corrected data is shown in Figure 4.19 and Figure 4.20. We see that by using the above correction, the experimental data is now in good agreement with the modelling outlined in §4.4.1 and §4.4.2, as shown in Table 4.3.

Configuration	λ_{me}	λ_m^I
Line of two	5.09 ± 5.57%	5.08
Line of three	5.32 ± 8.03%	5.30
Line of four	6.30 ± 9.86%	6.48
Equilateral triangle	3.69 ± 3.25%	3.70
2×2 square grid	3.89 ± 7.45%	4.20

Table 4.3: Non-dimensional merging heights of all experimental configurations and corresponding model merging heights with the corrected array data.

4.6.2 Discussion & Comparison to Models

We found that the experimental merging height of the two and three plume configurations were very well approximated by the interacting models (4.6) and (4.11). This is shown in Figure 4.16 - Figure 4.17. This strongly supports the modelling of two interacting plumes by Kaye & Linden [38] and the extension derived in §4.3.1. Note that all experimental data plotted in this chapter are non-dimensionalised with respect to the nozzle radius, $b_0 = 2.5\,\mathrm{mm}$.

In each of the three remaining cases, we found that the experimental merging

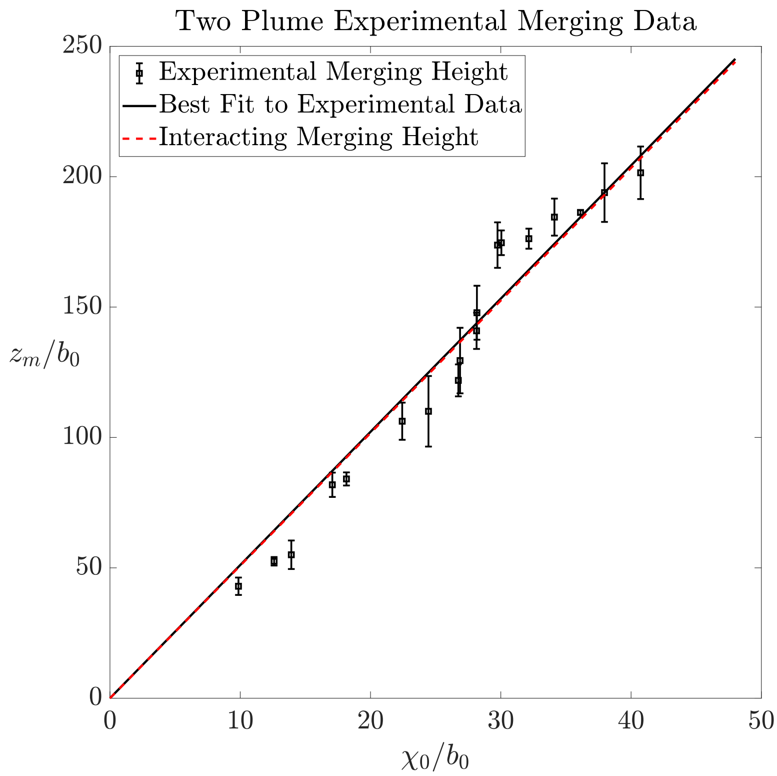

FIGURE 4.16: Experimental data for the merging height of two plumes. This data has a goodness of fit $r^2 = 0.880$ with the straight line through the origin.

height is lower than that predicted by the modelling in §4.3 - §4.4. The experimental data for four co-linear plumes are given in Figure 4.18, and the arrays of plumes are given in Figure 4.19 - Figure 4.20. All merging height data are also plotted on the same axis in Figure 4.21. Note that the data given for the array experiments here are the corrected values, not the original.

We also see that the uncorrected experimental data from the arrays is in poor agreement with the modelling in §4.4.1 and §4.4.2. However, once the correction is made, we see that the data is now in good agreement with the aforementioned models.

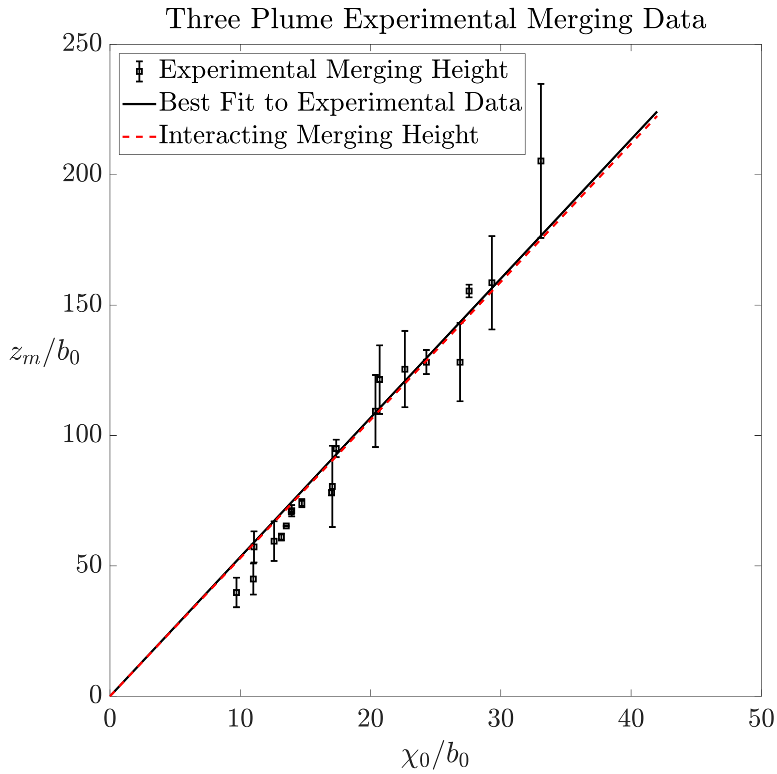

Figure 4.17: Experimental data for the merging height of three co-linear plumes. This data has a goodness of fit $r^2 = 0.895$ with the straight line through the origin.

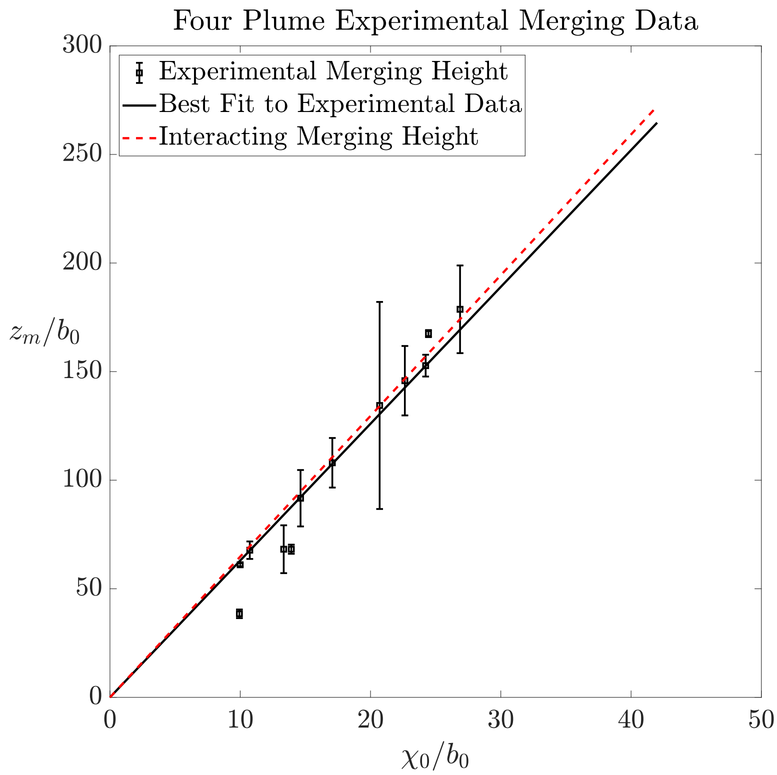

Figure 4.18: Experimental data for the merging height of four co-linear plumes. This data has a goodness of fit $r^2 = 0.937$ with the straight line through the origin.

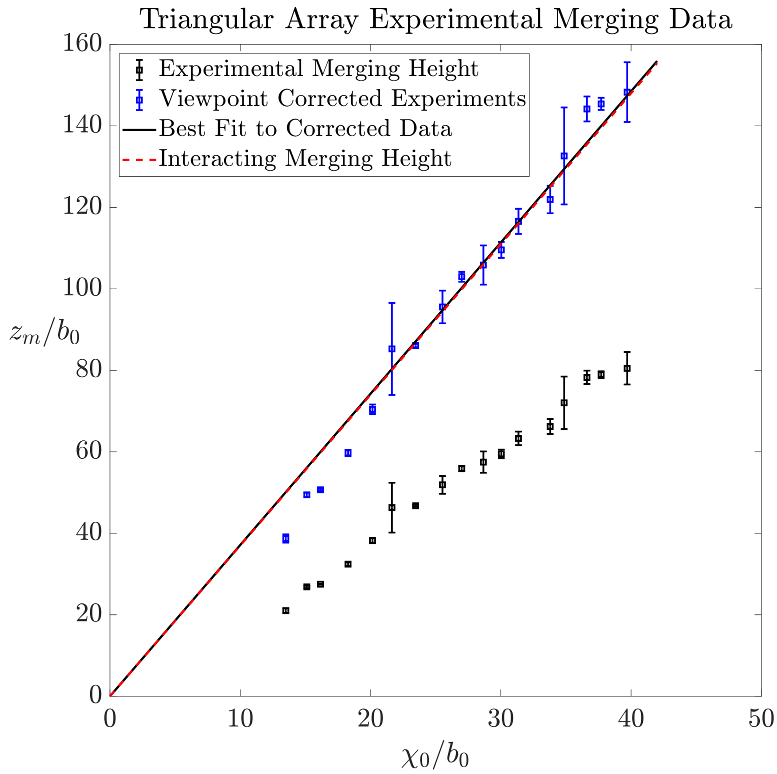

FIGURE 4.19: Experimental data for the merging height of equilateral triangle of plumes. This data has a goodness of fit $r^2 = 0.903$ with the straight line through the origin.

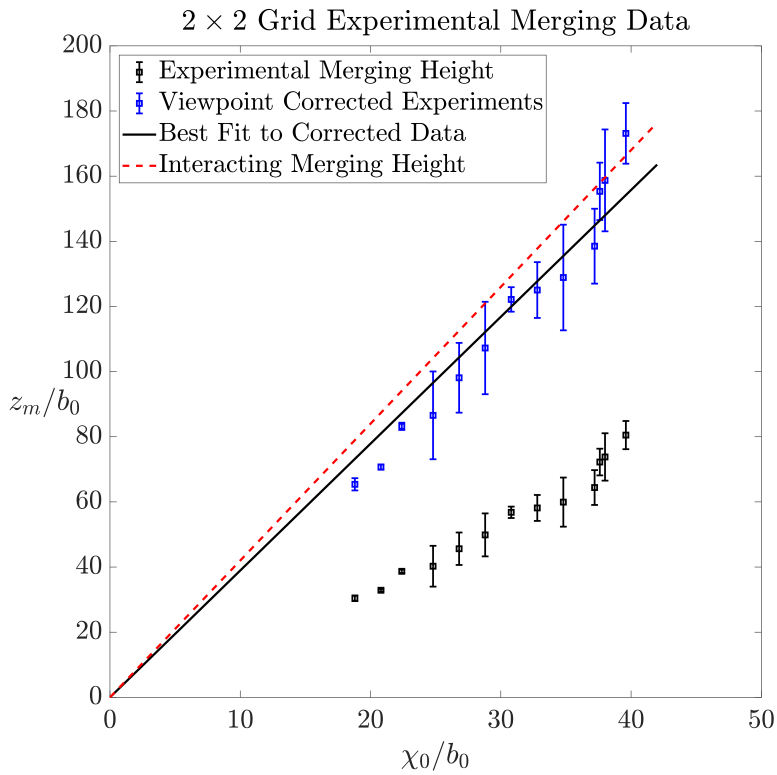

FIGURE 4.20: Experimental data for the merging height of 2×2 grid of plumes. This data has a goodness of fit $r^2 = 0.908$ with the straight line through the origin.

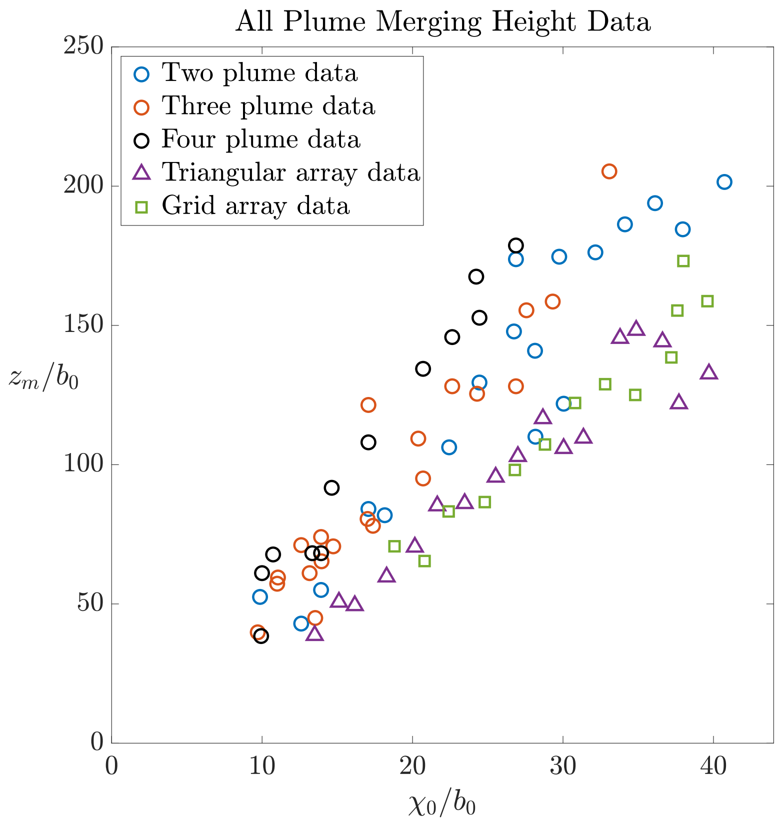

FIGURE 4.21: All plume coalescence merging heights plotted on the same axis.

4.7 Comparison to an Existing Model

A coupled ODE model to describe the dynamic interaction of a system of interacting jets was derived in [71]. A brief introduction of this model is given below. For a detailed derivation of this model, see [71].

Consider a group of buoyant jets with initial velocity u_0, source density ρ_0 discharged into a still ambient with uniform density ρ_a and depth H. Each jet discharges at an inclined vertical angle to the horizontal plane ϕ_0 and horizontal angle θ_0 to the x axis. To compare to the work of this chapter, we take $\phi_0 = \frac{\pi}{2}$ and $\theta_0 = 0$. Each individual jet behaves like a free jet initially, entraining the surrounding fluid and inducing an irrotational flow field. The pressure in the space between the jets tends to draw the jets together, changing their trajectories. This in turn induces a new flow field and pressure field causing a feedback loop. This process continues until a

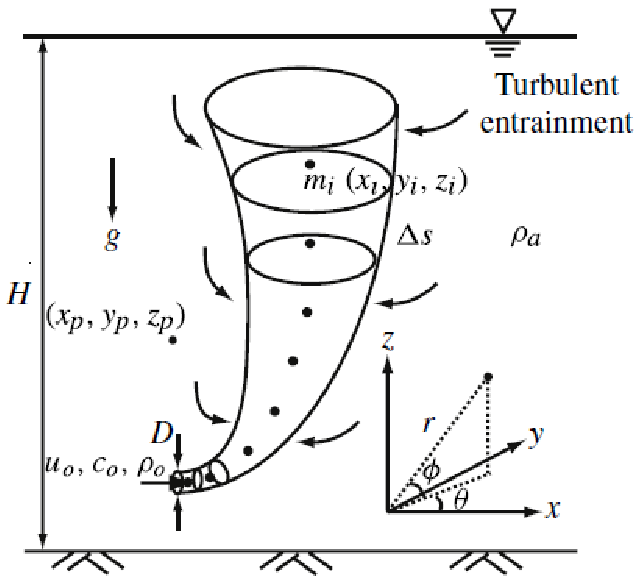

FIGURE 4.22: Schematic of an inclined buoyant jet. This is Figure 1(a) of [71].

steady state is reached.

The irrotational flow field can be modelled by a line sink with prescribed strength [73, 38]. The buoyant jet is considered as a series of jet elements of thickness Δs. Each element may be expressed as a 3D point sink of strength $m_i = -\dfrac{\mathrm{d}Q}{\mathrm{d}s}$, where Q is the specific volume flux of the plume at the i^{th} point sink and s is the curvilinear coordinate defined by (4.82), at a position $\boldsymbol{r}_i = (x_i, y_i, z_i)$. The velocity potential of this jet element is

$$\phi_i = \frac{m_i}{4\pi|\boldsymbol{r} - \boldsymbol{r}_i|}\Delta s, \tag{4.71}$$

where $\boldsymbol{r} = (x, y, z)$. The induced radial velocity at an arbitrary point $\boldsymbol{r}$ is given by the negative gradient of the velocity potential:

$$u_r = \frac{m_i}{4\pi|\boldsymbol{r} - \boldsymbol{r}_i|^2}\Delta s, \tag{4.72}$$

where $|\boldsymbol{r} - \boldsymbol{r}_i|^2 = (x - x_i)^2 + (y - y_i)^2 + (z - z_i)^2$.

For multiple buoyant jet discharges, the N_j jets consist of N point sinks.

For a given point $\boldsymbol{r}_p = (x_p, y_p, z_p)$, the induced velocity due to each point sink is given by

$$(u_x)_{ij} = \frac{m_i}{4\pi}\frac{(x_p - x_{ij})}{|\boldsymbol{r} - \boldsymbol{r}_i|^3}\Delta s, \quad (u_y)_{ij} = \frac{m_i}{4\pi}\frac{(y_p - y_{ij})}{|\boldsymbol{r} - \boldsymbol{r}_i|^3}\Delta s, \quad (u_z)_{ij} = \frac{m_i}{4\pi}\frac{(z_p - z_{ij})}{|\boldsymbol{r} - \boldsymbol{r}_i|^3}\Delta s, \tag{4.73}$$

where $i = 1, ..., N$ and $j = 1, ..., N_j$ are the point sink index and the jet index respectively. The external flow field induced by the jets is the superposition of all external flows induced by all point sinks and is therefore given by

$$u_x = \sum_{j=1}^{N_j}\sum_{i=1}^{N}(u_x)_{ij}, \quad u_y = \sum_{j=1}^{N_j}\sum_{i=1}^{N}(u_y)_{ij}, \quad u_z = \sum_{j=1}^{N_j}\sum_{i=1}^{N}(u_z)_{ij}. \tag{4.74}$$

For the irrotational flow $\boldsymbol{u} = (u_x, u_y, u_z)$ outside of the jets, the pressure is related to velocity by Bernoulli's equation

$$P = -\frac{1}{2}\rho|\boldsymbol{u}|^2 \tag{4.75}$$

where $|\boldsymbol{u}|^2 = u_x^2 + u_y^2 + u_z^2$. Note that in [71], $\boldsymbol{u}$ is denoted $\boldsymbol{q}$.

4.7.1 The Coupled System for Dynamic Pressure

Consider a buoyant jet as defined in Figure 4.22 in a local natural coordinate system (s, n_s) where s is the streamwise coordinate along the jet centreline and n_s is a normal to s. The velocity $u(s, n_s)$ and density deficit $\Delta\rho = \rho_a - \rho(s, n_s)$ are self-similar and Gaussian i.e.

$$u(s, n_s) = u_c(s)e^{-n_s^2/b_g^2}, \qquad \Delta\rho(s, n_s) = \Delta\rho_c(s)e^{-n_s^2/\lambda^2 b_g^2} \tag{4.76}$$

where u_c and $\Delta\rho_c$ are the centreline velocity and density deficit, and b_g is the characteristic plume radius. We express the volume flux, $Q = \int u\,\mathrm{d}A$, specific momentum flux, $M = \int u^2\,\mathrm{d}A$ and specific buoyancy flux, $F = \int ug'\,\mathrm{d}A$

using

$$
\begin{aligned}
\frac{\mathrm{d}Q}{\mathrm{d}s} &= 2\pi b_g(\alpha u_c) && (4.77)\\
\frac{\mathrm{d}M_z}{\mathrm{d}s} &= \frac{\pi\lambda^2 b_g^2(\rho_a-\rho_c)g}{\rho_a} && (4.78)\\
\frac{\mathrm{d}M_x}{\mathrm{d}s} &= -\sin\phi\left[\oint n_x\frac{P}{\rho}\,\mathrm{d}S + \oint q_x(\boldsymbol{n}\cdot\boldsymbol{q})\,\mathrm{d}S\right] && (4.79)\\
\frac{\mathrm{d}M_y}{\mathrm{d}s} &= -\sin\phi\left[\oint n_y\frac{P}{\rho}\,\mathrm{d}S + \oint q_y(\boldsymbol{n}\cdot\boldsymbol{q})\,\mathrm{d}S\right] && (4.80)\\
\frac{\mathrm{d}F}{\mathrm{d}s} &= 0 && (4.81)\\
\frac{\mathrm{d}x}{\mathrm{d}s} &= \cos\phi\cos\theta,\quad \frac{\mathrm{d}y}{\mathrm{d}s} = \cos\phi\sin\theta,\quad \frac{\mathrm{d}z}{\mathrm{d}s} = \sin\phi, && (4.82)
\end{aligned}
$$

where $M = \left(M_x^2 + M_y^2 + M_z^2\right)^{1/2}$. The centreline variables u_c and ρ_c are related to fluxes using

$$
Q = \pi u_c b_g^2,\quad M = \frac{\pi}{2}u_c^2 b_g^2,\quad F = \frac{\lambda^2}{1+\lambda^2}\pi u_c b_g^2\frac{(\rho_a-\rho_c)}{\rho_a}g. \tag{4.83}
$$

The entrainment coefficient, α, is expressed as a function of the local jet Froude number

$$
F_{r_L} = \frac{u_c}{\sqrt{gb_g\left(\Delta\rho_c/\rho_a\right)}}
$$

and the local vertical jet orientation ϕ:

$$
\alpha = \alpha_j + (\alpha_p - \alpha_j)\left(\frac{F_{r_p}}{F_{r_L}}\right)^2\sin\phi
$$

with $\alpha_j = 0.057$, $\alpha_p = 0.085$ and $F_{r_p} = \sqrt{\frac{5\lambda^2}{4\alpha_p}}$. The dynamic interaction between plumes is captured by the integral term of (4.79) and (4.80). This integral is calculated on each spatial interval over a closed control volume, which was chosen as a square, of side length $\frac{1}{2}$, centred at (x,y). It was shown, by Lai [71], that the value of this integral is independent of the chosen control volume. This system of equations must be solved on each discrete interval, for each plume. We take $\lambda = 1.2$, as found by Fischer *et* *al.* [74].

By expressing (4.77) - (4.82) in terms of fluxes (Q, M_x, M_y, M_z, F), this system of equations may be solved numerically using MATLAB's stiff solver 'ode15s' subject to initial conditions $(Q_0, M_{x0}, M_{y0}, M_{z0}, F_0, x_0, y_0, z_0)$ and the equation of state for pressure, given by (4.75).

4.7.2 Merging Height from the ODE Model

By solving (4.77) - (4.82), we find the centrelines of each plume. Furthermore, using (4.76), we compute the the buoyancy profile of the configuration at each s. Finally, using MATLAB peak detection, we are able to determine the height, z, where the N plumes have a single combined peak. This is the merging height of the numerical model. Example outputs for 2, 3 and 4 equi-spaced, equal strength co-linear plumes are shown in Figure 4.23.

The merging heights found from the Lai ODE model (4.77) - (4.82) are compared to the merging heights found with the model derived in §4.3.2 - §4.3.3 and the experimental results from §4.6 in Table 4.4. Note that the values in Table 4.4 are given as non-dimensional merging heights. To convert to dimensional units, these values must be multiplied by the separation distance, χ_0.

Configuration	Lai	Interacting Model	Experiments
Line of two	4.71	5.08	5.09 ± 5.57%
Line of three	4.95	5.30	5.32 ± 8.03%
Line of four	6.71	6.48	6.30 ± 9.86%

Table 4.4: Comparison of merging heights for co-linear plumes found using the Lai ODE model, the model derived in §4.3.2 - §4.3.3 and experimental results from §4.6.

We see that the merging heights given in Table 4.4 are in close agreement, giving strong validation to the model derived in this chapter. We also

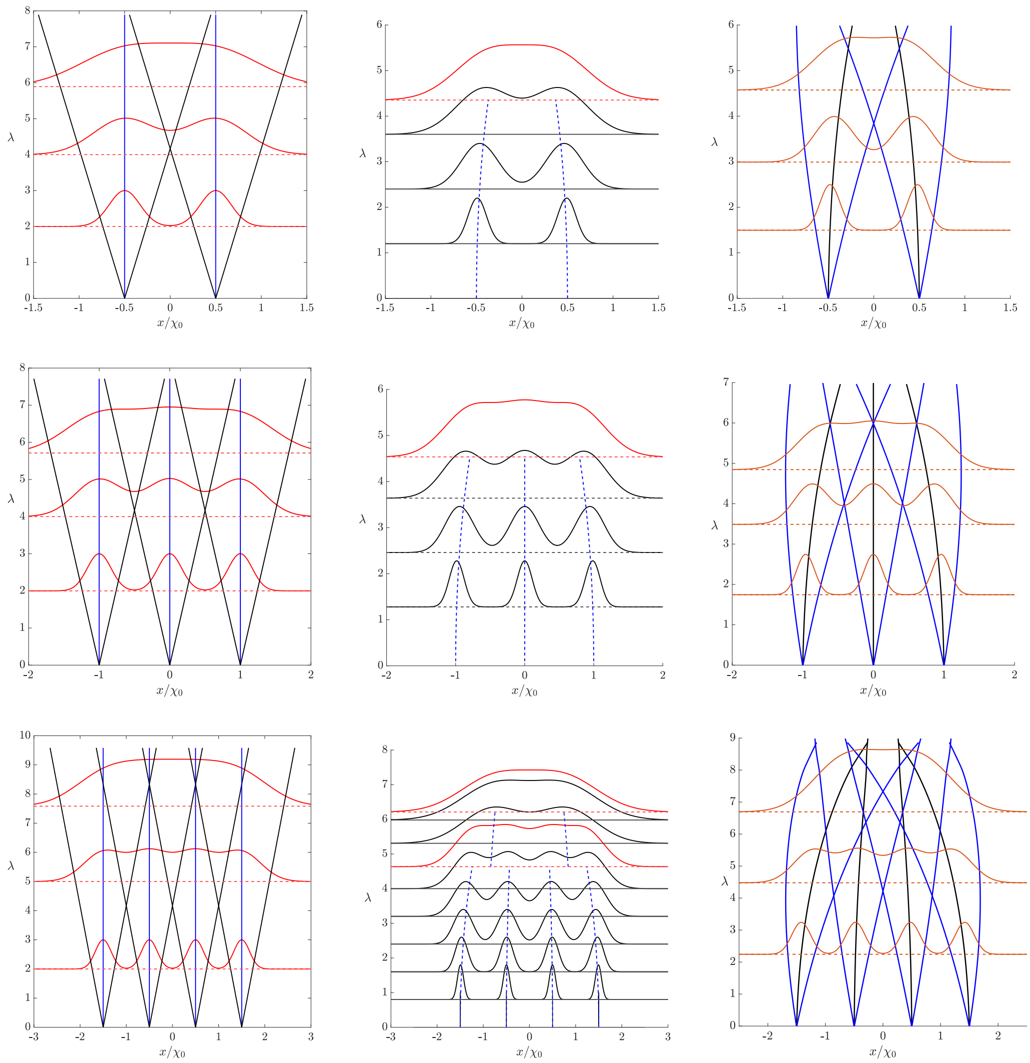

FIGURE 4.23: Example outputs of the non-interacting (left), interacting (middle) and Lai ODE models (right) for two, three and four plumes. For the non-interacting and Lai models, the black curves show the centreline location of the plumes, the blue curves show the location of the edges of the plumes, and the red (solid) line gives the buoyancy profile at the height shown by the red (dashed) line. For the interacting model, the plume curves show the centreline of the plumes and the black show the buoyancy profile. The red curves show, for two and three plumes the buoyancy profile at the merging height. For four plumes there are two red curves - the first (at the lower height) shows buoyancy profile at the height where four plumes merge to two. The second shows this where two plumes merge into one, i.e the merging height.

compare the merging heights found from the Lai model to both the non-interacting and interacting models derived previously. This is shown in Figure 4.5.

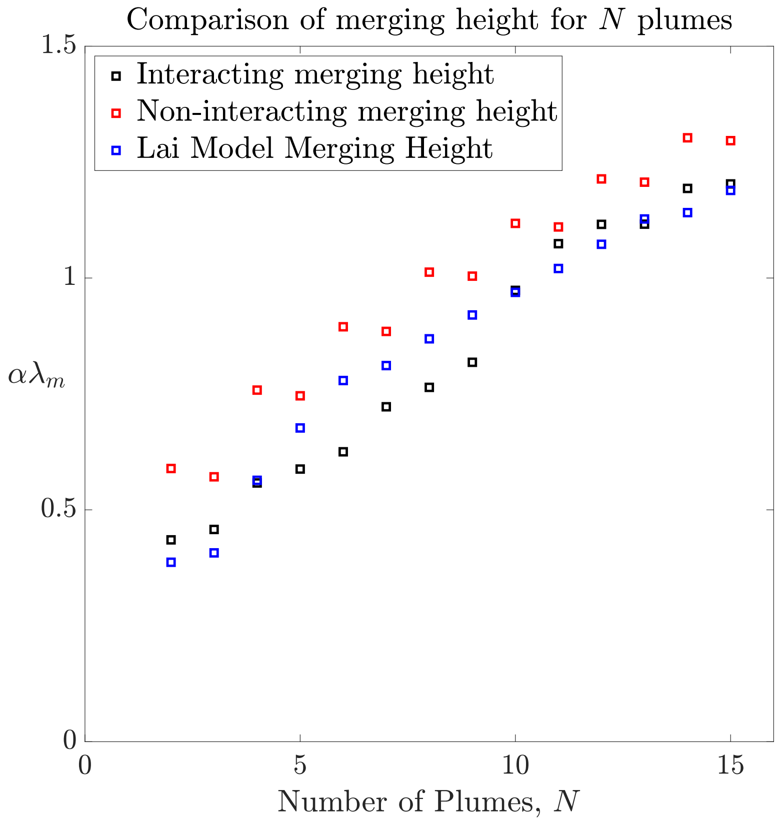

FIGURE 4.24: Plot comparing the non-interacting merging height (given in table 3.1) and the interacting merging height (given in table 4.1) to the merging heights computed using the Lai model given by (4.77) - (4.82). Note that the Lai merging heights are multiplied by the plume entrainment coefficient used in the Lai model ($\alpha_p = 0.085$) and not the entrainment coefficient used previously ($\alpha = 0.1$).

Furthermore, we are able to determine the merging height of arrays of plumes. In particular, we find the merging heights for an equilateral triangle of plumes, and 2×2 square grid of plumes. These non-dimensional merging heights are $\lambda_m = 3.86$ and $\lambda_m = 4.13$ for the triangle and the grid respectively. The surfaces at these heights are given in Figure 4.25 and Figure 4.26 respectively. We see that these values are close to the model results from an array of plumes in §4.4 and the experimental results from §4.6 as shown in Table 4.5.

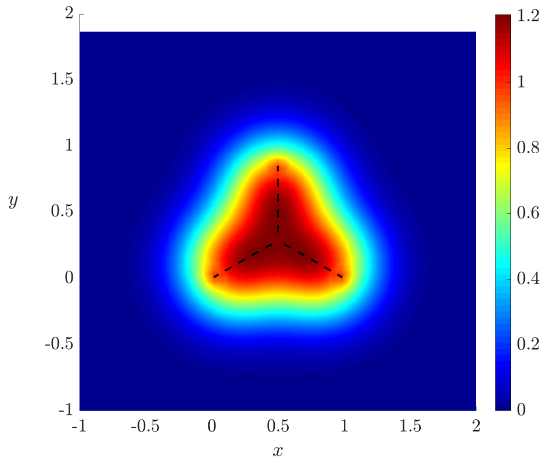

Figure 4.25: Buoyancy surface at $\lambda = \lambda_m = 3.86$ for an equilateral triangle array of equal strength plumes. The black dashed lines show the path of the centreline of each plume following Lai's model.

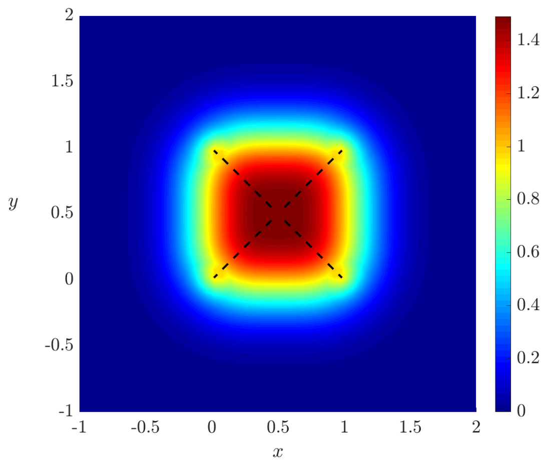

Figure 4.26: Buoyancy surface at $\lambda = \lambda_m = 4.13$ for an 2×2 square array of equal strength plumes. The black dashed lines show the path of the centreline of each plume following Lai's model.

Configuration	Lai	Interacting Model	Experiments
Equilateral Triangle	3.86	3.70	$3.69 \pm 3.25\%$
2×2 Grid	4.13	4.20	$3.89 \pm 7.45\%$

Table 4.5: Comparison of merging heights for plumes in an array found using the Lai ODE model, the model derived in §4.3.2 - §4.3.3 and experimental results from §4.6.

4.8 Summary

This chapter has extended the work of §3, which sought to find the height at which a line of plumes would behave as a single, larger plume if interaction between plumes was ignored. An interacting model was devised, based on the assumption that the strength of plume interaction is inversely proportional to the distance between the plumes. For two plumes, this model collapses to the interacting model of Kaye & Linden [38].

This model was further generalised to an arbitrary, finite number of interacting co-linear plumes by considering the entrainment experienced by a plume due to its neighbours. Doing so led to the model given in §4.3.2 - §4.3.3. This model was extended to two arrays of interacting plumes - an equilateral triangle and a 2×2 grid.

The interacting models from §4.3 and §4.4 were then compared to data collected from experiments for five configurations. The method of data collection and extraction of the merging height from the experimental data was outlined. The models were compared to the experimental data in Figures 4.16 - 4.20. We saw that these interacting models were in good agreement with the experimental data.

The predictions from the models derived in this chapter were also compared to those from the ODE model for dynamic interacting jets given by (4.77) - (4.82). We find that the model predictions are in good agreement for co-linear plumes and in an array. These models are in further agreement with the experimental data for co-linear plumes and the arrays.

Chapter 5

Plumes in a Cross-Flow: Theory

5.1 Motivation

The work presented in §3 - §4 has considered the simplified case of plumes in a stationary environment. These models allowed a closed form solution for the merging height of a line of plumes, but are severely limited in their physical applications. Namely, these models cannot be applied to rivers because there is always a flow in a river. In this chapter the model is developed so that it captures the behaviour of plumes in a cross-flow - from thermal plumes in rivers to chimney stacks in wind.

An additional layer of complexity is introduced due to the inherent turbulence present in the ambient environment. For example, rivers are always turbulent, typically with Reynolds numbers of the order 10,000 [75]. Time-averaged or steady state models will be used to model both the turbulence of the plume, and the turbulence of the river. An interesting phenomenon also exhibited by plumes in a cross-flow, known as the blockage effect, is introduced in §5.2, which adds further difficulty in modelling the behaviour of these plumes.

In §5.3 we examine several existing models for the behaviour of plumes in a cross-flow, but note that most of these are not able to be extended to multiple plumes due to the inability to capture the so-called "blockage effect"[76] (this is known as the blockage effect in this thesis). These existing models are instead particularly useful for capturing the behaviour of a single plume in various physical scenarios where a general model wouldn't suffice. From these existing models, we develop the one most readily extended to multiple plumes, and implement a model of the blockage effect. Finally, this extended model is validated against laboratory experiments conducted in a 5 m flume in §6.

5.2 The Blockage Effect

The blockage effect is the name given to a phenomenon observed when plumes in a line are exposed to a cross-flow. It can be seen that the upstream plumes are significantly more bent-over by the flow than the downstream plumes. This can be thought of as the upstream plumes shielding the downstream plumes from the flow. This can be thought of analogously to large vehicles in the left hand lane of the motorway shielding smaller ones in the right hand lanes from a prevailing wind, perpendicular to the direction of travel, on a motorway. Furthermore, these plumes bend significantly once they rise beyond the upstream plumes since they are no longer shielded. This can also be thought of using the motorway analogy, since the smaller vehicle will feel a crosswind when it passes the larger vehicle.

This behaviour was first modelled by Wooler *et al.* [76] to explain the behaviour of air flowing over the wing of a jet. While this behaviour was only noted for two plumes in [76], it was later observed for four and eight jets in the work of Yu *et al.* [77] as seen in Figure 5.1. Seeing this behaviour exhibited for two, four and eight jets suggests it will be shown for any number of jets and, by extension, plumes. Indeed, this was will be shown in three plumes as seen in §6.4. Therefore, this behaviour must be captured to give an accurate model of a line of plumes in a cross-flow.

5.3 Existing Cross-flow Models

5.3.1 Hoult *et al.*

The majority of models for a single plume in a cross-flow are based on, or extensions of, the work of Hoult & Weil [78] which uses theoretical observations given in [79]. It is important to note that these models are developed for round-source, not line-source plumes. These observations readily lend themselves to a two parameter model of entrainment, one parameter for the tangential component of entrainment and the other for the normal component. We introduce the following notation as used in [78]: let (s, θ) denote the curvilinear coordinate system where s is the distance along the curved centreline of the plume and θ be the anti-clockwise angle from the horizontal to the centreline of the plume at s. We define b and w as the plume radius and centreline velocity at a position s. These quantities are shown in Figure 5.2. As in §3, define Q, M and F as the specific mass, momentum and buoyancy fluxes given by

$$Q = b^2 w, \qquad M = b^2 w^2, \qquad F = b^2 w g' = b^2 w g \left(\frac{\rho_a - \rho}{\rho_a} \right)$$

where g is the acceleration due to gravity, ρ_a the ambient density and ρ the density at the plume centreline.

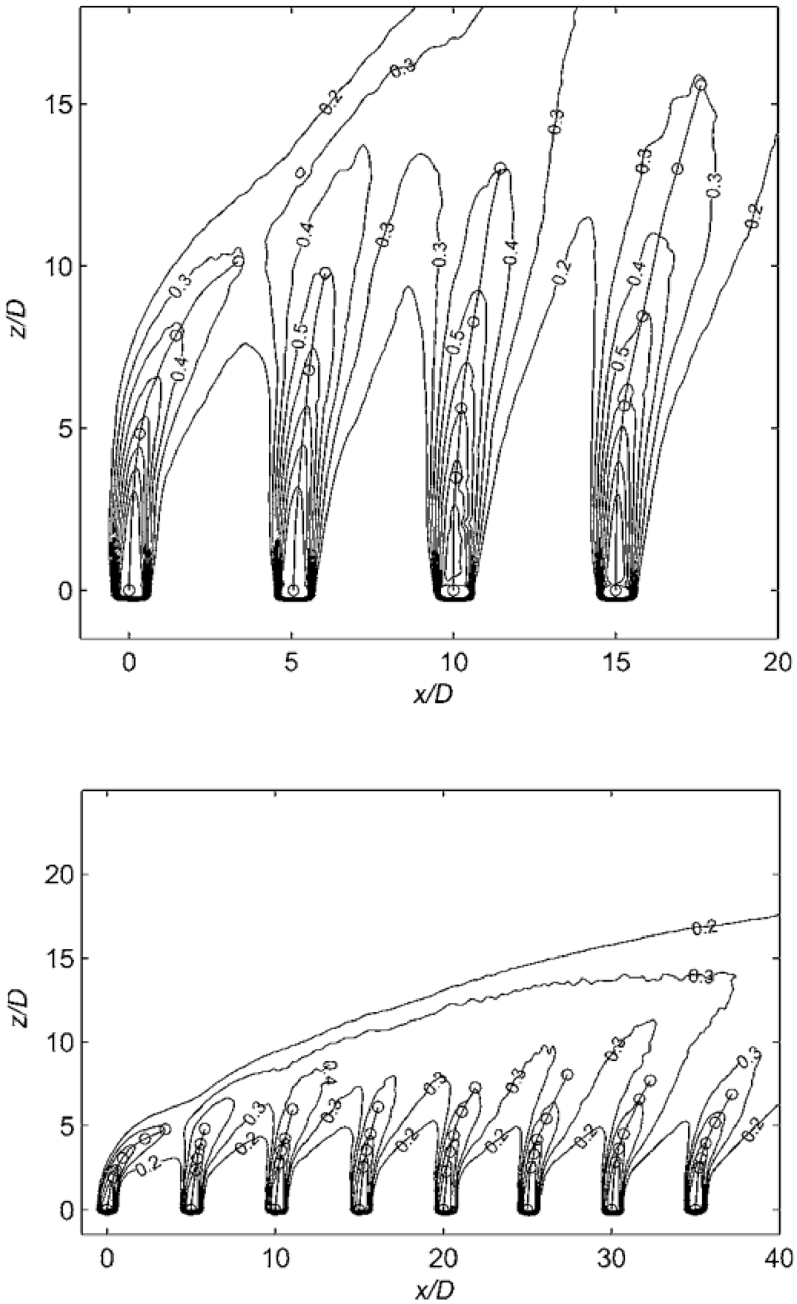

FIGURE 5.1: Figure 5 from [77] showing concentration contours and the blockage effect seen in four and eight jets in a line. For the four plume experiment, the ratio of source velocity and cross-flow is given by $\frac{U_0}{U_a} = 9.9$. For eight, $\frac{U_0}{U_a} = 4.2$. This data is non-dimensionalised with the jet diameter, D.

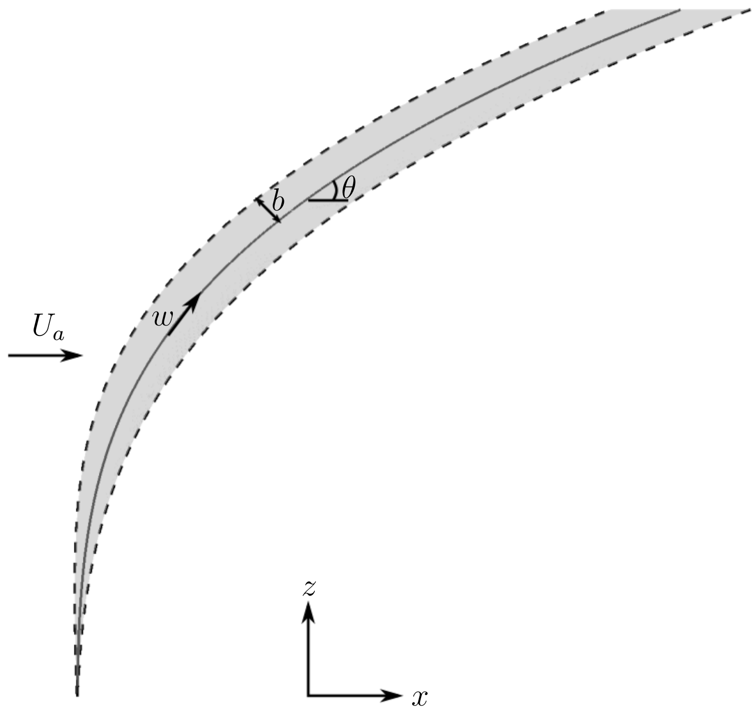

Figure 5.2: A visual representation of the quantities of a plume in a cross-flow.

The model for a single plume in a cross-flow is then given by:

$$u_e = \alpha|w - U_a \cos\theta| + \beta|U_a \sin\theta| \tag{5.1}$$

$$\frac{\mathrm{d}Q}{\mathrm{d}s} = 2\frac{Q}{\sqrt{M}}u_e \tag{5.2}$$

$$\frac{\mathrm{d}M}{\mathrm{d}s} = U_a \cos\theta \frac{\mathrm{d}Q}{\mathrm{d}s} + \frac{FQ}{M}\sin\theta \tag{5.3}$$

$$\frac{\mathrm{d}\theta}{\mathrm{d}s} = -\frac{U_a \sin\theta}{M}\frac{\mathrm{d}Q}{\mathrm{d}s} + \frac{FQ}{M^2}\cos\theta \tag{5.4}$$

$$\frac{\mathrm{d}F}{\mathrm{d}s} = 0 \tag{5.5}$$

$$\frac{\mathrm{d}x}{\mathrm{d}s} = \cos\theta \tag{5.6}$$

$$\frac{\mathrm{d}z}{\mathrm{d}s} = \sin\theta \tag{5.7}$$

where α and β denote tangential and normal entrainment parameters respectively, and U_a is the horizontal component of the velocity of the ambient fluid i.e. the cross-flow. This model reduces immediately to the single plume model of Morton, Taylor and Turner [33] when $\theta = \frac{\pi}{2}$ and $U_a = 0$, i.e for a vertical plume in a stationary environment.

This model can be non-dimensionalised using

$$\begin{gathered} Q = Q_0 Q^*,\ M = M_0 M^*,\ F = F_0 F^* \\ s = b_0 s^*,\ w = w_0 w^*,\ U_a = w_0 U_a^* \end{gathered} \tag{5.8}$$

to give (with stars removed)

$$u_e = \alpha|w - U_a \cos\theta| + \beta|U_a \sin\theta| \tag{5.9}$$

$$\frac{\mathrm{d}Q}{\mathrm{d}s} = 2\frac{Q}{\sqrt{M}}u_e \tag{5.10}$$

$$\frac{\mathrm{d}M}{\mathrm{d}s} = U_a \cos\theta \frac{\mathrm{d}Q}{\mathrm{d}s} + \mathit{\Gamma}\frac{FQ}{M}\sin\theta \tag{5.11}$$

$$\frac{\mathrm{d}\theta}{\mathrm{d}s} = -\frac{U_a \sin\theta}{M}\frac{\mathrm{d}Q}{\mathrm{d}s} + \mathit{\Gamma}\frac{FQ}{M^2}\cos\theta \tag{5.12}$$

$$\frac{\mathrm{d}F}{\mathrm{d}s} = 0 \tag{5.13}$$

$$\frac{\mathrm{d}x}{\mathrm{d}s} = \cos\theta \tag{5.14}$$

$$\frac{\mathrm{d}z}{\mathrm{d}s} = \sin\theta \tag{5.15}$$

where $\mathit{\Gamma} = \dfrac{F_0 Q_0^2}{M_0^{5/2}}$ and is analogous to the source Froude number defined in (3.28).

There is no general analytic solution for this cross-flow model. However, a solution for the plume trajectory for small deviations from the vertical was found by Hoult *et al.* [79] showing that a buoyant plume radius grows linearly with height when far from the source. Explicitly, it was shown that $b = \beta z$. By solving this model using ode15s in MATLAB for various values of U_a, we generate Figure 5.3. This shows that, when compared to $w_0 = 1$, the plume trajectories are progressively more bent-over as the horizontal component of the cross-flow velocity is increased.

This model can immediately be extended to an arbitrary number of non-interacting plumes simply by superimposing plumes with different origin conditions (x_0, z_0). However, there is no natural way to include interaction between plumes in this model. Therefore, it is not straightforward to extend to include the plume-to-plume interaction. A model that is more readily extended to account for interaction is given in Lai [71].

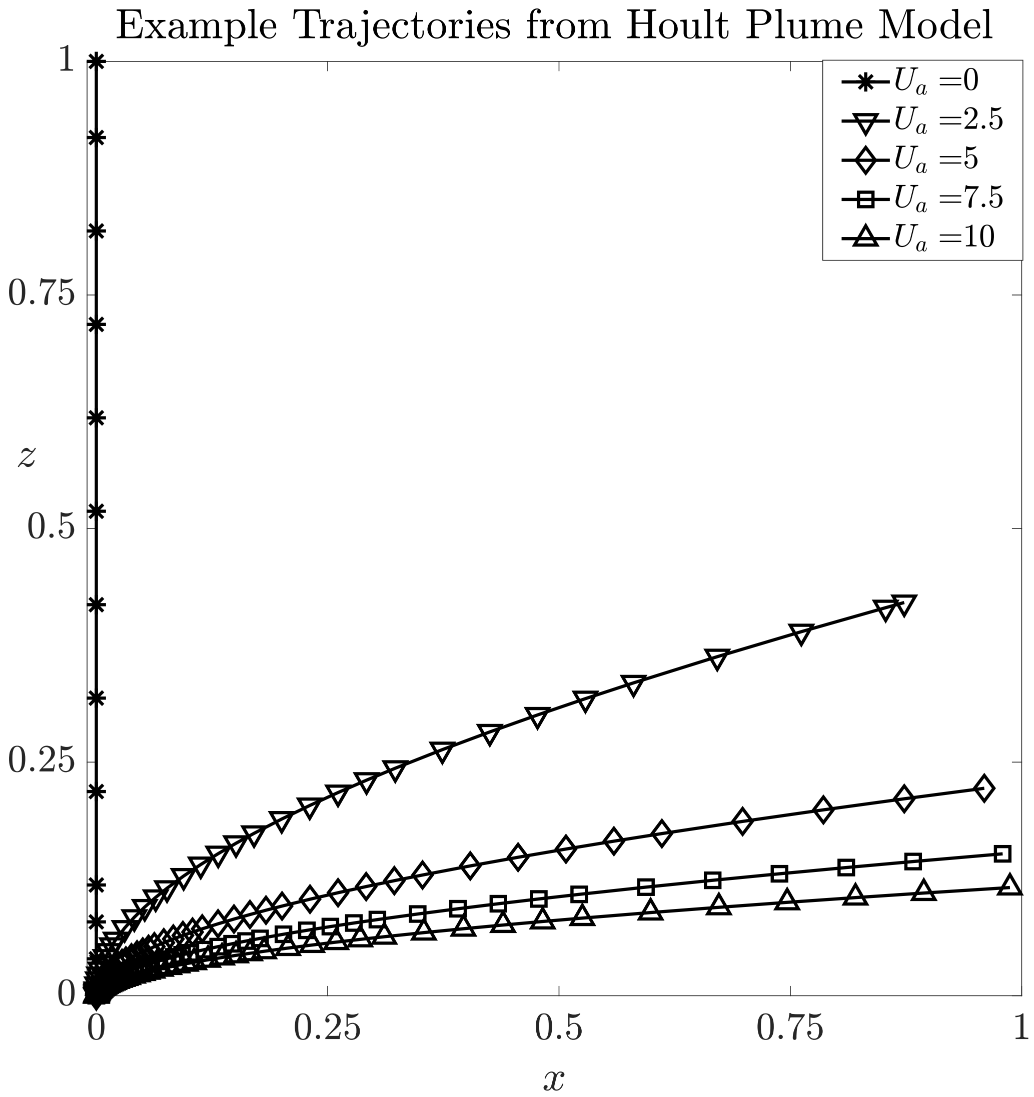

Figure 5.3: Sample solutions to the Hoult plume in a cross-flow model with initial conditions $(Q_0, M_0, F_0) = (1, 1, 1)$ and entrainment parameters $\alpha = 0.09$ and $\beta = 0.9$.

5.3.2 Lai

The modelling work by Lai was primarily for plumes in a stillwater environment, as was discussed in §4.7. This model can be extended to model a plume in a cross-flow by including the ambient velocity in the external flow field given by (4.73). For a horizontal cross-flow with velocity U_a, the u_y and u_z terms in (4.73) remain the same, while the u_x term becomes

$$u_x = U_a + \sum_{j=1}^{N_j} \sum_{i=1}^{N} (u_x)_{ij}$$

as discussed in [71]. In (5.3.2), the summation term describes the induced horizontal velocity from plume-to-plume interaction, as discussed in §4.7. the addition of U_a includes the horizontal cross-flow in the horizontal velocity component of the plumes. By including this cross-flow in the model given by (4.77)-(4.82) an approximation for the behaviour of a single plume in a cross-flow is obtained. However, the Lai model can also be generalised to an arbitrary number of interacting plumes in a cross-flow as the interaction is accounted for in (4.79)-(4.80). Two plumes in a cross-flow were simulated using the parameter values given in Table 5.1. The trajectories for this simulation are given in Figure 5.4.

Parameter	Symbol	Value
Number of plumes	N_j	2
Number of discretisation intervals	N_i	1000
Plume entrainment coefficient	α_p	0.085
Jet entrainment coefficient	α_j	0.057
Ambient density	ρ_a	$1000\,\mathrm{kg\,m^{-3}}$
Source density	ρ_0	$966\,\mathrm{kg\,m^{-3}}$
Cross-flow velocity	U_a	$0.044\,\mathrm{m\,s^{-1}}$
Source velocity	w_0	$0.33\ \mathrm{m\,s^{-1}}$

Table 5.1: Inputs to the Lai model for plumes in a cross-flow

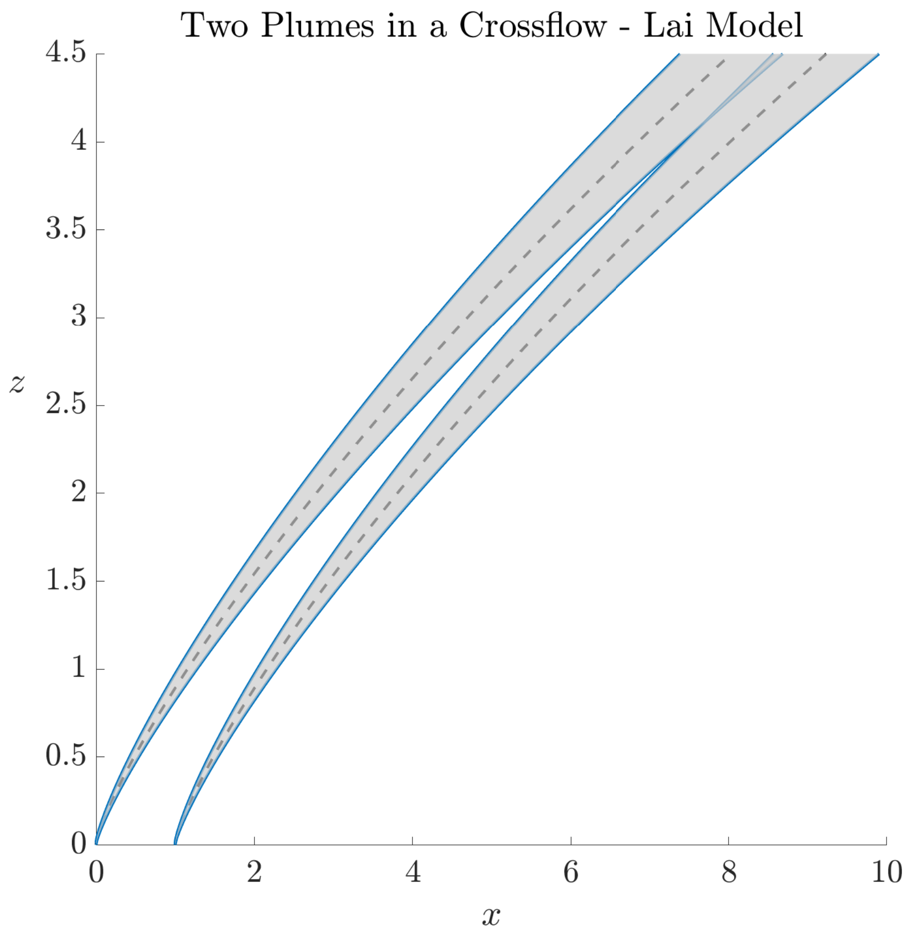

FIGURE 5.4: Example plume trajectories from the Lai model using parameters given in Table 5.1.

It is more straightforward to implement the blockage effect in [71] (this will be done in §5.4) but this model does not capture the nature of a single plume in a cross-flow, and therefore, even with the addition of the blockage effect, this model is unsuitable. There is no buoyancy dominated region near the source of the plumes since the plumes in Figure 5.4 do not rise vertically before being forced along a curved path by the cross-flow. This buoyancy dominated flow can be seen for low z/D in the experimental photos in Figure 5.1. Since this behaviour has been observed experimentally, it must be included in the modelling. The final existing model to be discussed in this chapter is JETLAG [37]. It will be shown that JETLAG exhibits the required behaviour, and can be extended to include an implementation of the blockage effect.

5.3.3 JETLAG

JETLAG is a Lagrangian model, derived in [80], which predicts the mixing of buoyant jets and plumes with three-dimensional trajectories. The unknown trajectory is modelled as a series of plume elements which increase in mass with distance from the source. This mass increase is caused by two physical factors - the shear-induced entrainment due to plume discharge and vortex entrainment due to the cross-flow. A full discussion of the work from which the JETLAG model is derived is given in [81, 82]. Here we introduce the notation of [37].

By modelling the k^{th} plume element, located at (x_k, y_k, z_k) as a cylinder with radius b_k and "height" (or long axis) as h_k. The velocity components of the plume element in the x, y and z directions are denoted u_k, v_k and w_k respectively, while $V_k = \sqrt{u_k^2 + v_k^2 + w_k^2}$ gives the speed of the plume element which is assumed constant through the plume element. The temperature, salinity and density of this k^{th} element are given by T_k, S_k and ρ_k respectively, where ρ_k is a function of T_k and S_k. That is, density is a function of both salinity and temperature. Then the mass of this plume element is given by $M_k = \rho_k \pi b_k^2 h_k$. The model depends on two angles, ϕ_k and θ_k, which are the angle between the plume and the horizontal plane, and the azimuthal angle. The changes in plume elements are examined over discrete time steps Δt. A typical cylindrical element is given schematically in Figure 5.5

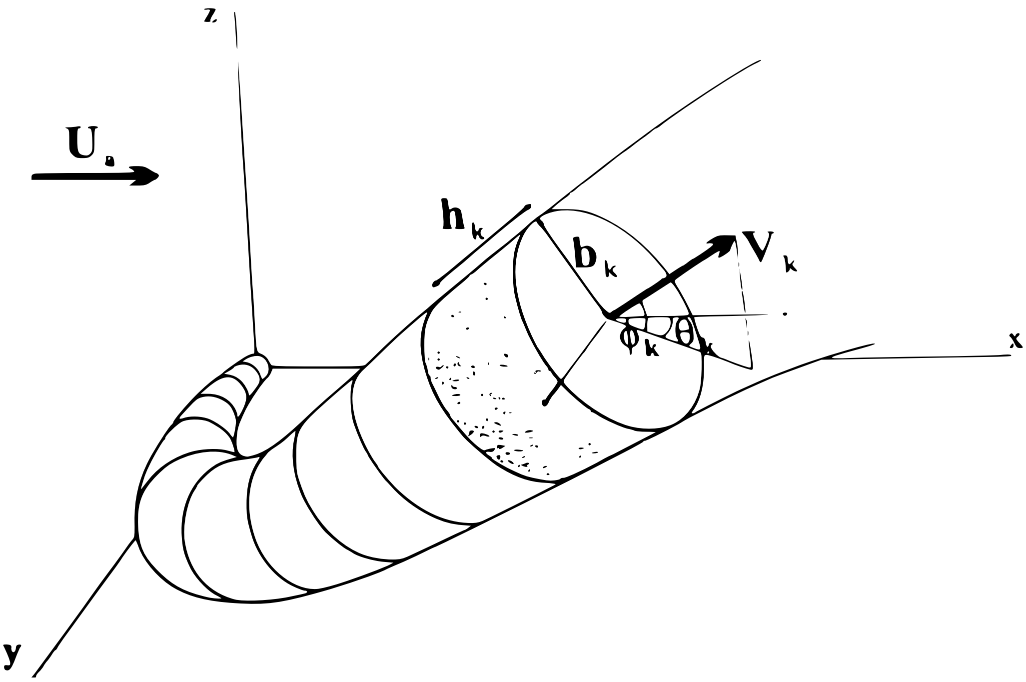

Figure 5.5: Schematic of a typical JETLAG plume showing the cylindrical element. This is Figure 10.7 in [37].

First consider the shear and vortex entrainment, which are required to find the change in mass due to turbulent entrainment, ΔM_k.

The shear entrainment, ΔM_s, at the k^{th} plume element is found with

$$\Delta M_s = 2\alpha_s b_k h_k \Delta U \Delta t \tag{5.16}$$

$$\alpha_s = \sqrt{2}\left(c_1 + c_2 \frac{\sin\phi_k}{F_l^2}\right)\left(\frac{2V_k}{\Delta U + V_k}\right) \quad \text{where} \tag{5.17}$$

$$\Delta U = |V_k - U_a \cos\theta_k \cos\phi_k| \quad \text{and} \tag{5.18}$$

$$F_l = \frac{\Delta U}{\sqrt{g\left(\frac{\rho_a - \rho_k}{\rho_a}\right) b_k}} \tag{5.19}$$

where $c_1 = 0.057$ and $c_2 = 0.554$ as given in [80, 37].

In the above system of equations, ΔU is the change in velocity of the plume due to entrainment in the direction of the centreline, α_s is the (local) entrainment coefficient and F_l is the local densimetric Froude number.

The vortex entrainment (or entrainment due to vorticity), ΔM_f, relies on a so-called "Projected Area Entrainment (PAE)" hypothesis found in [81, 80, 82]. The PAE hypothesis has three contributing terms: the projected area term (A_p), the increase in area due to plume growth (A_w) and the correction due to curvature (A_c). The PAE hypothesis is given by the sum of these three terms. The vortex entrainment is given by the following expression:

$$\begin{aligned}\Delta M_f &= \rho_a U_a \Big[2 b_k h_k \sqrt{1 - \cos^2\theta_k \cos^2\phi_k} + \pi b_k \Delta b_k \cos\phi_k \cos\theta_k \\ &+ \frac{\pi b_k^2}{2} \Delta(\cos\theta_k \cos\phi_k)\Big] \Delta t \\ &= \rho_a U_a \Delta t (A_p + A_w + A_c)\end{aligned} \tag{5.20}$$

and initial iteration of which is given by

$$\begin{aligned}\Delta M_f &= \rho_a U_a b_k h_k \Big[2\sqrt{1 - \cos^2\theta_k \cos^2\phi_k} \\ &+ \pi \frac{\Delta b_k}{\Delta s_k} \cos\phi_k \cos\theta_k \\ &+ \frac{\pi b_k}{2} \frac{(\cos\theta_k \cos\phi_k - \cos\theta_{k-1} \cos\phi_{k-1})}{\Delta s_k}\Big] \Delta t.\end{aligned} \tag{5.21}$$

Note that the term under the square root in (5.21) is equivalent to, but of a different form to that used in [80, 37]. The form chosen in [80, 37] was to minimise round off error. Finally, the change in mass due to turbulent entrainment, or the total entrainment is given by

$$\Delta M = \max(\Delta M_s, \Delta M_f). \tag{5.22}$$

Alternatively, one may use

$$\Delta M = \Delta M_s + \Delta M_f \tag{5.23}$$

however the former was seen to be in better agreement with experimental data [37].

Having determined the change in mass, the JETLAG model in terms of known equations is:

- Mass:

$$M_{k+1} = M_k + (\Delta M)_k \tag{5.24}$$

- Temperature, salinity and density:

$$S_{k+1} = \frac{M_k S_k + (\Delta M)_k S_a}{M_{k+1}} \tag{5.25}$$

$$T_{k+1} = \frac{M_k T_k + (\Delta M)_k T_a}{M_{k+1}} \tag{5.26}$$

$$\rho_{k+1} = \rho(S_{k+1}, T_{k+1}) \tag{5.27}$$

- Horizontal momentum:

$$u_0 = V_0 \cos\phi_0 \cos\theta_0 \tag{5.28}$$

$$v_0 = V_0 \cos\phi_0 \sin\theta_0 \tag{5.29}$$

$$u_{k+1} = \frac{M_k u_k + (\Delta M)_k U_a}{M_{k+1}} \tag{5.30}$$

$$v_{k+1} = \frac{M_k v_k}{M_{k+1}} \tag{5.31}$$

- Vertical momentum:

$$w_{k+1} = \frac{M_k w_k + M_{k+1} \left(\frac{\Delta\rho}{\rho}\right)_{k+1} g\Delta t}{M_{k+1}} \tag{5.32}$$

$$U_{k+1} = \left(u_{k+1}^2 + v_{k+1}^2\right)^{\frac{1}{2}} \tag{5.33}$$

$$V_{k+1} = \left(u_{k+1}^2 + v_{k+1}^2 + w_{k+1}^2\right)^{\frac{1}{2}} \tag{5.34}$$

- Cylinder dimensions:

$$h_0 = b_0 \tag{5.35}$$

$$h_{k+1} = \frac{V_{k+1}}{V_k} h_k \tag{5.36}$$

$$b_{k+1} = \left(\frac{M_{k+1}}{\rho_{k+1}\pi h_{k+1}}\right)^{\frac{1}{2}} \tag{5.37}$$

- Plume orientation:

$$\sin\phi_{k+1} = \frac{w_{k+1}}{V_{k+1}} \tag{5.38}$$

$$\cos\phi_{k+1} = \frac{U_{k+1}}{V_{k+1}} \tag{5.39}$$

$$\sin\theta_{k+1} = \frac{v_{k+1}}{U_{k+1}} \tag{5.40}$$

$$\cos\theta_{k+1} = \frac{u_{k+1}}{U_{k+1}} \tag{5.41}$$

- Trajectories:

$$\Delta t = \frac{h_0}{V_0} \tag{5.42}$$

$$x_{k+1} = x_k + u_{k+1}\Delta t \tag{5.43}$$

$$y_{k+1} = y_k + v_{k+1}\Delta t \tag{5.44}$$

$$z_{k+1} = z_k + w_{k+1}\Delta t \tag{5.45}$$

$$(\Delta s)_{k+1} = V_{k+1}\Delta t \tag{5.46}$$

To obtain the trajectories from the JETLAG model, a first iteration is performed using (5.16) and (5.21), and updating (5.24) - (5.46) for each point on the plume. These values are then stored and the next iteration takes (5.20), and repeats the same process. The iterative process is stopped when the following convergence criterion:

$$\left\{(x - x_{\text{prev}})^2 + (z - z_{\text{prev}})^2\right\}^{1/2} \leq \epsilon \tag{5.47}$$

is satisfied. The subscript "prev" denotes the value from the previous iteration, and the lack of subscript denotes the value from the current iteration. Note that y is not considered in (5.47) as the model is restricted to 2D. If 3D trajectories were desired, additional y dependence in (5.47) would be required. Taking $\epsilon = 10^{-4}$, it was stated in [37] that the JETLAG model should converge in approximately two iterations. This is seen when replicating their model. By taking $\epsilon = 10^{-14}$, convergence is obtained in six iterations. The rate of iterative convergence is linear, as shown in Figure 5.6.

The system of equations given above for the JETLAG model is only immediately applicable to non-interacting plumes; the effects of interaction and the blockage effect have yet to be included. Figure 5.7 shows a simulation of two plumes in cross-flow using the JETLAG model. Near the source (for small z), the plume rises near vertically, whereas far from the source the cross-flow begins to bend the plume. This agrees with what is seen experimentally, with a buoyancy dominant region near the source where the plume rises near vertically, and a momentum dominant region in the far field where the cross-flow forces the plume to significantly bend. Adding plume-to-plume interaction into the JETLAG model required determining how to model the blockage effect.

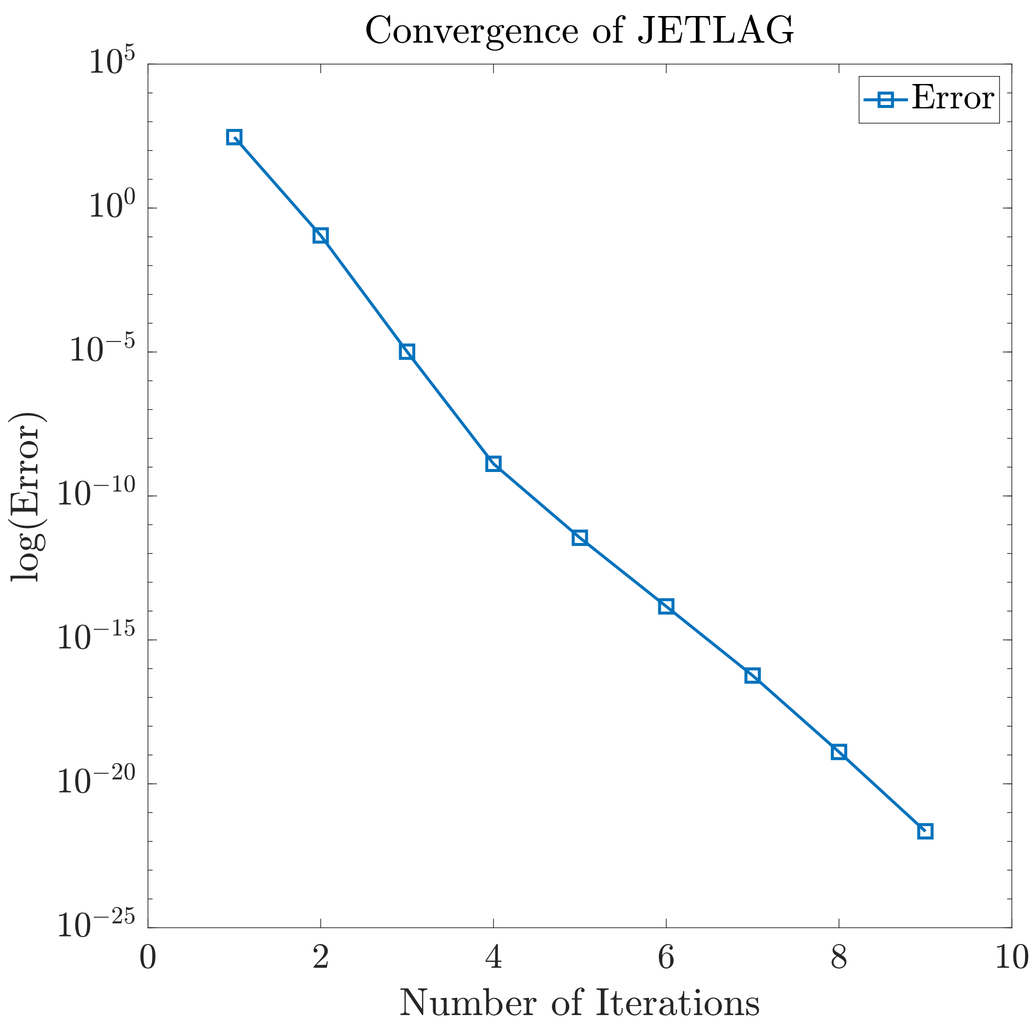

Figure 5.6: Semilog plot of the error between successive iterations of the JETLAG model, given by the LHS of (5.47).

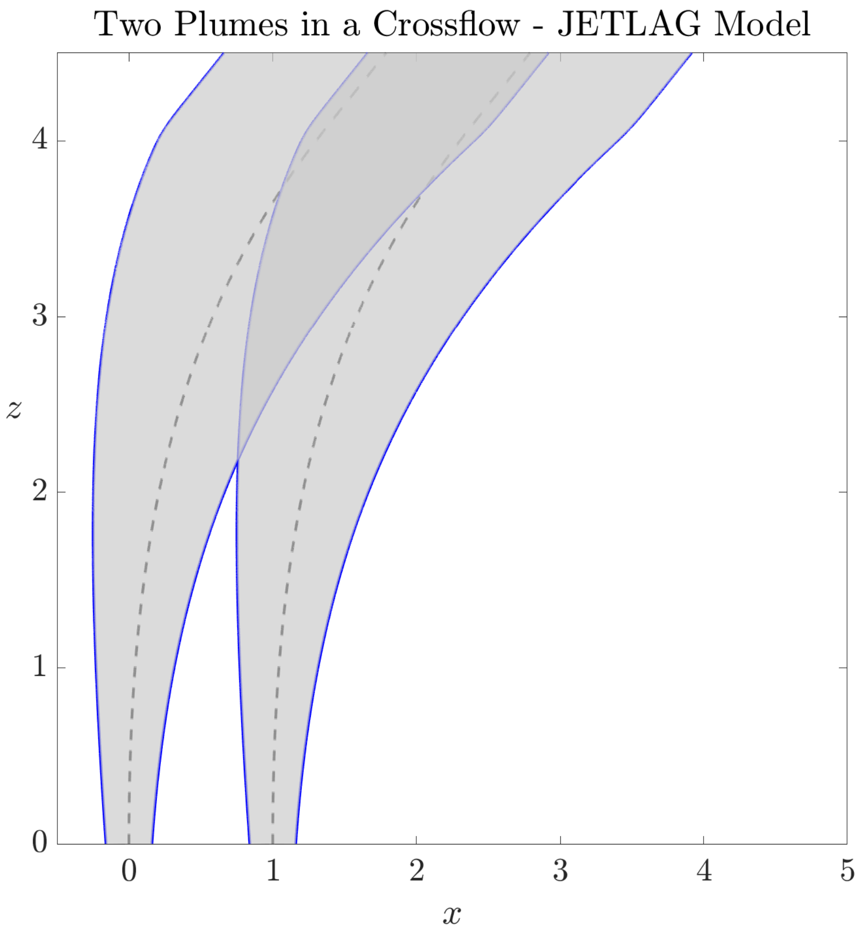

FIGURE 5.7: Sample trajectories from the JETLAG cross-flow model without interaction.

5.4 Implementing the Blockage Effect for Two Plumes

As discussed in §5.2, the blockage effect is seen in a line of plumes in a cross-flow. The effect itself is that the upstream plumes are significantly more bent-over than the downstream plumes. This suggests shielding by the upstream plumes to reduce the cross-flow felt by the downstream plumes. To capture the blockage effect, we model this reduced cross-flow.

We begin by considering the specific case of two plumes in a cross-flow. To leading order, the reduction in flow felt by a point on the downstream plume will be caused by the point closest to it on the upstream plume.

For a fixed point on the downstream plume, denoted (x_k, z_k), the closest point on the upstream plume is denoted (x_c, z_c) and is defined as

$$(x_c, z_c) = \left\{ (x^*, z^*) \text{ on first plume} \,\middle|\, \sqrt{(x^* - x_k)^2 + (z^* - z_k)^2} \text{ is minimised} \right\} \tag{5.48}$$

and the minimal distance is denoted χ_c. Recall from §4 that the entrainment of one plume on another is given, in the notation of JETLAG, by

$$F = -\frac{m}{2\pi}\frac{1}{r} = -\frac{\alpha b V}{\chi}$$

where b, V and χ are evaluated on the upstream plume. Then, by assuming that all shielding experienced by the downstream plume at (x_k, z_k) is due to the entrainment experienced due to the upstream plume at (x_c, z_c), the amount of shielding - or the reduction in flow, experienced at (x_k, z_k) is given by

$$F_k = -\frac{\alpha b_c V_c}{\chi_c} \tag{5.49}$$

where b_c, V_c denote the radius and centreline velocity on the point (x_c, z_c) and

α denotes the entrainment coefficient. The reduced cross-flow experienced at (x_k, z_k) is then given by

$$U_k^r = U_a + F_k. \tag{5.50}$$

Note that, in the limit of $U_a \to 0$, i.e. no cross-flow, the entrainment experienced by one plume from the other returns to the definition given in §4, and in turn this model will return to the previously discussed stillwater interacting model.

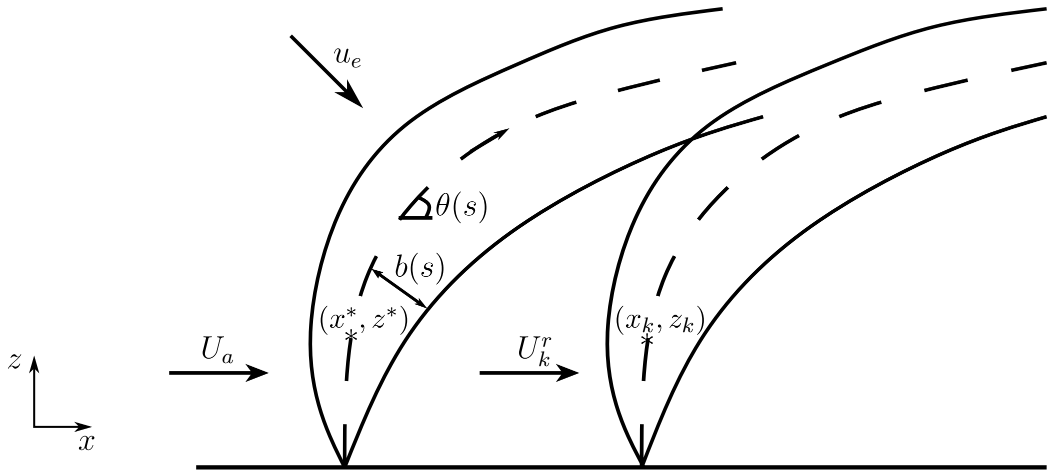

Figure 5.8: Schematic of two plumes in a cross-flow where the reduced cross-flow at point (x_k, z_k) is given by $U_k^r \leq U_a$.

By repeating this method for all points on the second plume, we obtain a reduced velocity for each point. The value of U_k^r replaces U_a in (5.16), (5.20) and (5.21) the next iteration of JETLAG. We then iterate the method to convergence as outlined in §5.3.3 and generate Figure 5.9. We see that the left plumes are identical between figures, but the right plume is significantly less bent-over in the second image which fits well with the experimental imagery of Yu in Figure 5.1. It is important to note that Figure 5.9 shows that the plumes pass through one-another, which is not physically true. Indeed, the plumes would be expected to merge instead of passing through each other. This is discussed in §5.4.2.

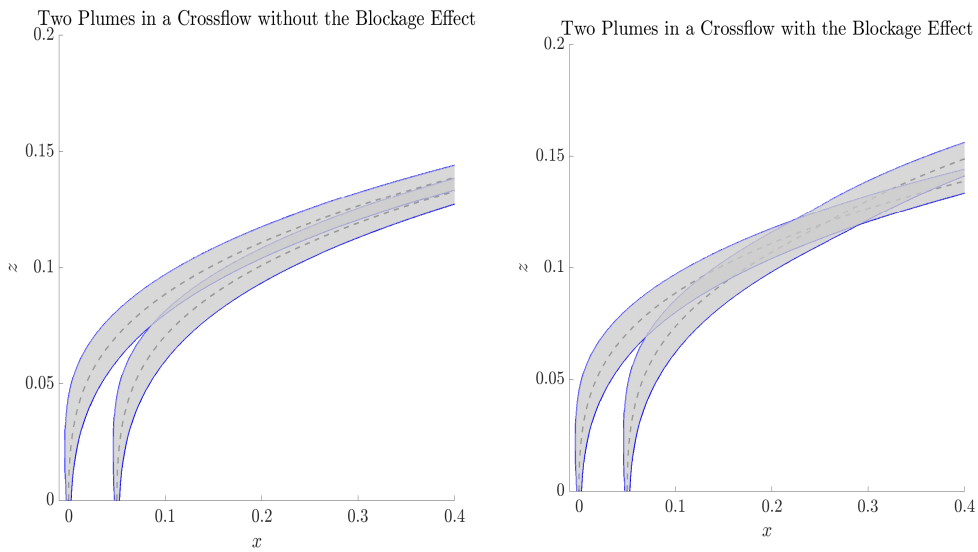

FIGURE 5.9: Figure showing the comparison between outputs from JETLAG. Left is the output with uniform cross-flow (no blockage effect) and right is with the blockage effect.

Figure 5.10 shows the errors between successive iterations in the same way as outlined previously, in §5.2. Also shown is that JETLAG converges linearly when including the blockage effect in the system of equations.

5.4.1 A General Blockage Effect

The modelling of the blockage effect can be generalised to an arbitrary number of plumes in a line. The flow reduction experienced by a point on a downstream plume can be approximated by the sum of the reductions from the closest point on each of the upstream plumes. Let N_p and N_s denote the number of plumes and spatial steps respectively. Define also n_p and n_s to be the current plume number and current spatial step number. Finally, define R_{n_s,n_p} to be the reduction in flow at point n_s on plume n_p. The method for computing the reduced flow is given as follows:

1. Set $n_s = 1$ and $n_p = 2$.

2. Extract the point (x_{n_s}, z_{n_s}) from plume n_p. Set $R_{n_s,n_p} = 0$.

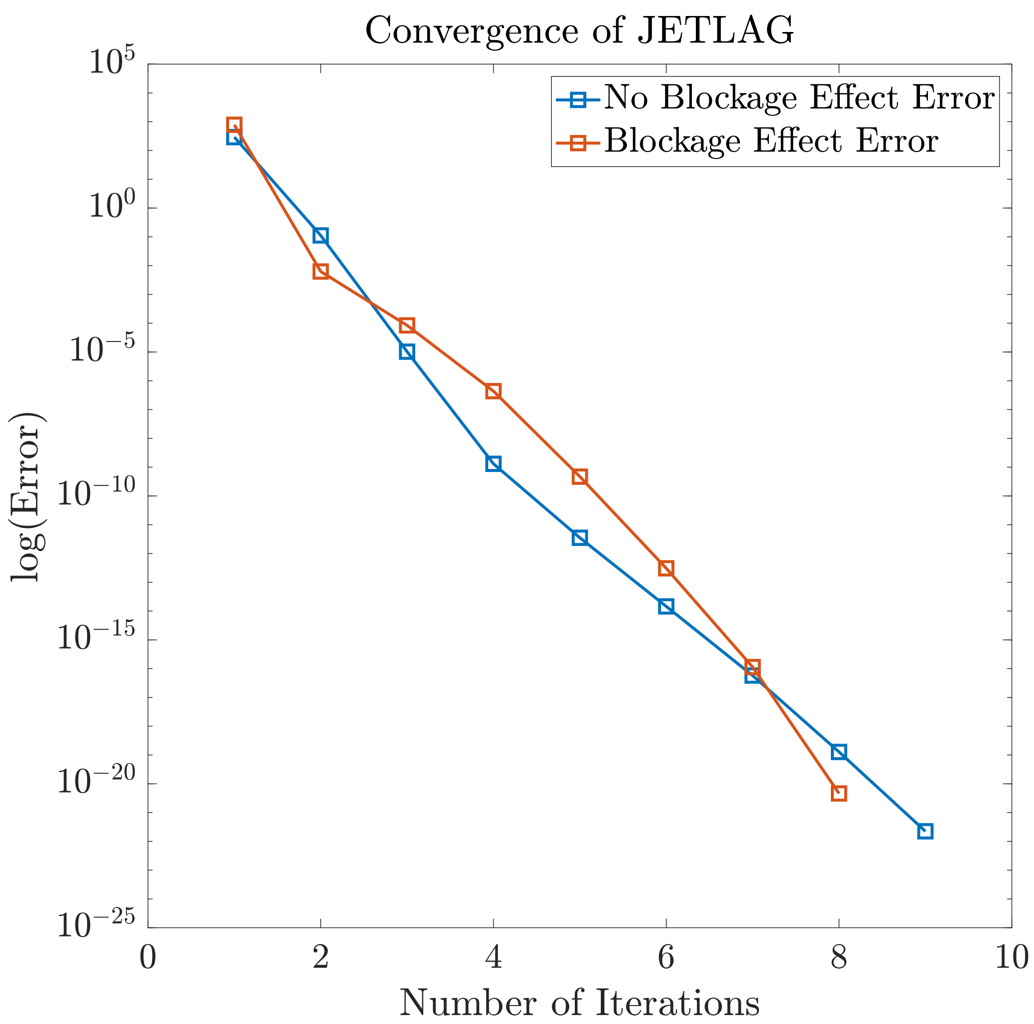

Figure 5.10: Plot of the convergence of the JETLAG model with and without the blockage effect.

3. For each plume upstream of the current one (i.e. for $k = 1 : n_p - 1$):

    - Extract the trajectory of plume k, defined as $(\boldsymbol{x}_k, \boldsymbol{z}_k)$.
    - Compute the shortest distance, χ_c, between plume k and the point (x_{n_s}, z_{n_s}), and the corresponding point (x_c, z_c). Denote any quantities at (x_c, z_c) by a subscript c.
    - update $R_{n_s,n_p} = R_{n_s,n_p} + \dfrac{\alpha b_c V_c}{\chi_c}$

4. Compute the reduced cross-flow $U^r_{n_s,n_p} = U_a - R_{n_s,n_p}$.

5. If $n_s < N_s$, update $n_s = n_s + 1$. Else $n_p = n_p + 1$, $n_s = 1$.

6. Continue until $n_s = N_s$ and $n_p = N_p$. This computes the reduced cross-flow for each of the relevant plumes in each location on the discretised centreline.

Figure 5.11 and Figure 5.12 show the results of using this algorithm for 4 and 8 plumes in a cross-flow using parameters and boundary conditions given in Table 5.2. The plume trajectories exhibit the behaviour shown experimentally by Yu *et al.* [77], giving preliminary validation to this model. Further experimental validation will be given in §6.

5.4.2 Modification of JETLAG: Merging

A key difference between the outputs from the JETLAG modelling discussed previously, and the experimental data given by Yu *et al.* [77] is seen in Figure 5.11. We see that the plume trajectories found by JETLAG pass through one another whereas in practice the plumes combine and remain so. The modelling extension is outlined for two plumes, and outlined for n co-linear plumes.

For two plumes, we expect the plumes to interact and merge into a single

Parameter	Value
Angle to the vertical, ϕ_0	$\frac{\pi}{2}$
Angle to the horizontal, θ_0	0
Centreline separation, χ_0	$0.01\,\mathrm{m}$
Plume radius, b_0	$10^{-3}\,\mathrm{m}$
Source temperature, T_0	$19\,°\mathrm{C}$
Ambient temperature, T_a	$21\,°\mathrm{C}$
Source Salinity, S_0	$0\,\mathrm{ppt}$
Ambient Salinity, S_a	$0\,\mathrm{ppt}$
Source tracer concentration, c_0	$0\,\mathrm{kg\,m^{-3}}$
Ambient tracer concentration, c_a	$0\,\mathrm{kg\,m^{-3}}$
Source density, ρ_0	$966\,\mathrm{kg\,m^{-3}}$
Ambient density, ρ_a	$1000\,\mathrm{kg\,m^{-3}}$
Centreline speed, V_0	$0.33\,\mathrm{m\,s^{-1}}$
Ambient cross-flow velocity, U_a	$0.014\,\mathrm{m\,s^{-1}}$

Table 5.2: Table containing the parameters used in JETLAG to generate Figure 5.11 and Figure 5.12.

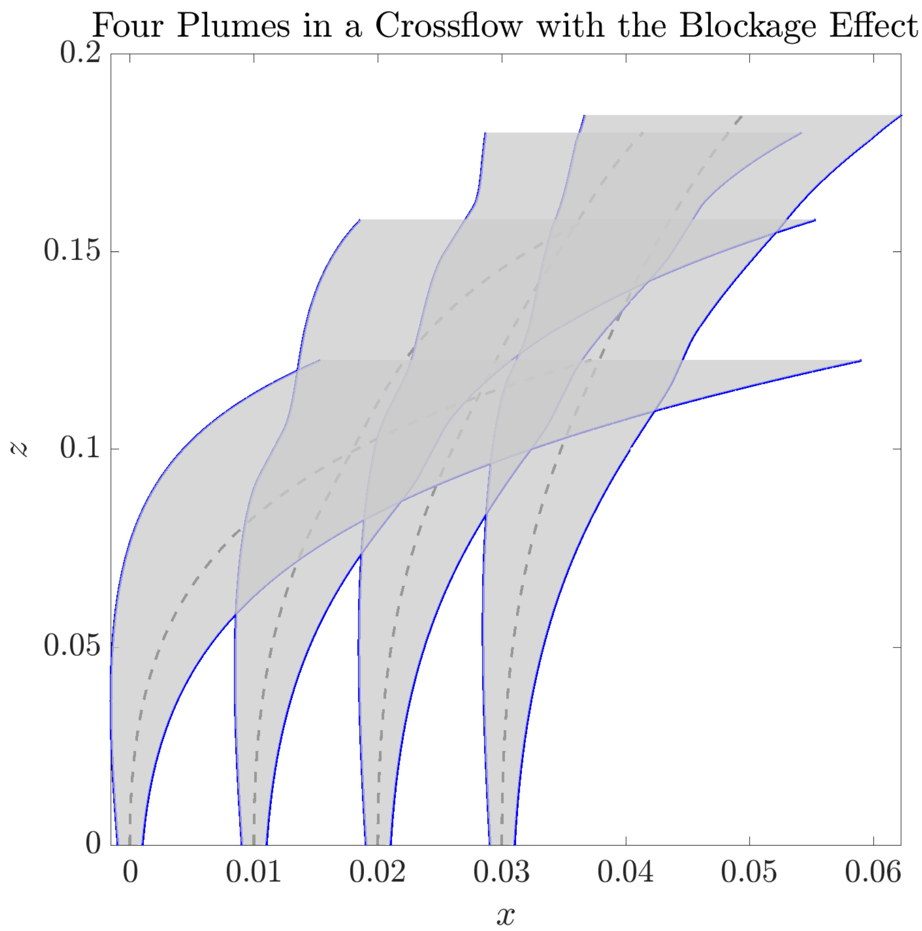

Figure 5.11: Simulation results for four plumes in a cross-flow with the blockage effect. Model inputs are given in Table 5.2.

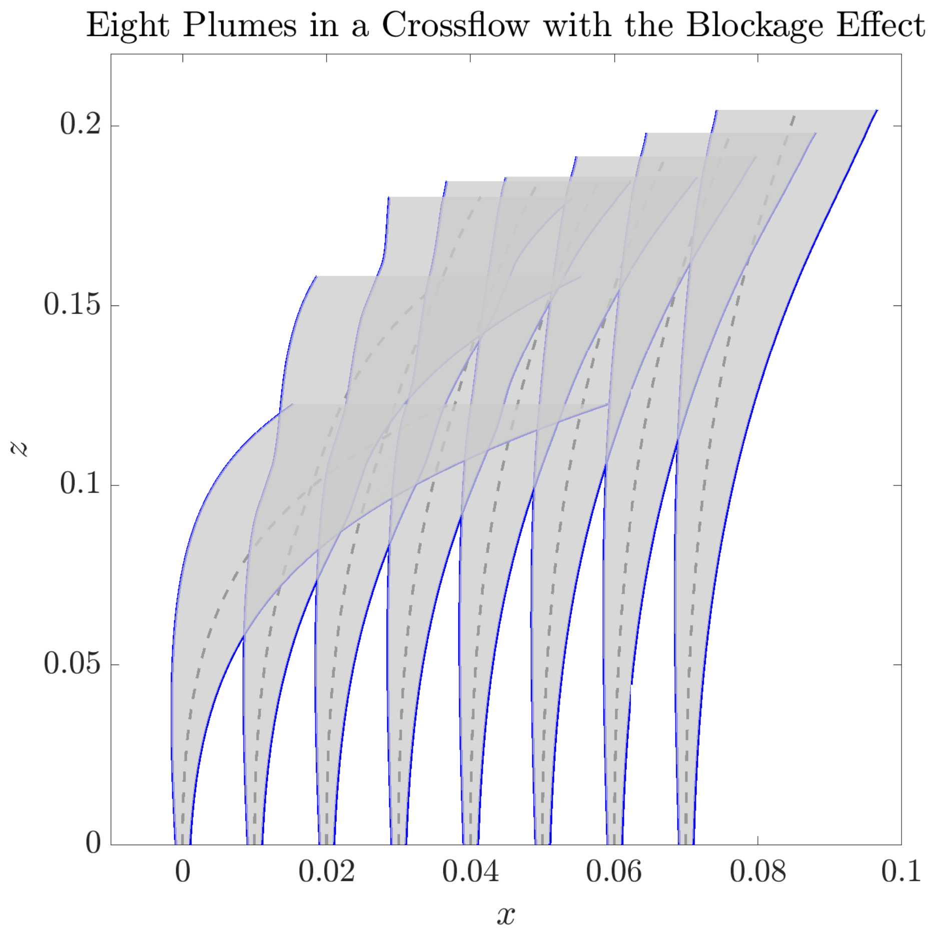

Figure 5.12: Simulation results for eight plumes in a cross-flow with the blockage effect. Model inputs are given in Table 5.2.

plume at some location (x_m, y_m, z_m). At this merging point, the merged plume will also have quantities as given in Table 5.2. Each of these quantities is calculable, but can not be determined without finding the merging point. To determine the merging point, the method of §4 is extended to a cross-flow. That is, the trajectories of the two distinct plumes are simulated, and their buoyancy profile determined using

$$E(x,y,z) = \sum_{j=1}^{\text{nPlumes}} \exp\left(-\frac{(x-x_j)^2 + (y-y_j)^2 + (z-z_j)^2}{b_j^2}\right) \tag{5.51}$$

where x_j, y_j, z_j, b_j are the coordinates and radii of each plume. Using MATLAB peak detecting, we find the peaks of (5.51) along the normal to the line segment connecting consecutive points on the centreline of the most downstream plume. When there is a single peak instead of two, the plumes have merged. This gives the merging point. For further detailed discussion of the merging point, see §6.

Specifically for two plumes, let subscripts m_1 and m_2 denote the quantity on plumes 1 and 2 at the merging point respectively. The coordinates of the new, merged, plume source is then given by the mean of the locations of the merging coordinates. i.e.

$$(x_0, y_0, z_0) = \frac{1}{2}\left(x_{m_1} + x_{m_2}, y_{m_1} + y_{m_2}, z_{m_1} + z_{m_2}\right). \tag{5.52}$$

To ensure continuity of the velocity scale we approximate the merged radius as

$$b_0 = \left(b_{m_1}^2 + b_{m_2}^2\right)^{1/2}. \tag{5.53}$$

Note that if $b_{m_1} = b_{m_2} = b_m$ then the merged radius is given by $b_0 = \sqrt{2}b_m$ which is preciously the result seen in (3.25) in §3.4.1.

To compute the merged velocities, we assume that at the point of merging, the plumes behave as though an inelastic (or plastic) collision had occurred. That is, the plume elements "stick together". In this case, the merged velocities are given by

$$(u_m, v_m, w_m) = \left(\frac{M_{m_1}u_{m_1} + M_{m_2}u_{m_2}}{M_{m_1} + M_{m_2}}, \frac{M_{m_1}v_{m_1} + M_{m_2}v_{m_2}}{M_{m_1} + M_{m_2}}, \frac{M_{m_1}w_{m_1} + M_{m_2}w_{m_2}}{M_{m_1} + M_{m_2}}\right) \tag{5.54}$$

where M denotes the mass of the plume element. Similarly, we may define U_m and V_m as

$$U_m = \sqrt{u_m^2 + v_m^2} \tag{5.55}$$

$$V_m = \sqrt{u_m^2 + v_m^2 + w_m^2} \tag{5.56}$$

from which we also obtain

$$\phi_m = \sin^{-1}\left(\frac{w_m}{U_m}\right). \tag{5.57}$$

Furthermore, we define $\theta_m = 0$ to ensure that the plumes remain restricted to the original 2D plane. Finally, the merged density, ρ_m, is computed using

$$\rho_m = \frac{M_{m_1} + M_{m_2}}{\pi b_{m_1}^2 h_{m_1} + \pi b_{m_2}^2 h_{m_2}} \tag{5.58}$$

where h is the height of the cylindrical plume element as outlined in §5.3.3. Using these new "source" conditions, the merged plume is simulated for a further 10^3 spatial steps to produce Figure 5.13 which shows the different behaviour captured by this modification to the JETLAG model.

By using this modification to the JETLAG model, we are also able to extend this idea to N co-linear plumes. This extension uses the argument that, for N co-linear plumes, the two most upstream will merge, then this merged plume will merge with the next plume and so on, until only one plume, containing each of the original plumes, remains.

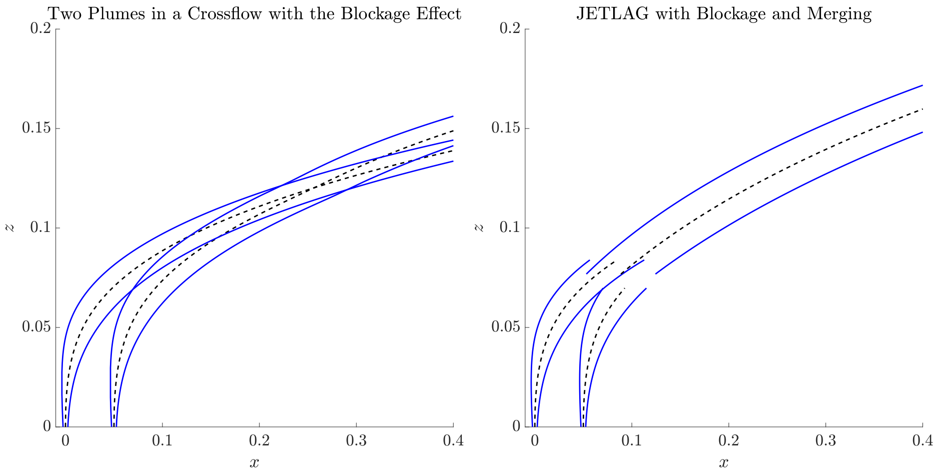

FIGURE 5.13: Figure comparing the trajectories and radii of two plumes subject to the blockage effect. If the plumes are allowed to follow the original model, the left plot is produced. The right plot is produced when the plumes are forced to remain merged once they've sufficiently merged to be thought of as behaving like a single plume.

5.5 Conclusion

In this chapter, we have developed a model for plumes in a cross-flow including, in particular, the phenomenon known as the blockage effect - where the upstream plumes shield the downstream plumes. Three existing models for plumes in a cross-flow, the model devised by Hoult *et al.* [79], the model devised by Lai, and JETLAG were investigated. The JETLAG model captured the behaviour of a plume in a cross-flow and could naturally be extended to implement the blockage effect. Therefore, the existing JETLAG model was extended to include my own model of the blockage effect. By simulating this extended model, the physical behaviour was captured in simulations of 2, 4 and 8 plumes in a cross-flow. The model outputs for 2 plumes will be compared to experimental data in §6.

Chapter 6

Plumes in a Cross-Flow: Experiments

6.1 Introduction

The modelling presented in §5 captured the behaviour of co-linear plumes in a cross-flow. This was done using a modification of the JETLAG model [37]. In this chapter, the model is validated experimentally. Specifically, experimental data is acquired to describe the trajectories of these plumes in a cross-flow. These trajectories are then compared to those predicted by the modelling in §5. Furthermore, from these trajectories, the experimental merging distance is found and again compared to the merging distance predicted by the previous modelling.

6.2 Methodology

6.2.1 Experimental Setup

The experiments to generate plumes in a cross-flow were set up according to Figure 6.1. A $5\,\mathrm{m} \times 0.60\,\mathrm{m} \times 0.60\,\mathrm{m}$ flume, in a laboratory at $21\,^{\circ}\mathrm{C}$, was filled with freshwater of density $\rho = 1000\,\mathrm{kg\,m^{-3}}$. This freshwater was the ambient environment. The fluid used to create the plumes was a saline solution of density $\rho = 1033\,\mathrm{kg\,m^{-3}}$. Both of these densities were measured using a sodium chloride refractometer. The saline solution was created using 20 litres of freshwater thoroughly mixed with 1.03 kg of sodium chloride. The plumes were visualised using 3 grams of E151 brilliant black dye mixed with 0.3 grams of yellow tartrazine dye.

The footage was collected at 30 frames per second using a manta camera with a 25 mm lens. A uniform light sheet was placed to backlight the region where the plumes would enter the flume. All windows were covered and any other artificial light sources were removed from the laboratory to minimise the noise introduced into the data. As discussed in §4.5.1, custom plume nozzles were used to ensure that each plume was fully turbulent. The design of these nozzles is given in Figure 4.9, based on the design of Dr Paul Cooper, Department of Mechanical Engineering, University of Wollongong, NSW, Australia.

We performed experiments using one, two and three plumes in a line at various source separations and cross-flow rates. Each plume had the same strength and all plumes were separated by the same distance from their nearest neighbour(s). To ensure that the cross-flow was constant, the flume was turned on and set to the desired cross-flow velocity and left to run for 30 minutes before the experiment. This was done to minimise any bursts of turbulence from air bubbles inside the engine that drove the water through the flume. We also ensured that the cross-flow was uniform by measuring the velocity in 3D using a *vectorino*, a velocity meter which measures in 3 dimensions, whenever the cross-flow velocity was changed. The experiment would only be performed if the vectorino found the cross-flow to be horizontal (parallel to the long edge of the flume) and uniform.

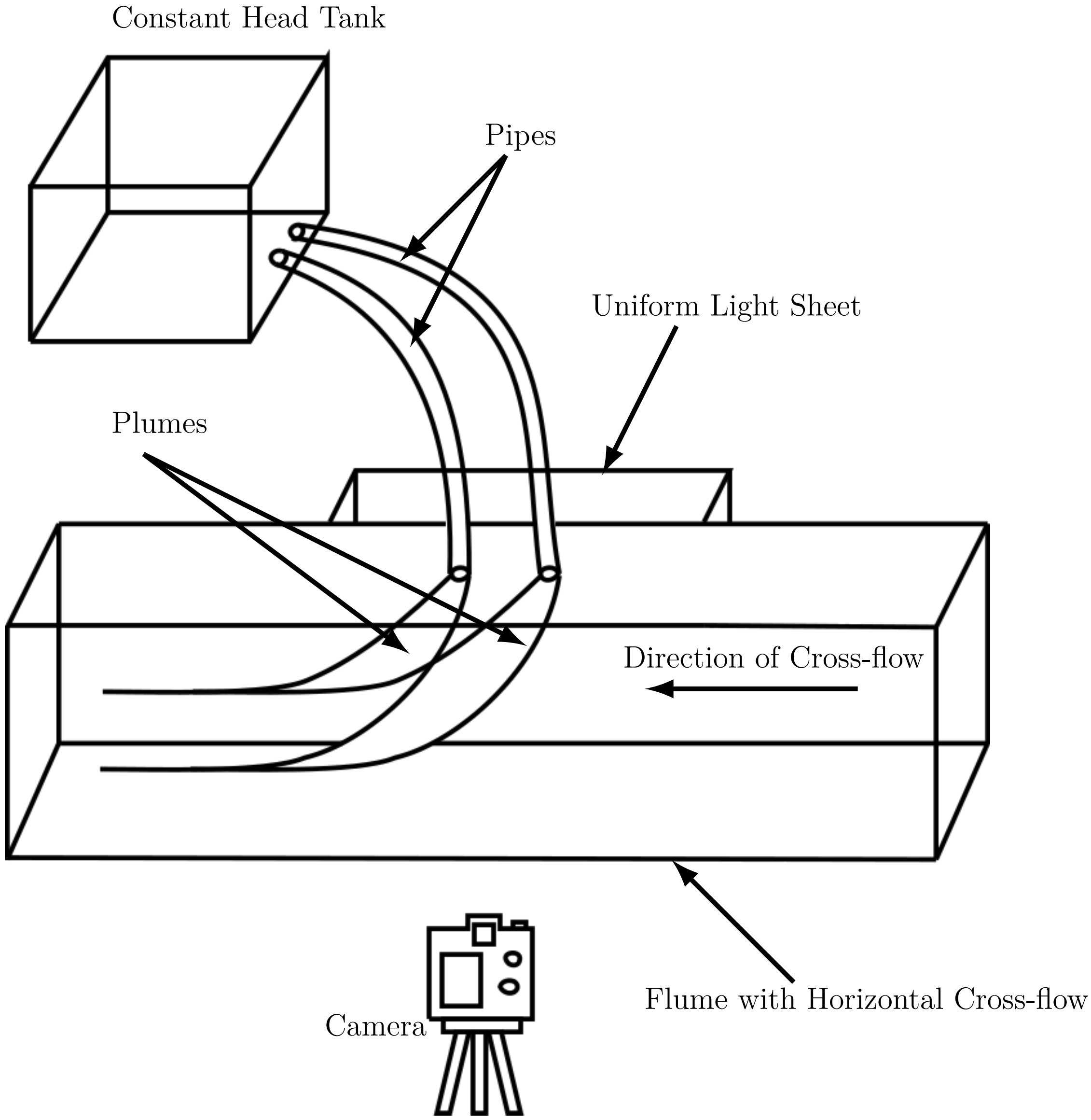

Figure 6.1: Experimental schematic of the cross-flow experiments, now with flow allowed.

6.2.2 Experimental Technique

The experiments in this chapter were conducted similarly to those in §4.5.2. The method is as follows:

1. Set the nozzle separation (for two or more nozzles).

2. Fill the flume with 0.6 m of freshwater and turn on the engine of the flume to create the desired cross-flow velocity. To ensure that the velocity is constant, based on preliminary experiments, the flume was allowed to run for 30 minutes before experiments were started.

3. Record 300 frames of background footage. This was used to remove the background from the plume imagery in the dye attenuation technique (given in Figure 4.10 and Figure 6.2).

4. Turn on all nozzles being used for this experiment and allow to run for 30 seconds. This allows the plume(s) to establish.

5. Begin recording the experiment and record for 90 seconds.

6. Stop recording, turn off all nozzles and drain the water from the flume.

7. Repeat steps 2 - 6 until five independent runs of the experiment are recorded at the current separation.

8. Increase the nozzle separation by 5 mm. Repeat this method until the configuration no longer merges in the region of the flume illuminated by the uniform light sheet.

Note that there are several key differences between this method and the method given in §4.5.2. The first is that we do not remove bubbles from the flume. This is because the fluid flows through the flume sufficiently quickly that bubbles were slow to form. Any bubbles that did form were washed downstream in the flume and therefore did not contaminate the experimental images. We were also able to record footage for significantly longer than in §4.5.2 because we did not encounter the "filling box problem". In the stillwater experiments, the dyed saline plumes would reach the bottom of the perspex tank and then cause a layer of dye to rise from the bottom of the tank which began to obscure the plume. As the flume had a flow and was removing the dyed fluid, this problem was not encountered. The above method was used for two and three plumes in a line with source separations ranging from 35 mm to 100 mm in a cross-flow of $0.014\,\mathrm{m\,s^{-1}}$. For a chosen separation, 60 mm, the cross-flow was also increased to $0.044\,\mathrm{m\,s^{-1}}$ and $0.084\,\mathrm{m\,s^{-1}}$.

6.3 Data Analysis

The aim of the experiments, outlined in §6.2.2, was to determine the behaviour of plumes in a cross-flow. In §5, we consider the behaviour of steady plumes in a cross-flow, therefore, we extract a time-average of each experiment using the dye attenuation technique as shown in Figure 4.10 and Figure 6.3. Once this steady plume image has been extracted, there are two quantities of particular interest - the centreline trajectories of the plumes, and the so-called merging distance. The merging distance is analogous to the merging height from §3 - §4. It is the curved distance from the source of the plumes to the point at which they merge and can be thought of as behaving like a single plume. Before attempting to compute the merging point, and thereby the merging distance, we must first find the centreline trajectories of the plumes.

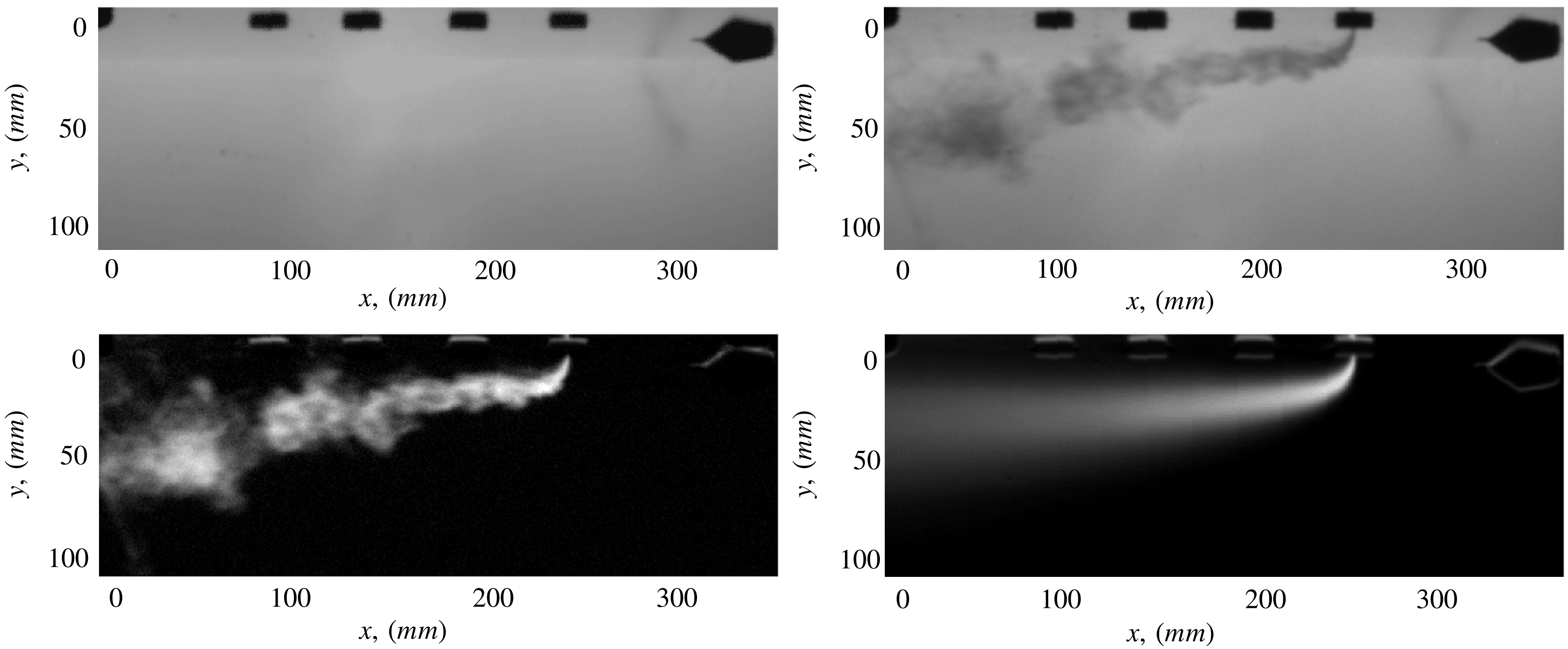

Figure 6.2: Schematic of the dye attenuation technique. The background image (top left) is removed from each frame of the video (top right) to give frames without background noise (bottom left) which are then time-averaged to give a steady plume (bottom right). This experiment was performed with a cross-flow velocity of $0.014\,\mathrm{m\,s^{-1}}$.

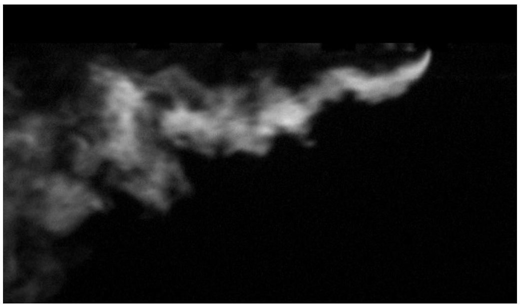

(a) Single frame from one nozzle cross-flow experiment.

(b) Time-averaged data from one nozzle cross-flow experiment.

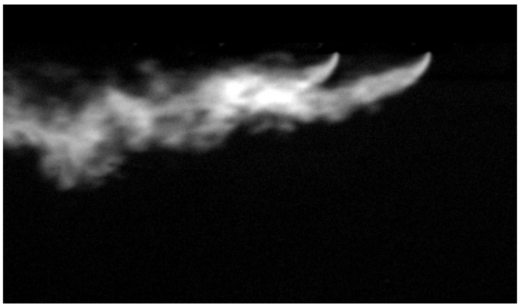

(c) Single frame from two nozzle cross-flow experiment.

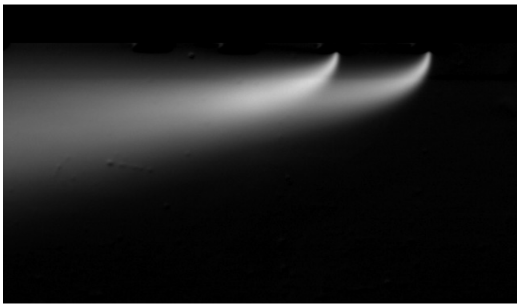

(d) Time-averaged data from two nozzle cross-flow experiment.

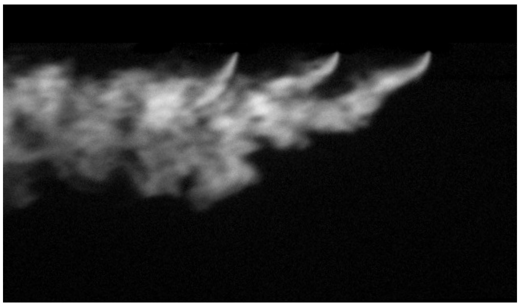

(e) Single frame from three nozzle cross-flow experiment.

(f) Time-averaged data from three nozzle cross-flow experiment.

FIGURE 6.3: Sample outputs from the cross-flow experiments, after the background has been subtracted and the time-average taken (where relevant). Axes are the same as in Figure 6.2.

6.3.1 Extracting Plume Trajectories

To extract the trajectories of the plumes found experimentally, a two dimensional peak search was used. For an initial iteration, we began by scanning top to bottom along the experimental image, and extracted the pixel intensity from each row of pixels in the image and fit an N-peaked Gaussian to this data, where N is the number of plume nozzles used. This method breaks down when the plumes are sufficiently far from vertical. Once the cross-flow has advected the plumes off-vertical, we repeat the same method but scanning left to right, and extracting columns of pixels instead of rows. This method now breaks down when the plumes are sufficiently off horizontal. A linear interpolant is used in the region where neither of the above searches are valid, thereby completing the initial iteration. Using MATLAB's "findpeaks" function, we determine the number of peaks in each of these fitted Gaussians. The locations of these peaks are used to approximate the plume trajectory. In the top-to-bottom search, we find the buoyancy dominated trajectories of the plumes and in the left-to-right search, we find the momentum dominated trajectories. Note that there is an intermediate region where these scans do not detect the correct number of peaks as we haven't extracted an angled plane of pixels, instead only rows or columns. In order to complete the initial iteration, we linearly interpolate this intermediate region, using the partial trajectories as a guide. Once complete, we have the initial plume trajectories.

For subsequent iterations, the following method was used:

1. Set $k = 1$, where k is the index of the current position on the plume trajectory, and extract the k^{th} entries in the previous trajectories. This will return N points.

2. Compute the best fitting linear interpolant through these N points

3. Extract the pixel data along this line. Note that this line extends to infinity, but we restrict this to only the image region. That is, the line is restricted to the region that overlaps the image.

4. Fit an N-peaked Gaussian to this extracted data and find the peaks.

5. Add the locations of these peaks to the current trajectory.

6. Update k to $k + 1$.

7. Iterate until k equals the number of points in the previous trajectory.

This algorithm is given schematically in Figure 6.4 where the circular points denote example points on the centreline of the plume, the orange line denotes the line segment between consecutive centreline points, the green curves are the Gaussians fitted to the light intensity extracted along the line normal to the orange line segment. The peaks of these Gaussians are those added to the trajectory as given in step 5 of the algorithm. This method is then iterated until the two-norm between successive trajectories is sufficiently small. That is,

$$\sqrt{(x_{\text{current}} - x_{\text{previous}})^2 + (z_{\text{current}} - z_{\text{previous}})^2} < \epsilon \tag{6.1}$$

for some tolerance, ϵ. Once this measure is less than ϵ, we say that we have iteratively converged to the experimental trajectories of the plumes. An example of these converged trajectories is given in Figure 6.5. The cyan trajectory is the midpoint of the white and black, which are the trajectories of the two plumes. Note that the white and cyan trajectories disappear under the black, which shows that after this point, there is only one identifiable peak in the two-peaked Gaussian which suggests that the two plumes have merged into one plume - which will have the trajectory given by the black centreline. Once the trajectories have been extracted, we are able to use them to determine the merging point.

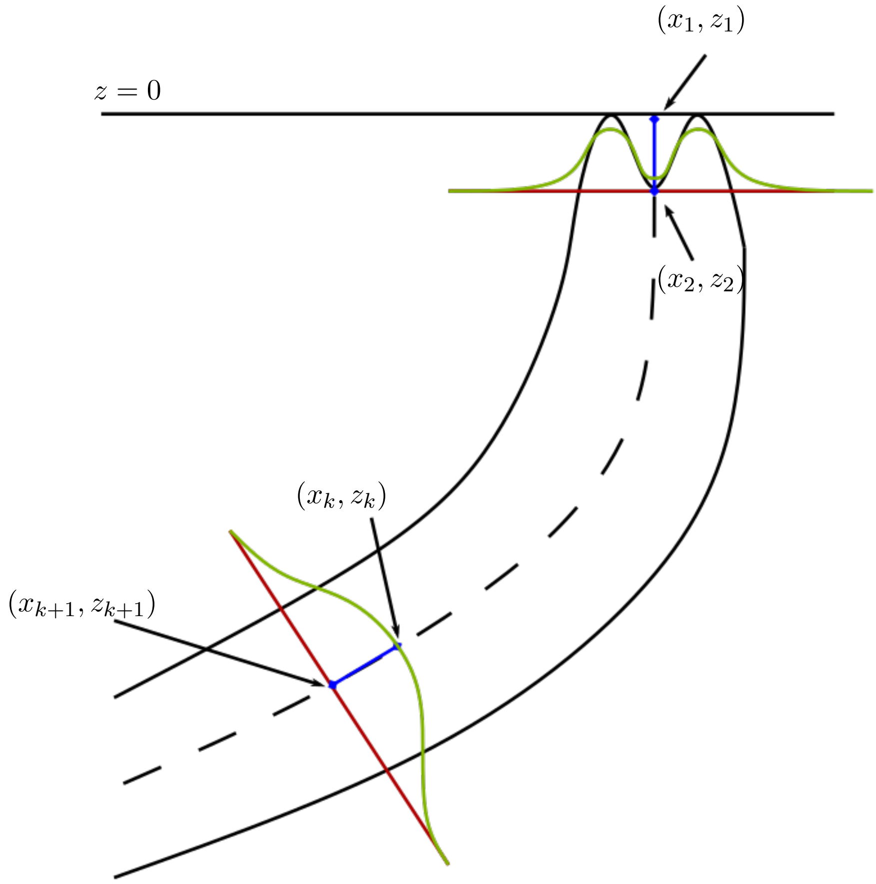

Figure 6.4: Schematic of the algorithm to extract plume trajectories. The blue line shows individual line segments connecting consecutive points (shown by blue squares) on the dashed, midline curve. The normal to these line segments are given in red. Pixel data is extracted along the red line, and a Gaussian fitted to this pixel data. This Gaussian is shown in green.

6.3.2 Finding the Merging Point

In order to determine the merging point, we require the midpoint trajectory - an example of which is given in cyan in Figure 6.5. The trajectory is discrete, and contains K points. Beginning from the source ($k = 1$), we compute the normal to the line connecting the k^{th} and $(k+1)^{\text{th}}$ points on the trajectory. The pixel data along this normal line is extracted, and an

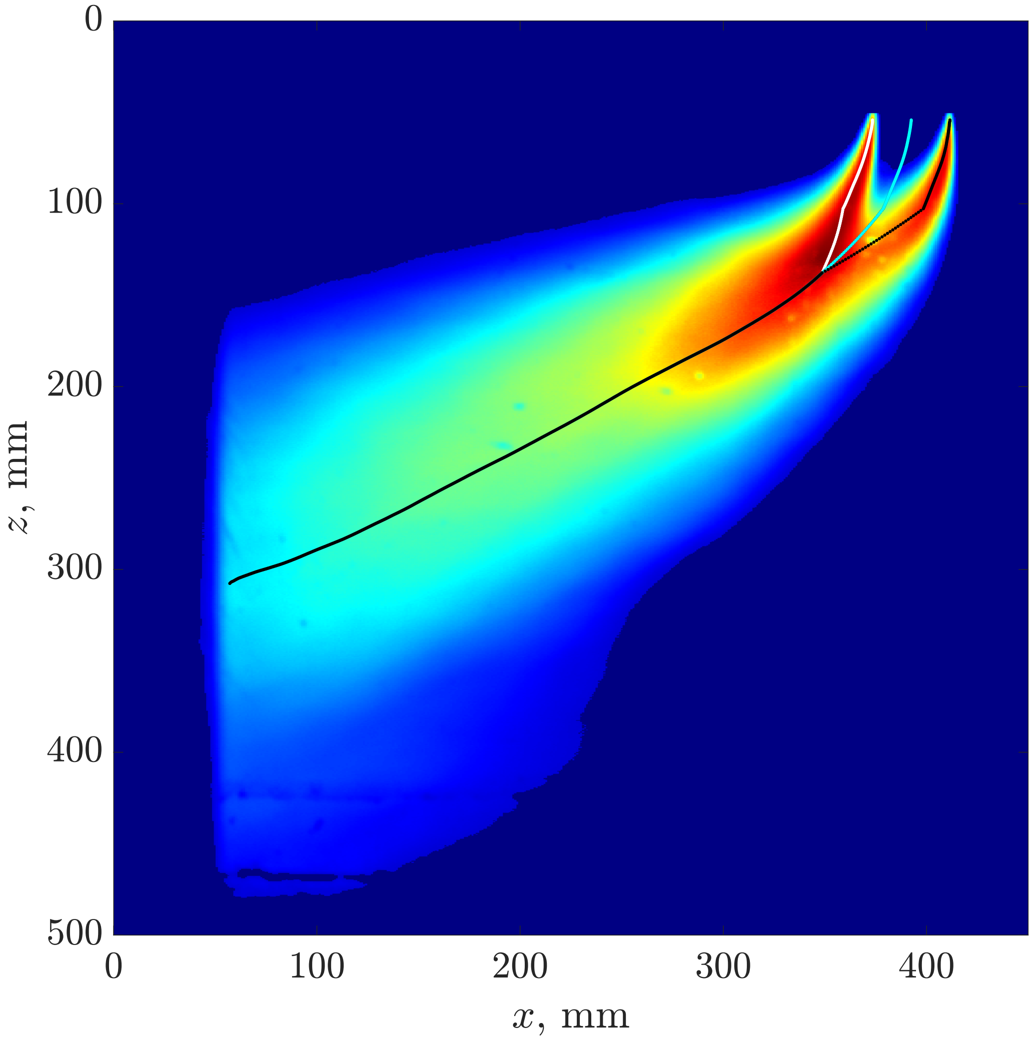

Figure 6.5: Figure showing the experimentally determined trajectories of two plumes, separated by a distance 35 mm, in a cross-flow with velocity $0.014\,\mathrm{m\,s^{-1}}$.

N-peaked Gaussian is fitted to this data. The merging point is defined as the first point along the midpoint trajectory where there is a single peak in the N-peaked Gaussian. An example of the merging point is given in Figure 6.6 for two plumes, with a source separation of 35 mm, and in a 0.014 m s^{-1} cross-flow. The black square denotes the first point, scanning from the source down (approximately top to left in Figure 6.6) at which we find one peak instead of two.

We performed this method on each independent experiment, and on the ensemble average of each separation distance (i.e. the ensemble average of the accumulated data from the five experiments performed at 35 mm separation). Doing so, we determined the merging point of each experiment. This was done for both the two and three plume experiments. Finally, we use this merging point to determine the merging distance for each experiment.

6.3.2.1 Finding the Merging Distance

The merging distance is analogous to the merging height from §3 - §4. We define it as the distance from the source of the midpoint trajectory to the merging point, found in Figure 6.3.2. To determine this distance, we computed the Euclidean distance between each successive pixel on the midpoint trajectory, and sum these. This gives an approximation to the merging distance using piecewise Euclidean distance. Explicitly, we have

$$s_m = \sum_{k=1}^{k=K_m-1} \sqrt{(x_k - x_{k+1})^2 + (z_k - z_{k+1})^2} \tag{6.2}$$

where K_m is the index of the merging point and s_m denotes the merging distance. Performing this method for each experiment and the ensemble average, we are able to determine the merging distance for two and three plumes in a given cross-flow as a function of the source separation.

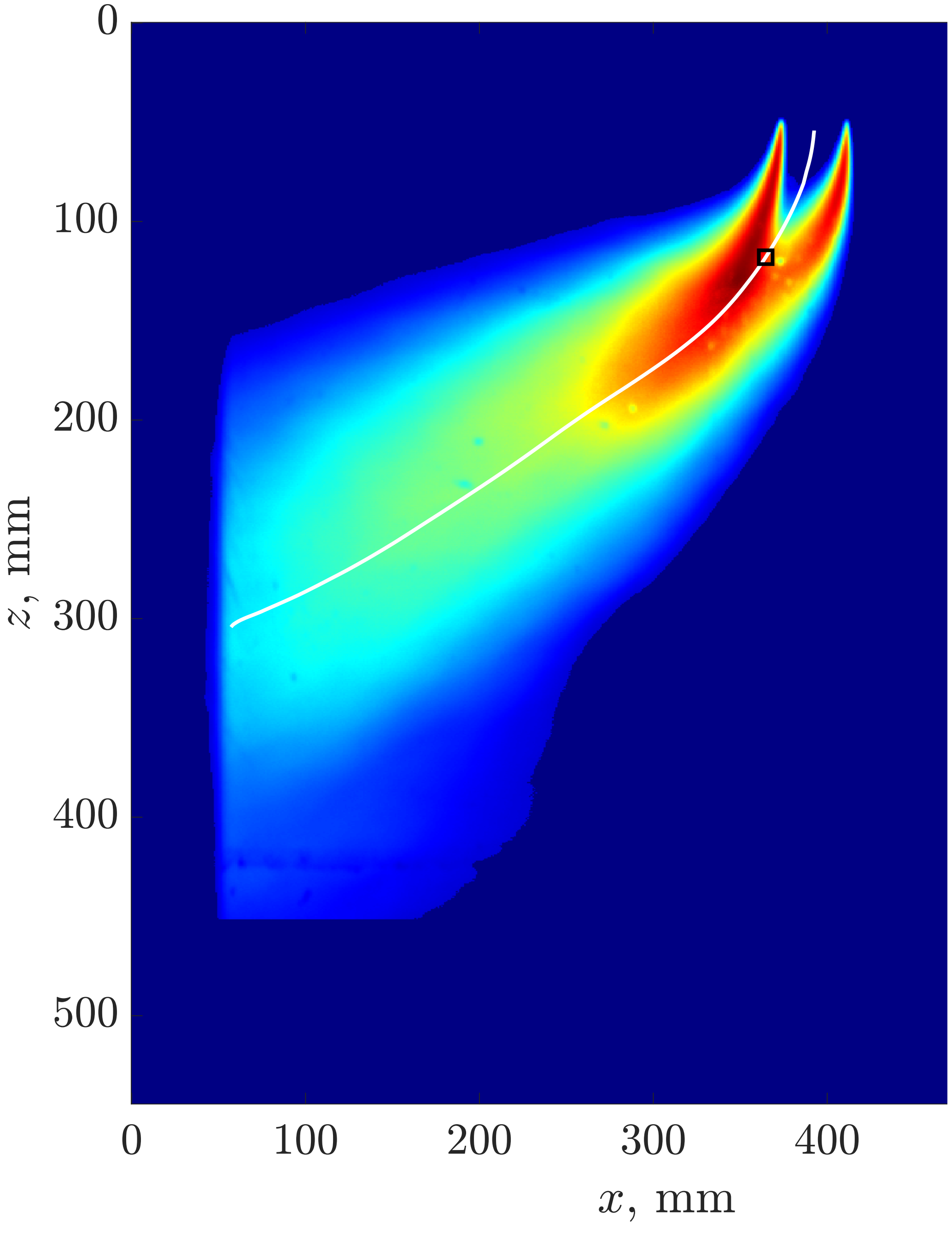

Figure 6.6: Figure showing the experimental midpoint centreline (white) and the merging point (black).

6.4 Results

By performing the analysis outlined in §6.3.2.1, we produce Figure 6.7 to show the merging distance of two plumes in a cross-flow of $0.014\,\mathrm{m\,s^{-1}}$, as a function of source separation. As in §4.6, this data is compared to a straight line through the origin, $s_m = \lambda_m \chi_0$, where λ_m denotes the non-dimensional merging distance and χ_0 the source separation between the plumes. Fitting this model to the experimental data using MATLAB's "fitnlm" function, which uses an iterative, non-linear least squares estimation, gives the solid line in Figure 6.7. The error bars are computed by taking the standard deviation of the merging distances found in the independent experiments, whereas the value shown by the squares is the merging distance found using the ensemble average of these experiments.

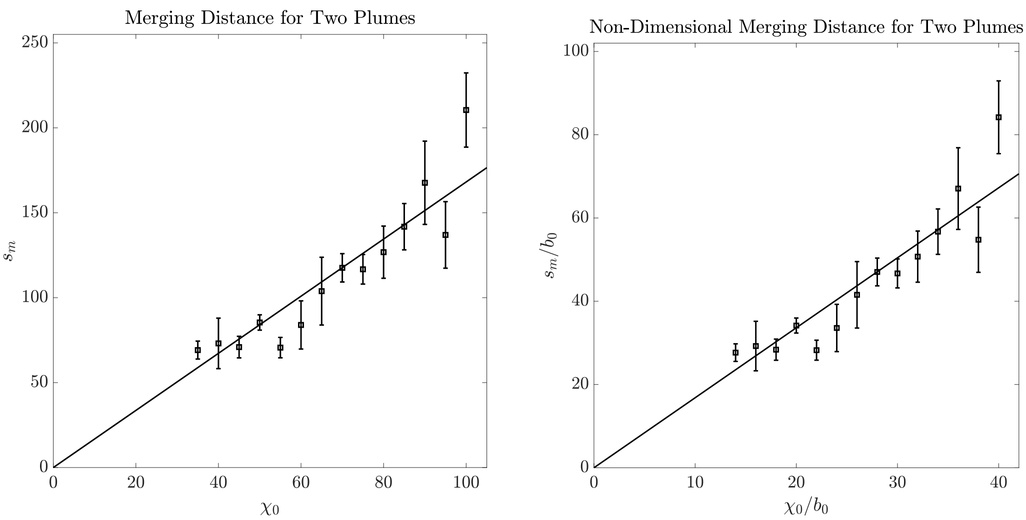

FIGURE 6.7: Plot of the merging distance, s_m, of two plumes in a cross-flow of $0.014\,\mathrm{m\,s^{-1}}$, as a function of source separation (left) and the same merging distance non-dimensionalised by the source radius of the plume nozzle, 2.5 mm.

Using an r^2 correlation coefficient, we see that the experimental data for two plumes in a cross-flow is well approximated by the straight line through the origin. Direct comparison between model and experiments gives $r^2 = 0.84$, implying strong correlation between model estimates and experimental data.

However, when repeating this method for three plumes in the same cross-flow, we obtain a noticeably poorer fit as shown in Figure 6.8, resulting in an r^2 of 0.59. Note that there is significantly less data for the three plume experiments due to the length of the uniform light sheet. That is, the plumes were advected outside of the range of the light sheet after separation distances of 70 mm. This r^2 value still suggests a strong positive correlation between experimental data and the straight line through the origin, but not to the extent of the two plume experimental data. There are numerous ways to account for this difference in the three plume case. The most likely reason is that the third plume adds an additional layer of plume-to-plume interaction which, when combined with the interaction between the cross-flow and the plumes themselves, causes the merging distance of the line of plumes to deviate from the predicted linear relationship.

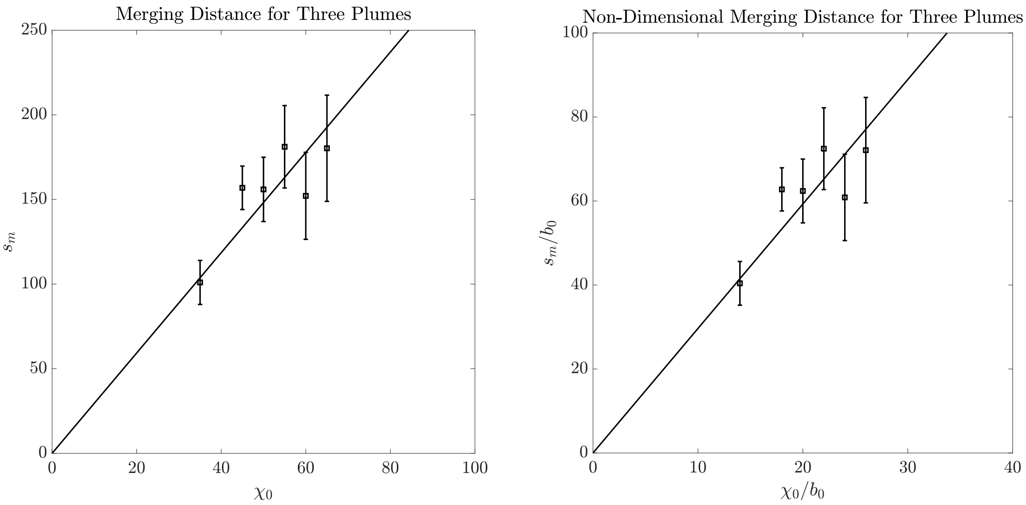

Figure 6.8: Plot of the merging distance, s_m, of three plumes in a cross-flow of $0.014\,\mathrm{m\,s^{-1}}$, as a function of source separation (left) and the same merging distance non-dimensionalised by the source radius of the plume nozzle, 2.5 mm. Note that the 40 mm separation experiment has been removed from the data set as it was determined to be an outlier.

Using an identical method of analysis, we determine the merging distance for lines of plumes with a source separation of 60 mm as a function of cross-flow velocity. Due to experimental limitations - namely the minimum flow rate of the flume and the maximum flow rate before the plumes were entirely

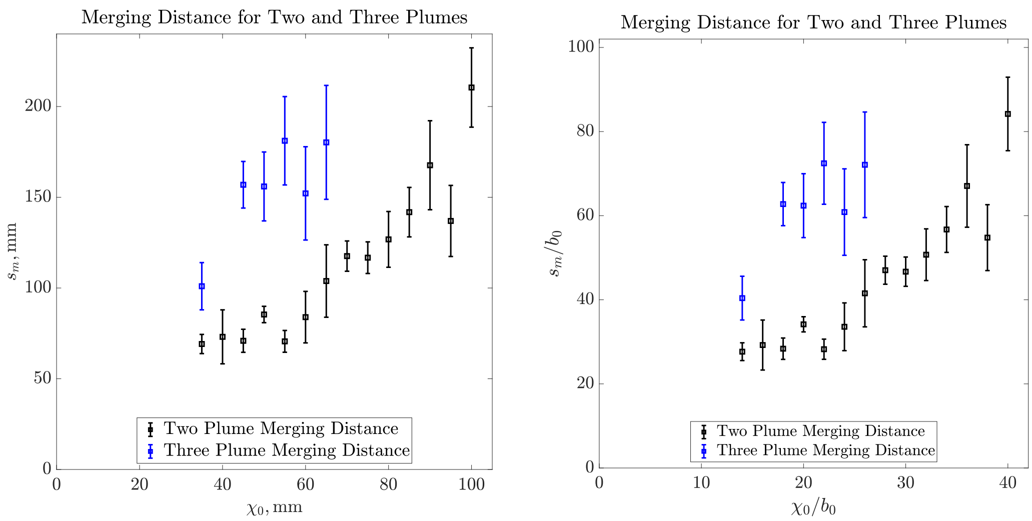

FIGURE 6.9: Plot of the merging distance of two and three plumes in a cross-flow of $0.014\,\mathrm{m\,s^{-1}}$, as a function of source separation (left) and the same merging distance non-dimensionalised by the source radius of the plume nozzle, 2.5 mm.

sheared off by the flow - we were only able to complete this experiment for three flow rates. These were $0.014\,\mathrm{m\,s^{-1}}$, $0.044\,\mathrm{m\,s^{-1}}$ and $0.084\,\mathrm{m\,s^{-1}}$. Taking flows slower than this would cause the engine of the flume to stall and create a non-constant and non-uniform flow in the flume. Any faster flows would cause the plumes to be sheared off before they could sufficiently form, and certainly before any chance of merging. This data is shown in Figure 6.10 and Figure 6.11. We note that the merging distance, s_m, is non-dimensionalised by the nozzle radius $b_0 = 2.5\,\mathrm{mm}$, and the cross-flow velocity, U_a, is non-dimensionalised by the source velocity $w_0 = 0.33\,\mathrm{m\,s^{-1}}$.

6.5 Comparison to Modified JETLAG

6.5.1 Comparison of Trajectories

In this section, we compare the plume trajectories predicted by JETLAG to the plume trajectories found experimentally. We also compare the merging distances found experimentally with those extracted from the JETLAG model. The parameters used in the JETLAG model are the same as the

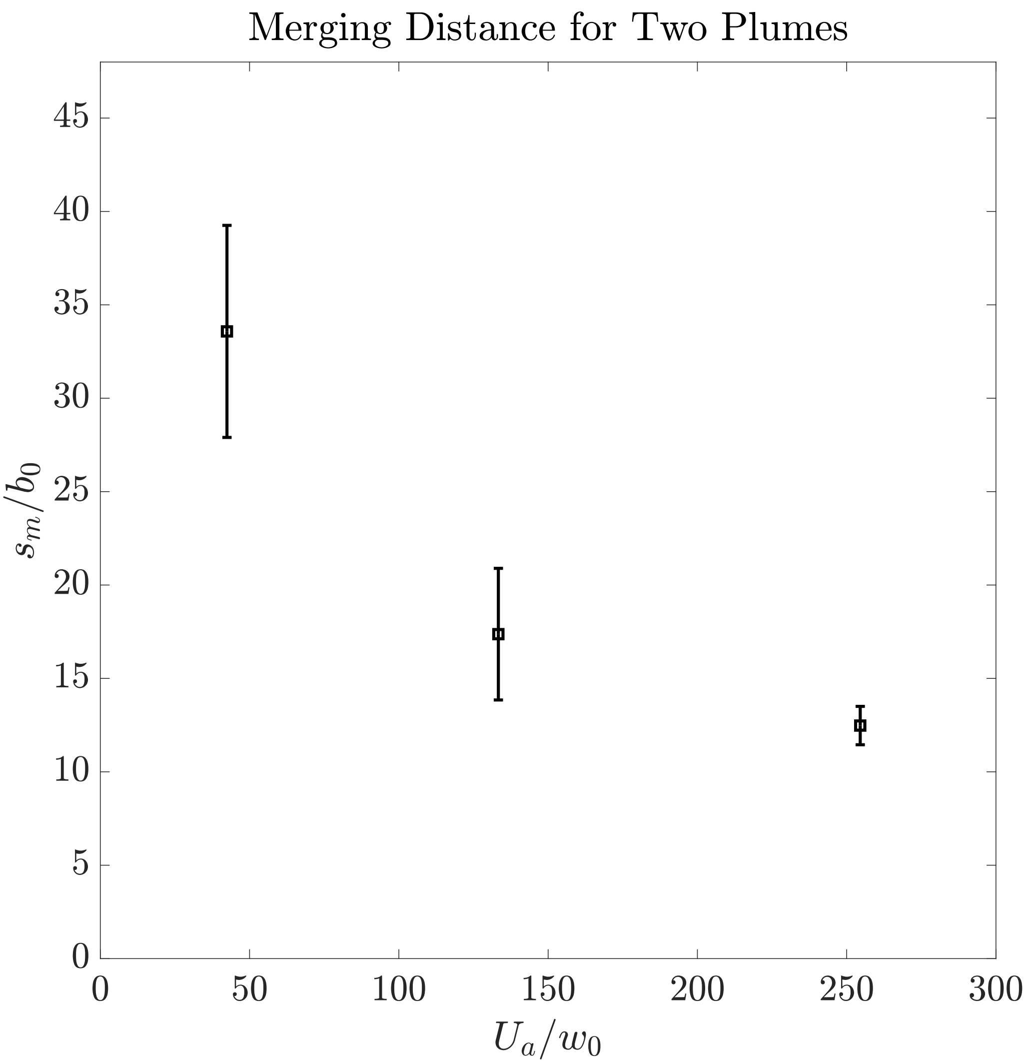

Figure 6.10: Plot showing the merging distance of two plumes in cross-flows of $0.014\,\mathrm{m\,s^{-1}}$, $0.044\,\mathrm{m\,s^{-1}}$ and $0.084\,\mathrm{m\,s^{-1}}$.

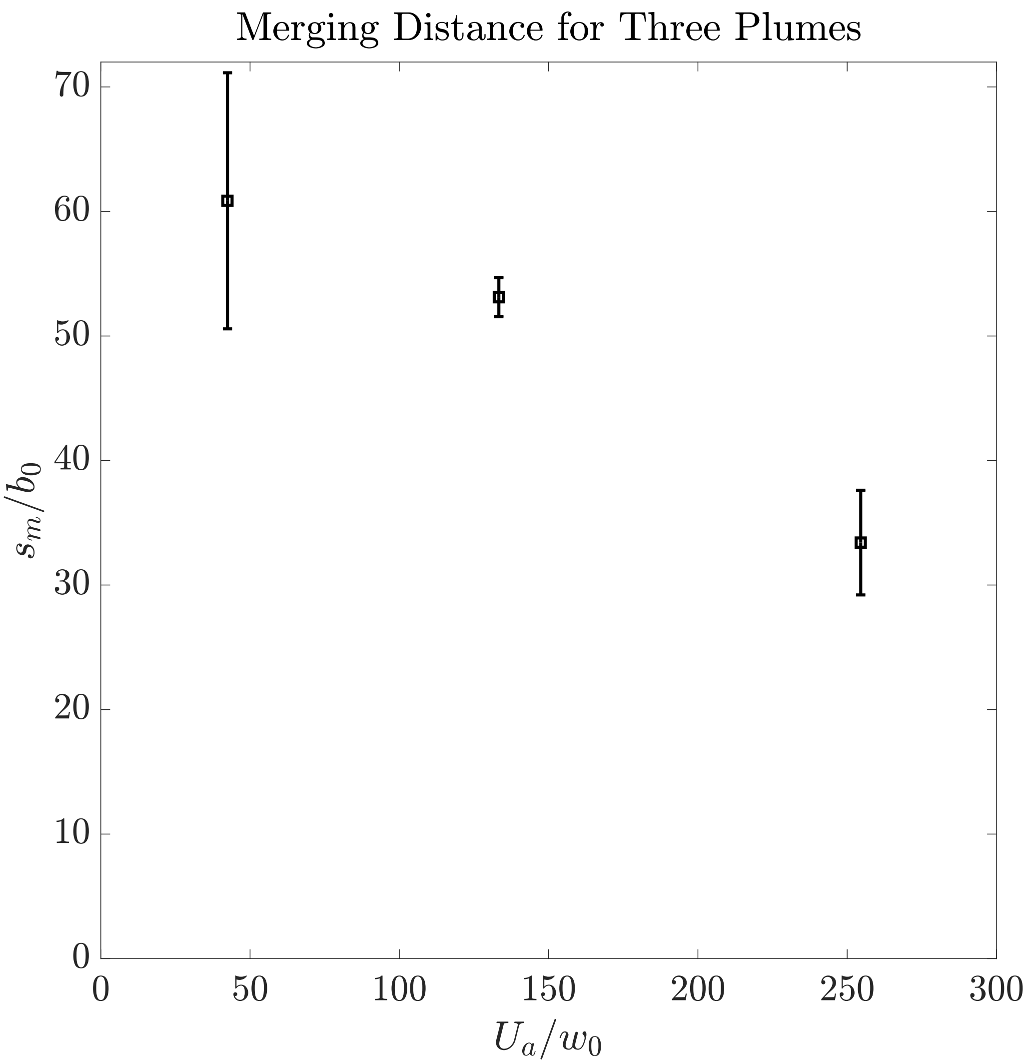

Figure 6.11: Plot showing the merging distance of three plumes in cross-flows of $0.014\,\mathrm{m\,s^{-1}}$, $0.044\,\mathrm{m\,s^{-1}}$ and $0.084\,\mathrm{m\,s^{-1}}$.

experimental quantities used in §6.4 and are given in Table 6.1. It is important to note that the values of ρ_0 and ρ_a are chosen such that $\Delta\rho$ is the same as in the experiments performed in this chapter because the experiments are upside down compared to the corresponding JETLAG simulations.

Parameter	Value
U_a	$0.014\,\mathrm{m\,s^{-1}}$
V_0	$0.088\,\mathrm{m\,s^{-1}}$
ρ_0	$967\,\mathrm{kg\,m^{-3}}$
ρ_a	$1000\,\mathrm{kg\,m^{-3}}$
b_0	$2.5 \times 10^{-3}\,\mathrm{m}$

Table 6.1: Table of initial conditions used to compare trajectories found experimentally and with the JETLAG model.

We compare trajectories between experiments with source separation distances of $\chi_0 = 50\,\mathrm{mm}$ and $70\,\mathrm{mm}$. The trajectories in question are plotted in Figures 6.12 and 6.13. In these figures, if the experimental centrelines were indistinguishable, i.e. the plumes had fully merged, only the red trajectory, for the rightmost plume, will be present as the lines are plotted over one-another. This is especially prominent in Figure 6.12. By examining these figures one-by-one, we encounter several differences between the model trajectories and the experimental.

For the smallest separation in the sample images, specifically 50 mm, we see that the near-source region is well approximated, but the far field is a poor match to the experimental data. Experimentally, we see that the plume centrelines meet approximately two source separations from the midpoint of their origins, and are then indistinguishable by the algorithm given in §6.3.1. However, in the JETLAG model approximations, the centrelines cross approximately 2.5 source separations from the midpoint of their origins and then separate again. These trajectories are then a poor approximation for the experimental, merged centreline. This so-called separating behaviour can be explained by referring back to §5.4 and noting that the blockage effect is applied to only one plume. That is, the blockage effect model assumes that only the right plume (red) is shielded, and is so for the entire experiment. Whereas in practice, after the plume centrelines cross, the left plume (blue) is now experiencing the blockage effect - not the right plume - and therefore is undergoing behaviour not approximated in the JETLAG model. This behaviour is seen for greater source separations as well, but does not lead to as severe of a deviation from the experimental data. Furthermore, we note that the JETLAG model used for comparison assumes that there are two plumes, and is not expected to be valid for the merged trajectory/

At 70 mm separation, we find that the near-source region is again well approximated by the JETLAG model, albeit with some deviation in the experimental centreline caused by turbulence in the cross-flow. We also encounter the so-called separating behaviour mentioned previously, but for this source separation the left plume approximately follows the merged experimental centreline. As before, the rightmost plume from the model is considerably different from the merged centreline. This is explained by the same argument as the 50 mm separation.

6.5.2 Comparison of Merging Distances

Recall that, along with the trajectories of the plumes, there is particular interest in finding how far from their sources that they merge. This is the merging height in stillwater, and the merging distance in a cross-flow. In §6.3.2, a method for how to find the merging distance for plumes in a cross-flow from experimental data was given. This is now compared to the merging distance found from the modelling given in §5, using a nominally identical method.

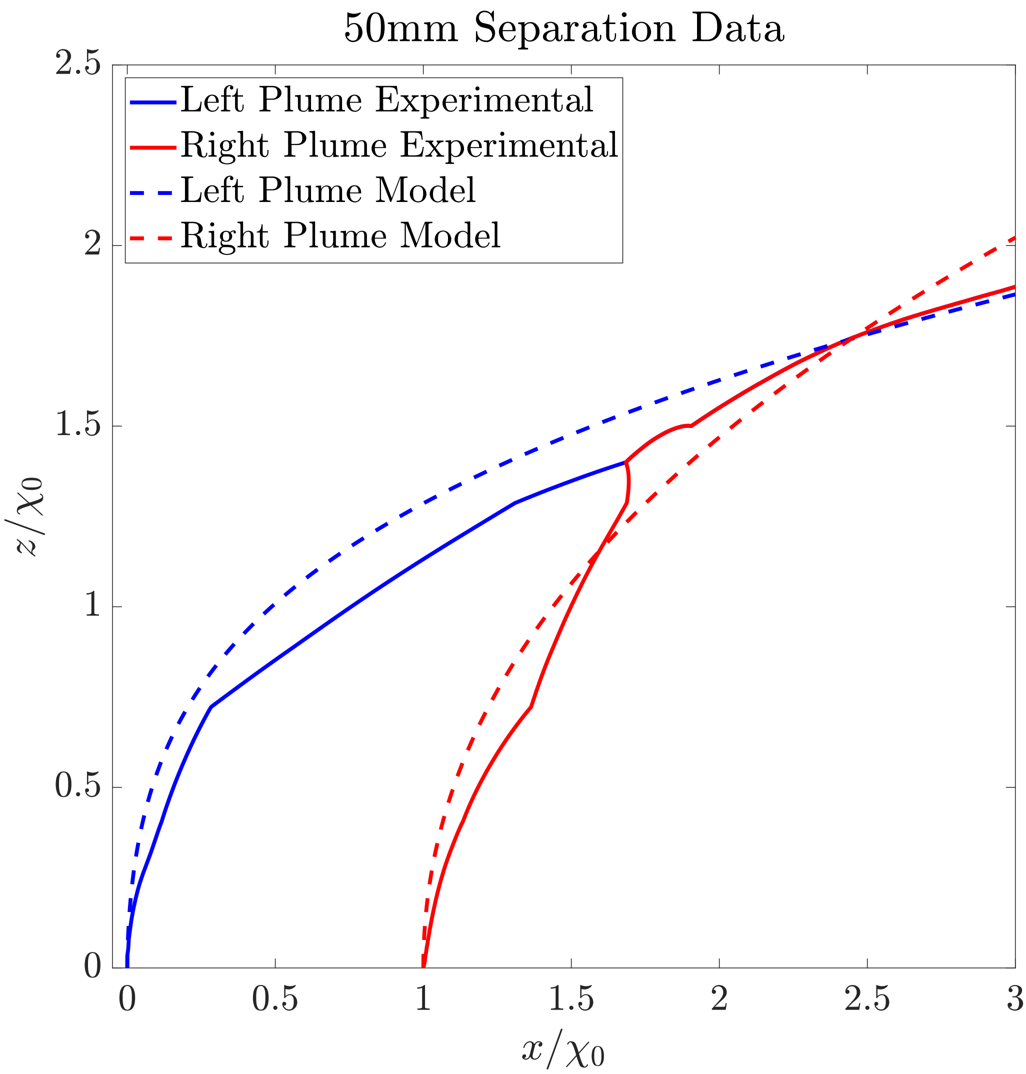

FIGURE 6.12: Comparison of trajectories found experimentally (solid) and with the JETLAG model (dashed) for 50mm source separation.

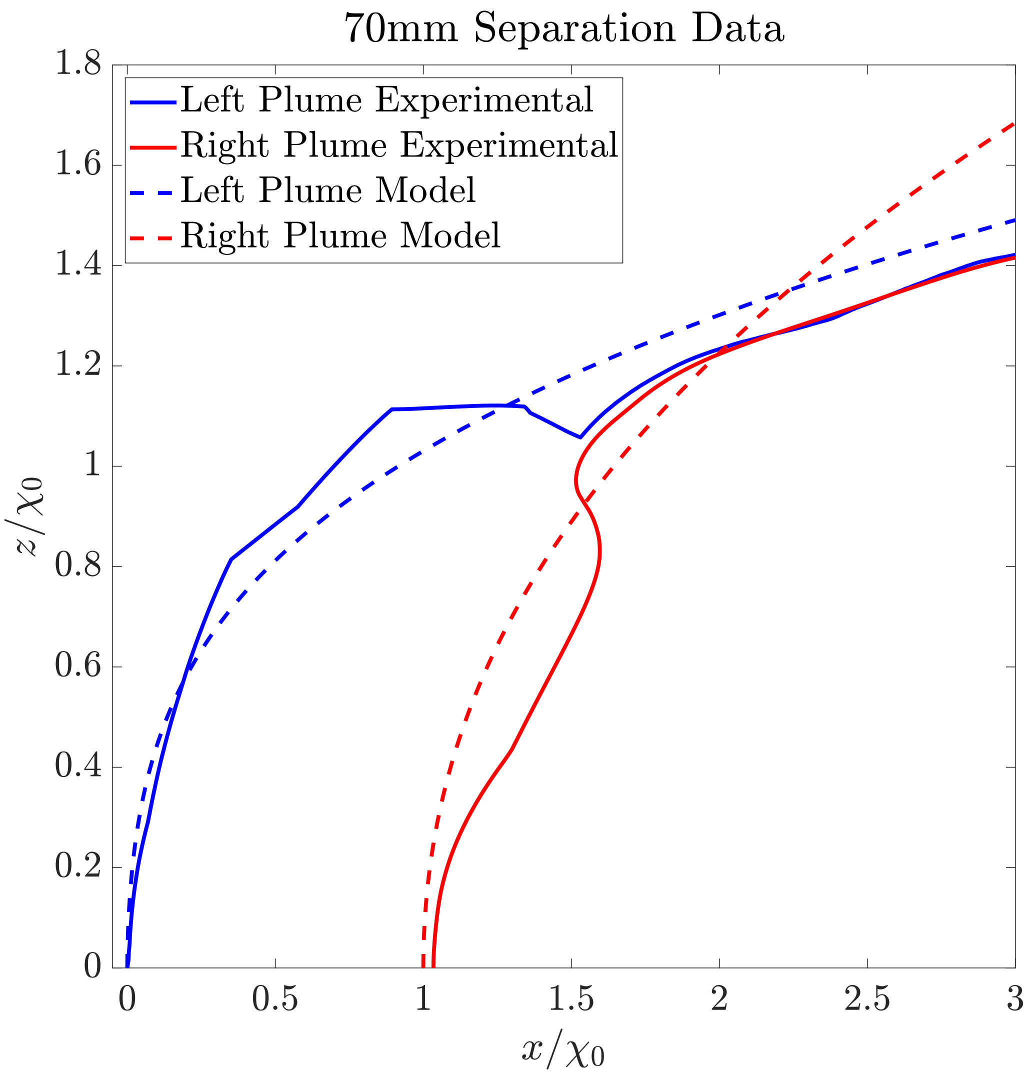

Figure 6.13: Comparison of trajectories found experimentally (solid) and with the JETLAG model (dashed) for 70mm source separation.

We first examine the behaviour of two plumes in the lowest flow used experimentally - $0.014\,\mathrm{m\,s^{-1}}$. By simulating the JETLAG model with the blockage effect, as outlined in §5, the plume trajectories are obtained for each experiment performed at this flow rate. By extracting the merging point and finding the merging distance, similarly to the method in §6.3.2, the data shown in Figure 6.14 is found. The data given in this figure show that the model and experimental merging distances exhibit the same trend, namely that they increase with the source separation. For small source separation distances, the model data and experimental data are in good agreement. However, for larger source separation distances (in this case 60 mm or greater), the model merging distance is significantly greater than the experimental merging distance. This discrepancy suggests that the blockage effect is underestimated for larger source separations.

To complete the comparison with the two plume experimental data, the merging distance from the modelling data is obtained at all flow rates used experimentally ($0.044\,\mathrm{m\,s^{-1}}$ and $0.084\,\mathrm{m\,s^{-1}}$). These are compared to the corresponding experimental merging distances in Figure 6.15. Here, it can be seen that for higher cross-flow velocities, the model and experimental data are in good agreement. However, for the lowest cross-flow, there is a significant difference between the model and experiments. This is consistent with the observation that the blockage effect is underestimated for larger source separations at a flow velocity of $0.014\,\mathrm{m\,s^{-1}}$. For greater velocities, the blockage effect appears to be well approximated by the modelling of §5. Similarly, the merging distances for three plumes at the source separations that correspond to the experimental data from this chapter are computed. The three plume modelling is seen to be in poorer agreement with experimental data, consistently underestimates the merging distances for the separation distances chosen. However, as the separation distance increases, the experimental merging distance is seen to be a noticeably

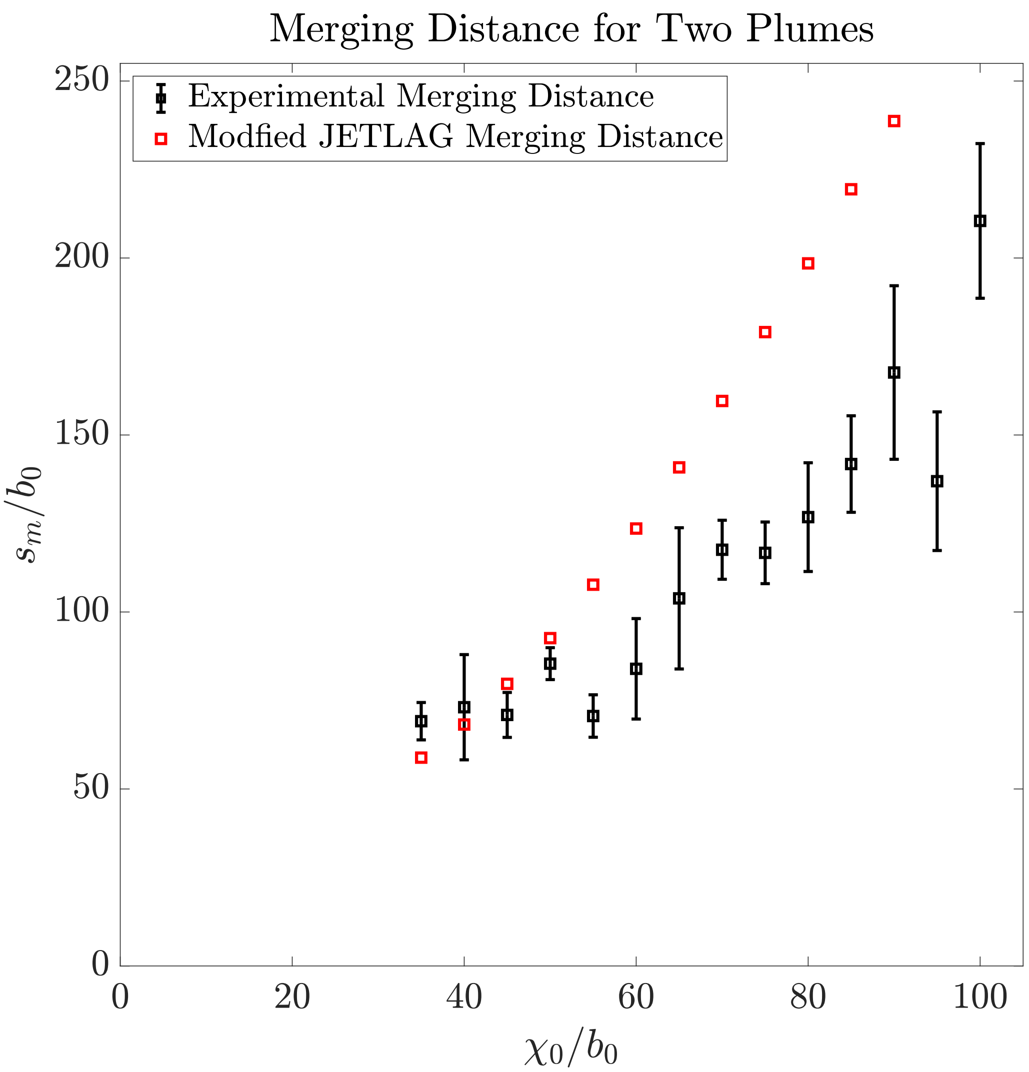

FIGURE 6.14: Plot showing the experimental and model merging heights for two plumes in a cross-flow of $0.014\,\mathrm{m\,s^{-1}}$.

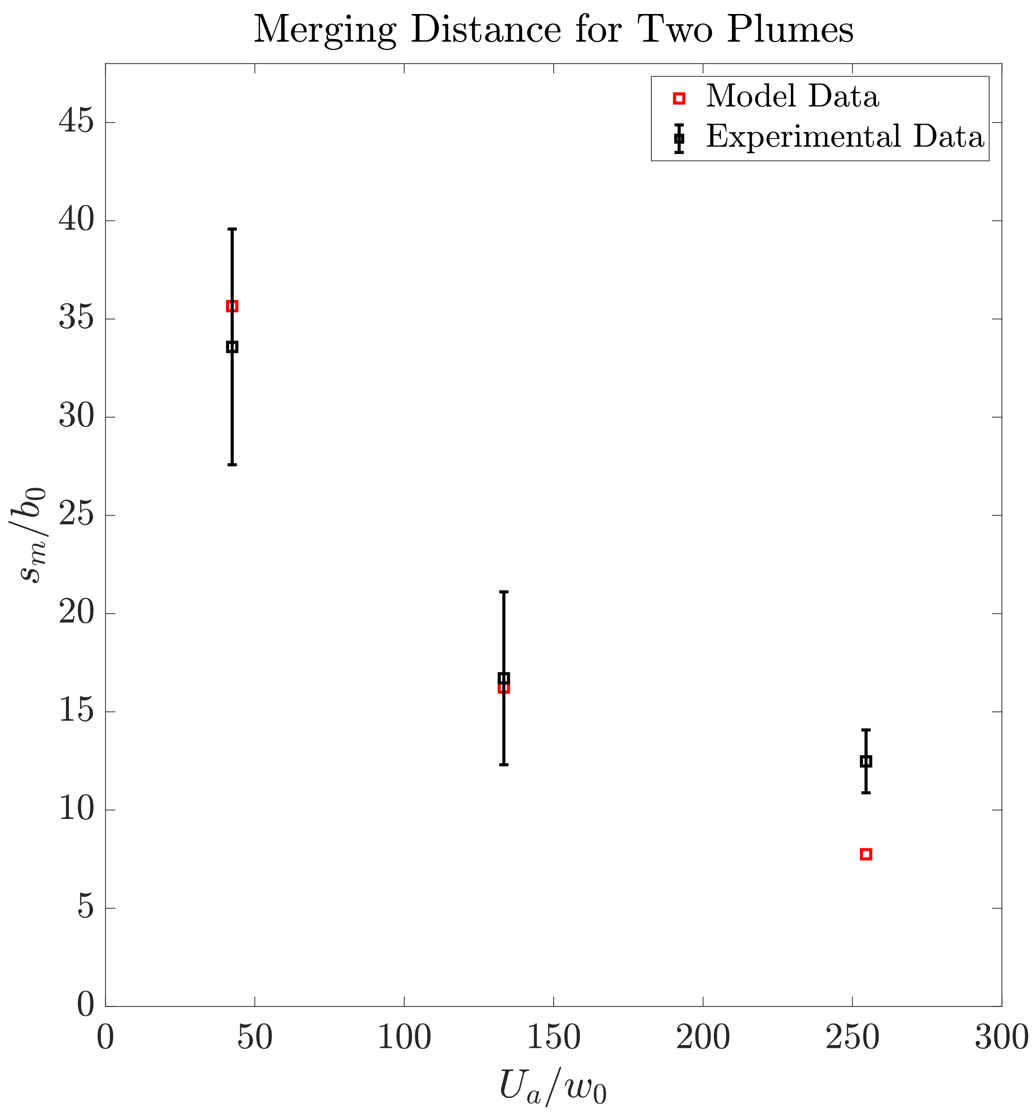

Figure 6.15: Plot showing the model merging distances of two plumes in cross-flows of $0.014\,\mathrm{m\,s^{-1}}$, $0.044\,\mathrm{m\,s^{-1}}$ and $0.084\,\mathrm{m\,s^{-1}}$ compared to the corresponding experimental data.

better fit to the model data. Indeed, it is seen in Figure 6.16 that the model data does not increase linearly with source separation, instead being proportional to the square of source separation.

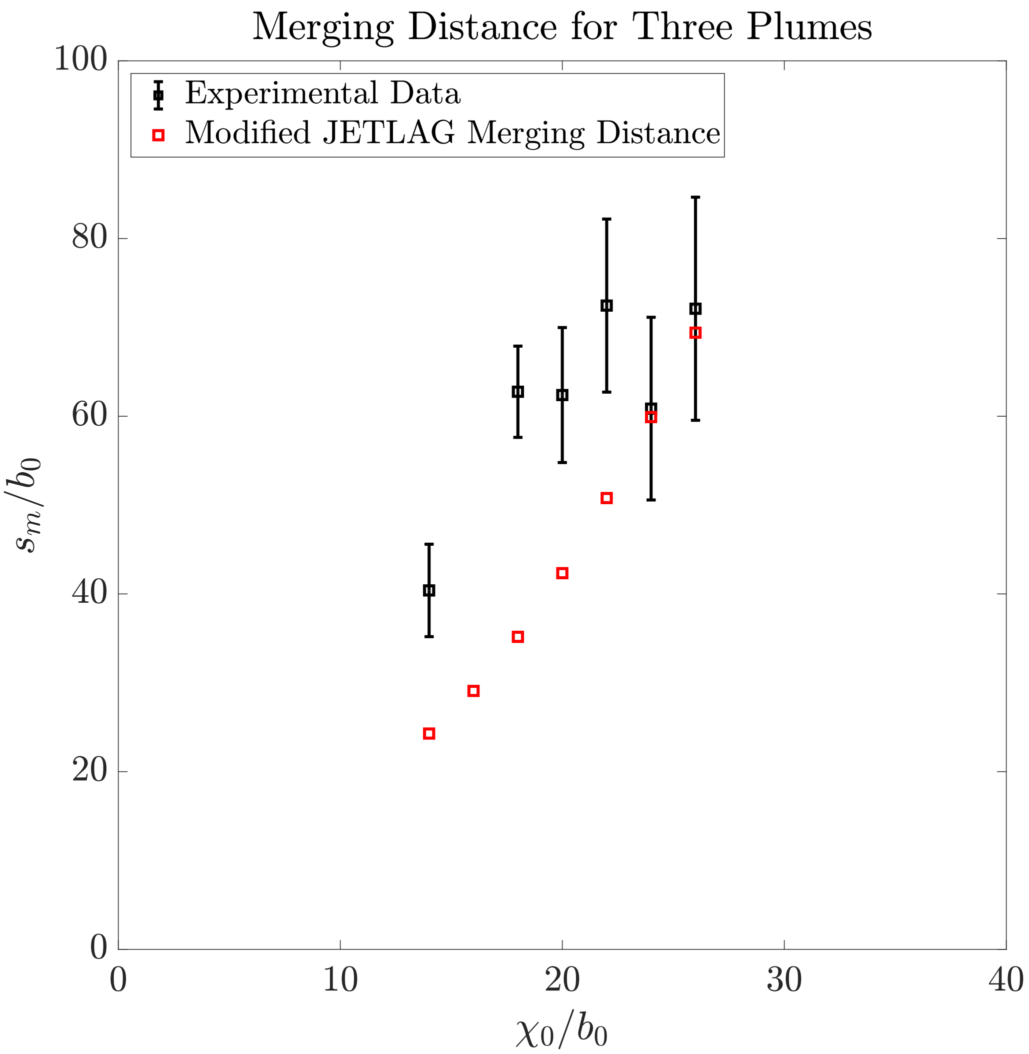

Figure 6.16: Plot showing the experimental and model merging heights for three plumes in a cross-flow of $0.014\,\mathrm{m\,s^{-1}}$.

6.6 Conclusion

This chapter has concentrated on determining the experimental merging distance for plumes in a cross-flow. The experimental data required to do so was obtained using flume experiments as outlined in §6.2. The trajectories of these experimental plumes were extracted and compared to model trajectories obtained in §5.

These experimental plume trajectories were seen to be in good agreement with those obtained from the mathematical model, and noticeably improved as the separation distance increased. This is because the mathematical model used was adapted from a model intended for non-interacting plumes, and the greater the separation distance between these plumes, the closer their behaviour is to that of independent, non-interacting plumes. From these experimental trajectories, the merging distance - the distance downstream from the plume sources that the plumes can be considered to behave as a single, large plume - was determined and compared to the experimental merging distance.

Comparing the experimental merging distances to those predicted by the modelling work, it is apparent that the model consistently underestimates the importance of the blockage effect, as the plumes are seen to merge lower than predicted by the modelling. This is also seen in the experimental trajectories - particularly for smaller separations. In both the experiments and the model, we saw that the merging distance increased with source separation distance, number of co-linear plumes and decreased rapidly as the cross-flow velocity increased. This work could be extended to determine the trajectories and merging distances of arrays of plumes in a cross-flow, and comparing to the corresponding modelling, both of which were beyond the scope of this thesis.

Chapter 7

Discussion and Conclusion

Heat pumps are a renewable source of thermal energy which are becoming more common as countries move from fossil fuels to renewable, sustainable energy. These heat pumps can be used to provide both heating and cooling, and have been successfully used for cooling in Central London [7]. This thesis has considered only *open-loop* heat pumps in rivers, which discharge water of a different temperature than the ambient river (cooler if the heat pump is used for heating, warmer if for cooling) back into the ambient river. In doing so, the heat pump creates a thermal plume in the river. As these heat pumps are commonly part of a larger system of pumps, known as a district heating (or cooling) system, the interaction between these plumes is particularly important. This interaction can lead to reduced efficiency for downstream systems, known as thermal breakthrough or parasitic energy, and also give a combined thermal impact on the ambient environment, which affects the riverine life found in the nearby environment.

The behaviour of these thermal plumes has been investigated using field data, as well as being modelled in two types of ambient environment - a still environment and a cross-flow. The field data, collected by Dugdale *et al.* [54], showed a thermal power law between the temperature difference caused by the plume, and the distance downstream from the source of this plume. A similar power law was observed in several sites along the Matapédia river within this study. From this sample of data from the Matapédia river, the obtained power law appeared scale independent.

The mathematical modelling of plumes in a stillwater environment presented here considered two cases for plume behaviour - non-interacting and interacting. Currently in the literature there is a model for two plumes in stillwater [38] and for an infinite line of interacting plumes [65]. The merging height was not considered for the latter, instead the merging height of two plumes was validated. However, the intermediate cases of $3 \leq n < \infty$ had not been studied. These are studied in this work. In both interacting and non-interacting cases, the merging height - the vertical distance from the sources of the plumes at which the plumes could be considered a single, larger plume - was determined.

In the non-interacting case, the merging height of n co-linear plumes was seen to scale linearly for small n and like $\sqrt{n}$ for large n. Sources distributed as square grids and an equilateral triangle were also considered. The $n \times n$ square grid was seen, in the mathematical model, to have an identical merging height to the corresponding n co-linear plumes. Finally, the merged plume - the larger far-field plume that a line of n plumes can be considered to behave like - was investigated, and shown to always behave like a lazy plume and exhibit radial growth which scales with $\sqrt{n}$.

A model to determine the merging height of interacting plumes was also developed based on the assumption that the strength of plume-to-plume interaction is inversely proportional to the distance between the plumes. This model considered an arbitrary, finite, number of interacting co-linear plumes, thereby addressing the gap in the current literature which considers this for two plumes. This work also considered an equilateral triangle and a

2×2 square grid. These models were validated with experimental data. In all cases, these interacting models showed agreement with the experimental data. The findings from these models showed that the merging height of co-linear plumes scales linearly with source separation between the plumes, and approximately linearly with the number of plumes.

Next, plumes in a cross-flow were investigated, and a model was devised based on the existing JETLAG model. This modelling described the behaviour of plumes in a cross-flow which also exhibited the blockage effect - where upstream plumes were seen to shield the downstream plumes from the cross-flow - which had not previously been implemented in JETLAG. This model was able to capture the behaviour of n co-linear plumes and validated against experimental data for two and three co-linear plumes. the experimental trajectories were in good agreement with the trajectories modelled by the adjusted JETLAG model. It was also seen that the merging distance - the cross-flow analogy to the merging height - grew proportionally with the source separation, decreased rapidly with cross-flow velocity (this appeared to decay exponentially, but further data is required, as only three different flow rates were investigated) and increased with the number of plumes.

Further work to extend the research presented includes conducting a field study across a number of rivers of various sizes. The modelling for plumes in stillwater could also be extended to an arbitrary $n \times n$ grid of plumes, not just a 2×2 grid, and to an arbitrary array shape, both of which could be included in future work. Finally, the adjusted JETLAG model could be extended to incorporate arrays of plumes, whereas in this thesis only co-linear plumes were considered. These arrays would then be validated experimentally using a similar method to this thesis. It is important to note that, while it is possible to configure JETLAG in such a way that complex topologies can be considered, JETLAG does not simulate the turbulent behaviour of a cross-flow. Therefore, for scenarios where complex topologies are important, it may be more worthwhile to consider using CFD in order to capture both the turbulence and the topology. Indeed, this is typically how more sophisticated scenarios are currently simulated.

In 2020, the UK prime minister announced plans for the UK to install 600,000 heat pumps per year to help the UK reach net-zero by 2050. This PhD has provided a basis for assessing the potential thermal impacts of such heat pump schemes and could be used to inform their placement. It is reasonable to expect that many of these newly installed heat pumps will be placed in bodies of water (particularly rivers) where other heat pumps are already in use, not least because they will be clustered in areas of high population density. Therefore, insight into thermal impacts, particularly on the ambient environment, are critically important both for ensuring the ecological regime remains unharmed and for the efficiency and effectiveness of the heat pumps themselves. Of particular importance is the shielding of plumes by nearby, upstream plumes, altering their merging behaviour. This has significant implications for the interaction of heat pumps that are likely to be closely spaced in urban rivers due to the government's plans. Furthermore, this shielding - known in this work as the "blockage effect" - has been observed, both experimentally and from real-world data, to significantly alter the dynamics of the plumes. The most upstream plume has been observed to be much more curved, or deflected, than those downstream, which are shielded from the flow of the river, and therefore remain relatively straighter.

Chapter 8

Appendices

8.1 Derivation of the Plume Equations

Consider a cylindrical control volume of height Δz and radius $b(z)$. The control volume is subject to an entrainment velocity u_e and a vertical velocity $w(z)$. Outside of this control volume, the environment has reference density ρ_∞ whereas inside the density is ρ. Finally, the source density is given by ρ_0. The system of equations given by (1.1) - (1.3) considers conservation of mass, momentum and buoyancy, and will be derived in order. We first consider the conservation of mass.

By applying a mass balance to the cylindrical control volume, we note that the mass entering the bottom and sides of the cylinder are equal to the mass exiting the top. Therefore

$$\pi b^2 w|_{z+\Delta z} = \pi b^2 w|_z + 2\pi b u_e \Delta z \tag{8.1}$$

$$\Rightarrow \frac{b^2 w|_{z+\Delta z} - b^2 w|_z}{\Delta z} = 2\alpha u_e. \tag{8.2}$$

Applying the entrainment assumption, $u_e = \alpha w$, and taking the limit as

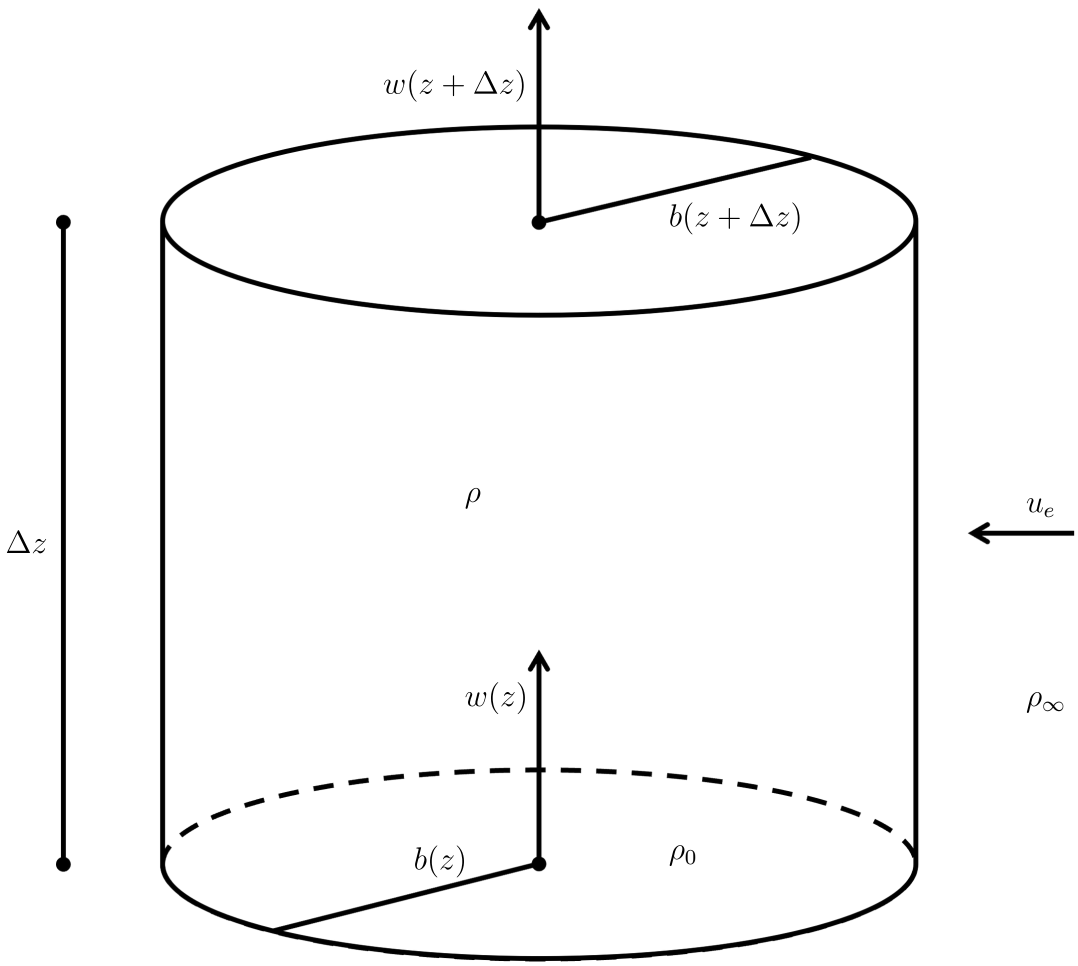

Figure 8.1: A schematic of the cylindrical control volume used in the derivation of the plume equations (1.1) - (1.3).

$\Delta z \to 0$, we see that

$$\frac{\mathrm{d}}{\mathrm{d}z}\left(b^2 w\right) = 2\alpha b w \tag{8.3}$$

Finally, by applying the definitions $Q = b^2 w$ and $M = b^2 w^2$, we arrive at

$$\frac{\mathrm{d}Q}{\mathrm{d}z} = 2\alpha M^{\frac{1}{2}} \tag{8.4}$$

which is (1.1), as required.

Next, we consider the conservation of momentum. We assume that the momentum exiting the top of the cylindrical control volume is balanced by the momentum entering the base, the sides and the upward buoyancy force. By assumption, zero momentum enters through the sides of the control volume. The upward buoyancy force is calculated as

$$\begin{aligned} F_b &= \pi \rho_\infty b^2 g \Delta z - \pi b^2 \rho g \Delta z \\ &= \pi b^2 g \Delta z (\rho_0 - \rho). \end{aligned}$$

The momentum balance is then given by

$$\begin{aligned} \pi \rho b^2 w^2|_{z+\Delta z} &= \pi \rho_1 b^2 w^2|_z + F_b && (8.5) \\ \Rightarrow \rho b^2 w^2|_{z+\Delta z} - \pi \rho b^2 w^2|_z &= b^2 g \Delta z (\rho_\infty - \rho) && (8.6) \\ \frac{\mathrm{d}}{\mathrm{d}z}(\rho b^2 w^2) &= b^2 g (\rho_\infty - \rho). && (8.7) \end{aligned}$$

By applying the Boussinesq approximation to (8.7) and dividing by the constant reference density, ρ_∞, we see that

$$\frac{\mathrm{d}}{\mathrm{d}z}(b^2 w^2) = b^2 g \frac{\rho_\infty - \rho}{\rho_\infty} = b^2 g'.$$

We define the buoyancy flux, $F = b^2 w g'$ and apply the definitions of Q and

M to arrive at (1.2)

$$\frac{\mathrm{d}M}{\mathrm{d}z} = \frac{FQ}{M}.$$

Finally, we consider the conservation of density deficit. By balancing the density deficit, we see that

$$\begin{aligned}
\pi b^2 w(\rho_0 - \rho)|_{z+\Delta z} &= \pi b^2 w(\rho_0 - \rho)|_z + 2\pi b u_e \Delta z(\rho_0 - \rho_\infty) \\
\Rightarrow \frac{\mathrm{d}}{\mathrm{d}z}(b^2 w[\rho_0 - \rho]) &= 2\alpha b w(\rho_0 - \rho_\infty) \qquad (8.8) \\
\Rightarrow \frac{\mathrm{d}}{\mathrm{d}z}(Qg(\rho_0 - \rho + \rho_\infty - \rho_\infty)) &= (\rho_0 - \rho_\infty) g \frac{\mathrm{d}Q}{\mathrm{d}z} \qquad (8.9) \\
\Rightarrow \frac{\mathrm{d}}{\mathrm{d}z}\left[\frac{Qg(\rho_0 - \rho_\infty)}{\rho_0} + \frac{Qg(\rho_\infty - \rho)}{\rho_0}\right] &= \frac{\mathrm{d}}{\mathrm{d}z}\left[\frac{Qg(\rho_0 - \rho_\infty)}{\rho_0}\right] - \frac{gQ}{\rho_0}\frac{\mathrm{d}}{\mathrm{d}z}(\rho_0 - \rho_\infty) \qquad (8.10) \\
\Rightarrow \frac{\mathrm{d}}{\mathrm{d}z}(Qg') &= \frac{gQ}{\rho_0}\frac{\mathrm{d}\rho_\infty}{\mathrm{d}z} \qquad (8.11) \\
\Rightarrow \frac{\mathrm{d}F}{\mathrm{d}z} &= -\mathrm{N}^2 Q \qquad (8.12)
\end{aligned}$$

8.2 Deriving the Strength of Plume Entrainment

Consider an incompressible, radial flow which is independent of angle. Then the velocity $\boldsymbol{u} = u_r(r)\hat{\boldsymbol{r}}$ satisfies

$$\nabla \cdot \boldsymbol{u} = \frac{1}{r}\frac{\mathrm{d}}{\mathrm{d}r}\left(r\frac{\mathrm{d}u_r}{\mathrm{d}r}\right) = 0 \qquad (8.13)$$

and the velocity is therefore given by

$$\boldsymbol{u} = \frac{K}{r}\hat{\boldsymbol{r}} \qquad (8.14)$$

where K is a constant. The flow is radial, and $K < 0$ for a sink. The strength of this line sink, $m(z)$ is equal to the flux through a circle of radius

$r = R$ and is given by

$$m(z) = \int_{r=R} \boldsymbol{u} \cdot \boldsymbol{n} \, \mathrm{d}S = \int_0^{2\pi} \left(\frac{K}{R}\right) \times R \, \mathrm{d}\theta = 2\pi K. \tag{8.15}$$

Finally, set $K = -A$, where $A > 0$ (note that this step wouldn't be necessary if line sources were considered). Hence, the radial component of $\boldsymbol{u}$ is given by

$$\boldsymbol{u} \cdot \hat{\boldsymbol{r}} = u_r = -\frac{A}{r} = -\frac{m}{2\pi}\frac{1}{r}. \tag{8.16}$$

This is the flow due to a line sink of strength $-m(z)$ as given in (4.7) with the prime omitted.

Bibliography

[1] Angus McCrone, U Moslener, F d'Estais, and C Grüning. Global trends in renewable energy investment report 2018. *UN Environment's Economy Division, Frankfurt School-UNEP Collaborating Centre for Climate & Sustainable Energy Finance, and Bloomberg New Energy Finance*, 2018.

[2] Committee on Climate Change. Net zero - the uk's contribution to stopping global warming. `https://www.theccc.org.uk/publication/net-zero-the-uks-contribution-to-stopping-global-warming/`, 2019. Accessed: 10-06-2019.

[3] SM Hasnain. Review on sustainable thermal energy storage technologies, part i: Heat storage materials and techniques. *Energy conversion and management*, 39(11):1127–1138, 1998.

[4] SM Hasnain. Review on sustainable thermal energy storage technologies, part ii: Cool thermal storage. *Energy conversion and management*, 39(11):1139–1153, 1998.

[5] N Wincott and J Billings. *CP2: Surface Water Source Heat Pumps: Code of Practice for the UK*. CIBSE, 2016.

[6] I Dincer and MA Rosen. *Exergy: Energy, Environment and Sustainable Development*. Newnes, 2012.

[7] VA Fry. Lessons from london: regulation of open-loop ground source

heat pumps in central london. *Quarterly Journal of Engineering Geology and Hydrogeology*, 42(3):325–334, 2009.

[8] What on earth is a heat pump? https://1010uk.org/articles/what-on-earth-is-a-heat-pump. Accessed: 05-03-2019.

[9] Designing Buildings. Water source heat pumps. https://www.designingbuildings.co.uk/wiki/Water_source_heat_pumps. Accessed: 21-06-2019.

[10] Engineers Edge. Convective heat transfer coefficients table. https://www.engineersedge.com/heat_transfer/convective_heat_transfer_coefficients__13378.htm. Accessed: 21-06-2019.

[11] A Miyara, K Kariya, Md H Ali, SB Selamat, and Jalaluddin. Heat transfer characteristics of various kinds of ground heat exchangers for ground source heat pump system. In *AIP Conference Proceedings*, volume 1788, page 020001. AIP Publishing, 2017.

[12] C Tong, X Li, L Duanmu, and Z Wang. Research on heat transfer characteristics of soil thermal storage in the non-heating season. *Procedia Engineering*, 205:3293–3300, 2017.

[13] OJ Svec, LE Goodrich, and JHL Palmer. Heat transfer characteristics of in-ground heat exchangers. *International Journal of Energy Research*, 7(3):265–278, 1983.

[14] Energy Consulting. Coefficient of performance. http://industrialheatpumps.nl/en/how_it_works/cop_heat_pump/, May 2018.

[15] Ofgem. Seasonal performance factor. https://www.ofgem.gov.uk/key-term-explained/seasonal-performance-factor-spf, May 2018.

[16] Martin Zogg. History of heat pumps-swiss contributions and international milestones. In *9th International IEA Heat Pump Conference, Zürich, Switzerland*, pages 20–22, 2008.

[17] ET Garside. Ultimate upper lethal temperature of atlantic salmon salmo salar l. *Canadian Journal of Zoology*, 51(8):898–900, 1973.

[18] TC Bjornn and DW Reiser. Habitat requirements of salmonids in streams. *American Fisheries Society Special Publication*, 19(837):138, 1991.

[19] RM Lee and JN Rinne. Critical thermal maxima of five trout species in the southwestern united states. *Transactions of the American Fisheries Society*, 109(6):632–635, 1980.

[20] D Caissie. The thermal regime of rivers: A review. *Freshwater Biology*, 51(8):1389–1406, 2006.

[21] CC Coutant. Compilation of temperature preference data. *Journal of the Fisheries Board of Canada*, 34(5):739–745, 1977.

[22] GA Wichert and P Lin. A species tolerance index for maximum water temperature. *Water Quality Research Journal*, 31(4):875–893, 1996.

[23] JEA John. Thermal pollution: A potential threat to our aquatic environment. *Envtl. Aff.*, 1:287, 1971.

[24] JG Eaton, JH McCormick, HG Stefan, and M Hondzo. Extreme value analysis of a fish/temperature field database. *Ecological Engineering*, 4(4):289–305, 1995.

[25] G Garner, DM Hannah, JP Sadler, and HG Orr. River temperature regimes of england and wales: Spatial patterns, inter-annual variability and climatic sensitivity. *Hydrological Processes*, 28(22):5583–5598, 2014.

[26] DM Hannah and G Garner. River water temperature in the united kingdom: Changes over the 20th century and possible changes over the 21st century. *Progress in Physical Geography*, 39(1):68–92, 2015.

[27] S Foster, J Love, I Walker, and M Crane. Heat pumps in district heating. *Department of Energy and Climate Change*, 2016.

[28] District heating and cooling. `https://www.icax.co.uk/Kingston_Heights.html`. Accessed: 05-03-2019.

[29] Energy Department for Business and Industrial Strategy. `https://assets.publishing.service.gov.uk/government/uploads/system/uploads/attachment_data/file/631146/UK_Energy_in_Brief_2017.pdf`, July 2017.

[30] Energy Department for Business and Industrial Strategy. `https://www.gov.uk/government/statistics/uk-energy-in-brief-2018`, July 2018.

[31] Energy Saving Trust. Renewable heat incentive. `https://www.energysavingtrust.org.uk/scotland/grants-loans/renewables/renewable-heat-incentive`. Accessed: 10-06-2019.

[32] GR Hunt and TS Van den Bremer. Classical plume theory: 1937–2010 and beyond. *IMA Journal of Applied Mathematics*, 76(3):424–448, 2011.

[33] BR Morton, GI Taylor, and JS Turner. Turbulent gravitational convection from maintained and instantaneous sources. *Proceedings of the Royal Society of London. Series A. Mathematical and Physical Sciences*, 234(1196):1–23, 1956.

[34] Ya B Zeldovich. The asymptotic laws of freely-ascending convective flows. *Zhur. Eksper. Teor. Fiz*, 7(12):1463–1465, 1937.

[35] Maarten van Reeuwijk and John Craske. Energy-consistent entrainment relations for jets and plumes. *Journal of Fluid Mechanics*, 782:333–355, 2015.

[36] JS Turner. *Buoyancy Effects in Fluids*. Cambridge University Press, 1979.

[37] Chu VH Lee JHW. Turbulent jets and plumes: A lagrangian approach, 2003.

[38] NB Kaye and PF Linden. Coalescing axisymmetric turbulent plumes. *Journal of Fluid Mechanics*, 502:41–63, 2004.

[39] AM Matulka, GP Lopez, AM Redondo, and AAM Tarquis. On the entrainment coefficient in a forced plume: Quantitative effects of source parameter. *Nonlinear processes in geophysics*, 21(1):269–278, 2014.

[40] GR Hunt and NG Kaye. Virtual origin correction for lazy turbulent plumes. *Journal of Fluid Mechanics*, 435:377–396, 2001.

[41] E Kaminski, S Tait, and G Carazzo. Turbulent entrainment in jets with arbitrary buoyancy. *Journal of Fluid Mechanics*, 526:361–376, 2005.

[42] GA Briggs. Plume rise, us atomic energy commission. *TID-25075, NTIS, Springfield, VA*, 1969.

[43] Fred Witham and Jeremy C Phillips. The dynamics and mixing of turbulent plumes in a turbulently convecting environment. *Journal of Fluid Mechanics*, 602:39–61, 2008.

[44] JW Deardorff and GE Willis. Investigation of turbulent thermal convection between horizontal plates. *Journal of Fluid Mechanics*, 28(4):675–704, 1967.

[45] JS Turner. The motion of buoyant elements in turbulent surroundings. *Journal of Fluid Mechanics*, 16(1):1–16, 1963.

[46] James S Turner. Jets and plumes with negative or reversing buoyancy. *Journal of Fluid Mechanics*, 26(4):779–792, 1966.

[47] MM Scase, CP Caulfield, SB Dalziel, and JCR Hunt. Time-dependent plumes and jets with decreasing source strengths. *Journal of Fluid Mechanics*, 563:443–461, 2006.

[48] GG Rooney and PF Linden. Similarity considerations for non-boussinesq plumes in an unstratified environment. *Journal of fluid mechanics*, 318:237–250, 1996.

[49] Yongxing Ma. *Plumes in Two-Layer Stratified Fluid with and without Background Rotation*. PhD thesis, University of Alberta, 2018.

[50] BR Morton. Forced plumes. *Journal of Fluid mechanics*, 5(1):151–163, 1959.

[51] GR Hunt and NB Kaye. Lazy plumes. *Journal of Fluid Mechanics*, 533:329–338, 2005.

[52] Adrian Bejan, S Ziaei, and Sylvie Lorente. Evolution: Why all plumes and jets evolve to round cross sections. *Scientific reports*, 4:4730, 2014.

[53] AW Woods and CP Caulfield. A laboratory study of explosive volcanic eruptions. *Journal of Geophysical Research: Solid Earth*, 97(B5):6699–6712, 1992.

[54] Stephen J Dugdale, Normand E Bergeron, and André St-Hilaire. Spatial distribution of thermal refuges analysed in relation to riverscape hydromorphology using airborne thermal infrared imagery. *Remote Sensing of Environment*, 160:43–55, 2015.

[55] Matthew F Johnson and Robert L Wilby. Seeing the landscape for the trees: metrics to guide riparian shade management in river catchments. *Water Resources Research*, 51(5):3754–3769, 2015.

[56] Luna Bergere Leopold and Thomas Maddock. *The hydraulic geometry of stream channels and some physiographic implications*, volume 252. US Government Printing Office, 1953.

[57] Walter B Langbein. Geometry of river channels. *Journal of the Hydraulics Division*, 90(2):301–312, 1964.

[58] Walter B Langbein and Luna B Leopold. Quasi-equilibrium states in channel morphology. *American Journal of Science*, 262(6):782–794, 1964.

[59] DIH Barr, JF RIDDELL, CCS SONG, MK ALAM, MA GILL, MANNING, A NISHAT, CT YANG, and FROUDE. A contribution to regime theory relating principally to channel geometry. *Proceedings of the Institution of Civil Engineers*, 71(3):955–969, 1981.

[60] Ashlan Berry. Development of regional and hydraulic geometry curves for the eastern kentucky coalfields, 2016.

[61] René Leclerc and Michel F Lapointe. Hydraulic geometry of alluvial rivers in the bois-francs region of southern quebec. *Canadian Water Resources Journal*, 19(3):237–252, 1994.

[62] E Moses, G Zocchi, I Procaccia, and A Libchaber. The dynamics and interaction of laminar thermal plumes. *EPL (Europhysics Letters)*, 14(1):55, 1991.

[63] E Moses, G Zocchi, and A Libchaberii. An experimental study of laminar plumes. *Journal of Fluid Mechanics*, 251:581–601, 1993.

[64] C Cenedese and PF Linden. Entrainment in two coalescing axisymmetric turbulent plumes. *Journal of Fluid Mechanics*, 752, 2014.

[65] GG Rooney. Merging of a row of plumes or jets with an application to plume rise in a channel. *Journal of Fluid Mechanics*, 771, 2015.

[66] Jorge J Moré, Burton S Garbow, and Kenneth E Hillstrom. User guide for minpack-1. Technical report, CM-P00068642, 1980.

[67] MM Scase, CP Caulfield, and SB Dalziel. Boussinesq plumes and jets with decreasing source strengths in stratified environments. *Journal of Fluid Mechanics*, 563:463–472, 2006.

[68] H Yamamoto, C Cenedese, and CP Caulfield. Laboratory experiments on two coalescing axisymmetric turbulent plumes in a rotating fluid. *Physics of Fluids*, 23(5):056601, 2011.

[69] H Rouse, CS Yih, and HW Humphreys. Gravitational convection from a boundary source. *Tellus*, 4(3):201–210, 1952.

[70] SJ Gaskin, DA Papps, and IR Wood. The axisymmetric equations for a buoyant jet in a cross flow. In *Twelfth Australasian Fluid Mechanics Conference (ed. RW Bilger)*, pages 347–350, 1995.

[71] Adrian CH Lai and Joseph HW Lee. Dynamic interaction of multiple buoyant jets. *Journal of fluid mechanics*, 708:539–575, 2012.

[72] E Bjørn and PV Nielsen. *Merging Thermal Plumes in the Indoor Environment*. Department of Building Technology and Structural Engineering, Aalborg University, 1995.

[73] GI Taylor. Flow induced by jets. *Journal of Aero/Space Science*, XXV, 1958.

[74] Hugo B Fischer, John E List, C Robert Koh, Jorg Imberger, and Norman H Brooks. *Mixing in Inland and Coastal Waters*. Elsevier, 1979.

[75] Habib O Anwar. Turbulent structure in a river bend. *Journal of hydraulic engineering*, 112(8):657–669, 1986.

[76] PT Wooler, GH Burghart, and JT Gallagher. Pressure distribution on a rectangular wing with a jet exhausting normally into an airstream. *Journal of Aircraft*, 4(6):537–543, 1967.

[77] Daeyoung Yu, MS Ali, and Joseph HW Lee. Multiple tandem jets in cross-flow. *Journal of hydraulic engineering*, 132(9):971–982, 2006.

[78] DP Hoult and JC Weil. Turbulent plume in a laminar cross flow. *Atmospheric Environment (1967)*, 6(8):513–531, 1972.

[79] David P Hoult, James A Fay, and Larry J Forney. A theory of plume rise compared with field observations. *Journal of the Air Pollution Control Association*, 19(8):585–590, 1969.

[80] Joseph HW Lee and Valiant Cheung. Generalized lagrangian model for buoyant jets in current. *Journal of Environmental Engineering*, 116(6):1085–1106, 1990.

[81] Walter E Frick. Non-empirical closure of the plume equations. *Atmospheric Environment (1967)*, 18(4):653–662, 1984.

[82] V Cheung and JHW Lee. Discussion of 'improved prediction of bending plumes'. *Journal of Hydraulic Research*, 1996.